Final Technical Report

This report summarizes research resulting from 3/1/97-2/28/99 NEHRP support

Thrust fault slip rates deduced from coupled geomorphic and tectonic models of active faults and folds in the San Francisco Bay Area: Collaborative Research with Arizona State University, and University of California, Davis

1434-H-97-GR-03113

Submitted by

George E. Hilley and Ramón Arrowsmith, Ph.D.

Department of Geology

Arizona State University

Tempe, AZ 85287-1404

480-965-3541

hilley@asu.edu

ramon.arrowsmith@asu.edu

June 2, 2000

Program elements: Element #1 Evaluate urban hazard and risk (60%), Element #2 Understanding the earthquake process (20%), and Element #3 Providing geologic hazards information services (20%).

Key words: Neotectonics, teconic geomorphology, Quaternary fault behavior, and surface deformation.

Abstract

This project focused on the compelling evidence for high topography and high rock uplift rates in the Santa Cruz Mountains (SCM) California and the implications for earthquake hazard to the heavily populated and industrialized Santa Clara Valley. The work followed two principal paths on which we report here.

Morphometric analyses of the digital topography of the San Francisco Peninsula

We analyzed the morphometry of the Southern San Francisco Bay Area in order to 1) identify areas potentially undergoing high active uplift, 2) the location of faults that may pose seismic risk to the Santa Clara Valley, and 3) identify study areas for detailed work in the Peninsula area. We aquired 23 USGS 7.5 minute Digital Elevation Models (DEMs) as a topography base for our analysis. Three dimensional visualization of the topography in the area was used to identify lineaments in the topography. In addition, a Geographic Information System (GIS) containing the geology of the Southern San Francisco Bay Area (courtesy of C. Wentworth) was overlain onto the topography in order to see the relative influence of lithologic contacts and active uplift on determining the morphology of the Southern Bay Area.

Several morphometric parameters were computed in order to determine the degree of incision into the Santa Cruz Mountains. We hypothesize that the bulk of the relief in the Santa Cruz Mountains is formed by uplift along thrust faults that strike sub-paralell to the San Andreas Fault. Therefore, there is an intimate link between uplift rates, material redistribution rates (due to geomorphic processes), and the morphology of the Santa Cruz Mountains .This analysis utilized readily available digital topographic data and applied standard GIS tools to the analysis of the San Francisco Peninsula topography. The analysis shows that morphometric investigations may identify zones of high rock uplift. By testing it in the Southern Santa Cruz Mountains where independent analyses conclude similarly, we were then able to apply it to the rest of the region and identify Black Mountain and portions of the Half Moon Bay/San Mateo area.

The topographic investigations for the study area started with the basic topography, and then successively illustrate the basic morphometric parameters of drainages, slope, curvature, and aspect. Additional more "derivative" morphometries are: local relief calculated over the neares 150 and 300 m, the residual (the difference between sirfaces defining ridgelines and drainages), and the minimum exhumation (difference between the envelope and the topography.

A number of factors influence the interpretation of these data: 1) complex fault geometries, both in map view and at depth, 2) variations in slip distributions along these faults during recent times, resulting in a complicated uplift distribution in areas surrounding these faults, 3) disequilibrium in geomorphic processes (ungraded river channels, partial relaxation of surrounding hillslopes to graded channels, importance of landsliding), 4) accuracy of 7.5 minute DEMs, 5) noise due to gridding algorithms of surfaces, 6) differential

resistance to erosion of different rock types juxtaposed by slip along faults, and 7) mechanical weakening of rocks by increased fracture density along fault zones. We summarize our initial theoretical investigation of a number of these factors in the second section of this report.

Landscape development modeling of transport- and production- limited fault scarps, with implications for morphologic dating and earthquake hazard assessment in tectonically active regions

A fault's geomorphic expression contains information about the rates and timing of movement along the fault and the rates of geomorphic processes acting to redistribute sediment across the fault. Where geomorphic rates and initial landform geometries can be reconstructed or inferred, fault scarp and/or fault zone morphology may be used to estimate tectonic rates. This method provides broader temporal (10 kyr–100 kyr) coverage than detailed fault zone studies that typically focus on individual fault ruptures and events.

Analyses of the morphology of scarps to determine tectonic rates typically are limited to scarps that do not expose bedrock (transport-limited scarps). However, scarps in which transport is limited by the rate at which bedrock is converted to regolith (production-limited) has not received much attention. In this study, we present a model for the degradation of fault scarps dominated primarily by production limited conditions. We determine what range of tectonic rates the scarp morphology is most sensitive for transport- and production-limited conditions. For transport-limited scarps, we find that scarp morphology is dependent on tectonic and geomorphic transport rates. For realistic geomorphic transport rates, transport-limited scarps are sensitive to tectonic uplift rates between 2–10 mm/yr. We find that for typical bedrock weathering rates, a steady-state condition, where the surface topography of the scarp and the location of soil–bedrock interface do not vary with time is never achieved. In contrast to transport-limited scarps, production-limited scarp morphology depends primarily on the tectonic uplift and bedrock production rates. Production-limited scarps are sensitive to lower tectonic uplift rates (0.01–0.5 mm/yr). From our models, we propose the following possibilities for short and long term scarp development: 1) Scarp development will remain transport-limited for the duration of the faulting if the tectonic rates are slow, the tectonic uplift is short lived, or the thickness of transportable material is large. 2) The scarp will change from transport-limited conditions towards production-limited conditions if high ($>$ 1 mm/yr) tectonic uplift rates are sustained. The time at which the scarp becomes production-limited will depend on the initial thickness of transportable material and the diffusive transport rate. 3) Under special circumstances where bedrock production rates are high and rock uplift rates are less than 1 mm/yr, transport-limited conditions may be preserved over long time-scales.

For typical tectonic and bedrock production rates, our analysis suggests that an equilibrium profile

and soil-bedrock interface cannot persist indefinitely under transport-limited conditions. Therefore, faults slipping at rates where the rock uplift rate exceeds 1 mm/yr will usually be driven into production-limited conditions. This conceptual model is consistent with field observations where transport-limited scarps persist in faulted alluvium in front of a larger, production-limited range front created by continual faulting.

Non-technical summary

We assume that the surface deformation caused by active earthquake faulting is expressed in tectonic landscapes. Analysis of landforms can be used to determine information about the location, geometry, and activity of the causative faults. If these faults do not break the surface, they would go undetected by standard evaluation methods. This research uses an integrated approach of GIS (Geographic Information Systems) analysis of digital elevation models, and state-of-the-art computer models of an actively deforming and degrading landscape to provide new tools for the quantitiative identification and characterization of hazardous faults. We have applied this approach to the evaluation of active thrust faults in the southern San Francisco Bay area. A computer analysis of the importance of fault geometry, rate of surface transport, and production of transportable material provides an innovative look at the controlling parameters observed in the field and help to identify the conditions under which the landscape contains resolveable information about the active tectonic deformation field.

Contents

1 List of Plates

The plates contained in the pocket at the end of this report provide a spectular illustration of the morphometric variability of the landscape of the San Francisco Peninsula and indicate the zones of high rock uplift, including the most significant rock uplift zone: the southern Santa Cruz Mountains. See the first section entitled, "Morphometric analysis of the Santa Cruz Mountains."

1. Topography of San Francisco Peninsula
2. Topography and drainage network of San Francisco Peninsula
3. Slope map of San Francisco Peninsula
4. Landscape curvature map of San Francisco Peninsula
5. Aspect map of San Francisco Peninsula
6. Local relief (120 m kernal) in the central southern Santa Cruz Mountains
7. Local relief (300 m kernal) in the central southern Santa Cruz Mountains
8. Residual map of topography of San Francisco Peninsula
9. Minimum exhumation map of San Francisco Peninsula

2 Overview

This project focused on the compelling evidence for high topography and high rock uplift rates in the Santa Cruz Mountains (SCM) California and the implications for earthquake hazard to the heavily populated and industrialized Santa Clara Valley. This area was affected by the 1989 Loma Prieta earthquake, yet that event did not uplift the highest topography of the SCM, and another, potentially more hazardous deformation source is implied. The work followed two principal paths on which we report here.

2.1 An investigation of topographic parameters measurable from digital topography (morphometry from DEMs) applying new Geographic Information System (GIS)-based methods of calculation and visualization

This analysis was applied to the entire San Francisco Penisula and indentified the spatial extents of areas in which high rock uplift, and hence high deformation rates and earthquake potential, were evident. The southern SCM were indeed the area with the highest indication of active deformation, but the area of Black Mountain near Los Altos and Palo Alto, and portions of the northern Santa Cruz Mountains north of Half Moon Bay were also noted in the analysis.

2.2 Landscape development modeling

While the above morphometric analysis was illustrative, it certainly pointed out the limitations of a purely empirical approach to the interpretation of topography. Thus we embarked on the second focus of this research: landscape development modeling considering variable fault geometries, simple surface transport processes, and the production of regolith available for transport. This approach was appropriate given the uncertainties in range-scale landscape development modeling and provides insights into the processes controlling topographic development at the key positions of fault scarps in the deforming landscape. This analysis is far-reaching in that it extends the long standing alluvial fault scarp analyses commonly used in earthquake hazard investigations to include the more complicated aspects of variable fault geometry and regolith production. Transport-limited conditions are those in which sufficient regolith is always available for transport and thus surface transport is at full capacity. In contrast, production-limited conditions are ones in which the local surface lowering rate is equal to the regolith production rate, and transport capacity is limited to the available regolith. This portion of the investigation provides a number of innovative analyses including: normalization of the transport-limited problem; a refinement of the reverse fault scarp, production-limited case; an evaluation of the time to steady-state for landscape in areas of active tectonism; and further refines the error analysis in the fitting of model profiles to observed one;, bringing the analysis back to the beginning: the range of applicability of these studies to earthquake hazard investigation.

2.2.1 Publications

Hilley, G.E, Amoroso, L., and Arrowsmith, J R., Morphologic dating of transport- and production-limited fault scarps, *GSA Abstracts with Programs*, *31*, 7, 302, 1999.

Hilley, G. E., Arrowsmith, J R., and Bürgmann, R.: Investigation of active deformation using a landscape development model and field examination of landforms along the northeastern margin of the southern Santa Cruz Mountains, *GSA Abstracts with Programs*, *29*, 6, 324, 1997.

Hilley, G. E., Arrowsmith, R., and Pollard, D. D., A geographic information system applied to areas of active tectonics, *GSA Abstracts with Programs*, *28*, 7, 265, 1996.

Hilley, G. E., Arrowsmith, R., and Pollard, D. D., Mechanical modeling and visualization of fault bends using boundary elements methods and geographic information systems, *EOS Transactions AGU*, 1996.

2.2.2 Other activities

Presentation at Monte Vista fault zone—what do we know about it and what is the hazard? USGS Workshop, October 30, 1997.

Presentation on Santa Cruz Mountains rangefront deformation at The Bay Area Paleoearthquake Experiment–BAPEX May 1998.

Participation in The Working Group on California Earthquake Probabilities 1999.

3 Morphometric analysis of the Santa Cruz Mountains

3.1 Introduction

The earth's surface acts as a limiting surface between processes that uplift or depress it (tectonic processes) and those that change its elevation by redistribution of material (geomorphic processes) (Penck, 1953). Rock uplift by isostatic equilibration, fault movement, folding and intrusion, and volcanic deposition increases the elevation of a region. Fluvial erosion, landsliding, soil creep, and glacial erosion decrease the elevation of a region. These two sets of processes are spatially variable and may act on different elements of the landscape. For example, rock uplift from isostatic readjustment of material acts nearly uniformily over kilometer-scale regions, while fluvial transport occurs in discrete conduits that dissect the relatively uniformily uplifted surface. Therefore, it is the interaction of these processes on the limiting surface of the earth which form landscapes. Moreover, the rates at which these processes act define the interaction between the processes, and thus determine the morphology of the landscapes on the earth's surface. If we have knowledge of the surface morphology and constrain the geomorphic rates by geologic observations, then we can estimate tectonic rates.

We analyzed the morphometry of the Southern San Francisco Bay Area in order to 1) identify areas potentially undergoing high active rock uplift, 2) the location of faults that may pose seismic risk to the Santa Clara Valley, and 3) identify study areas for detailed work in the Peninsula area. The calculations were performed on digital topography provided by the USGS at 1:24,000 scale within the ARC/INFO Geographic Information System software package.

The relative plate motion in the Bay Area, Northern California is accomodated along several strike-slip faults including the San Andreas Fault (SAF), the Hayward Fault, and the Calavaras Fault. In addition to the strike-slip motion along these faults, a significant component of SAF-normal convergence has been documented by Bürgmann et al. (1997). The convergence is accomodated along thrust faults in the Peninsula of the Bay Area that strike sub-parallel to the SAF. We hypothesize that differential motion along these faults drives incision and increases relief within drainage basins of the Santa Cruz Mountains. By quantifying the morphology of the Santa Cruz Mountains, in particular relief within drainage basins, we may highlight spatial zones with differing tectonic uplift rates. While a morphometric analysis cannot provide us with quantitative rates for these processes, it may be used to determine the relative distribution of uplift in the Santa Cruz Mountains.

3.2 Morphometric Methods

One of the problems in performing morphometric analyses to quantify the shape of the landscape is the inability to reproduce many of themorphometric parameters. For example, the topographic residual gives

a measure of relief within the drainage basins in a landscape. It is calculated by subtracting two surfaces, the envelope and the subenvelope surfaces. The envelope surface is calculated by taking elevations from the ridgelines in a landscape and interpolating a surface from these points. Likewise, the subenvelope surface is calculated by selecting elevations from the stream channel bottoms in a landscape and interpolating a surface between those points. By subtracting these two surfaces, the relief within drainage basins is quantified. However, the end distribution of the residual values is dependent on which points are selected for the envelope and subenvelope surfaces. Therefore, the residual surface typically is plagued with interpretation and hence, non-reproducibility.

We aquired twenty-three USGS 7.5 minute Digital Elevation Models (DEMs) as a topography base for our analysis. The horizontal resolution of this data is 30 meters. Three dimensional visualization of the topography in the area was used to identify lineaments in the topography (Figures 1–3). Contrasting rock types adjacent to faults may result in differing susceptabilities to transport and may be expressed as topographic breaks. Also, sag ponds, shutter ridges, and offset stream channels indicative of active strike-slip faulting may be readily identified in perspective view. The topographic data were integrated with a Geographic Information System (GIS) containing the geology of the Southern San Francisco Bay Area (Wentworth, 1993) in order to study the relative influence of contrasting rock types and active rock uplift the morphology of the Southern Bay Area.

Several morphometric parameters were computed in order to determine the degree of incision into the Santa Cruz Mountains. We developed standard algorithms for computing the envelope, subenvelope, and residual surfaces from DEMs. The calculations are performed by a computer and determine the envelope, subenvelope, and residual surface. Traditionally, these surfaces are computed by interpretation of contour maps (e.g. Stearns, [1967]; Bullard and Lettis [1993]; Burgmann et al., [1994]; Arrowsmith [1995]) by interpolating a surface between points selected along ridge crests and stream bottoms. Therefore, the envelope, subenvelope, and residual surfaces are subject to interpretation and are not uniquely defined by the landscape. The algorithms we developed uniquely determine an envelope, subenvelope, and residual surface based on two user-specified parameters.These techniques represent an effort to standardize the computation of morphometric parameters, making them more useful for quantitative analyses. Our computations are performed with the aid of the ARC/INFO GIS software. The general method for computing the envelope, subenvelope, and residual surfaces is shown schematically in Figure 4.

3.3 Results

3.3.1 Morphometry of the San Francisco Bay Peninsula

Perspective Visualization of the San Francisco Bay Area

We created three-dimensional images of the Santa Cruz Mountains in order to identify topographic lineaments and study the general morphology of this area. All images were produced on a Silicon Graphics Indigo2 R10000 Workstation running ERMapper 5.5, Arc/Info 7.1.2, and ArcView in the Active Tectonics, Quantitative Structural Geology and Geomorphology laboratory at Arizona State University (http://activetectonics.la.asu.edu). These images were rendered using shading and reflectance algorithms. In these algorithms, a shaded-area contour map was draped onto the digital topography of the Bay Area. The reflectence of this draped surface was computed based on the observation perspective and the location of a light source. The rendered images were exported as JPEG graphics files.

Figure 1 shows an overview of the digital topography of the San Francisco Peninsula. A cursory inspection of this oblique topographic image shows the influence of the San Andreas Fault (SAF) and associated secondary structures (e.g. the Monte Vista, Berrocal, Sargent Fault Zones) on the landscape. The clear linear trough running through the topography is the SAF. Labeled on the map are Mt. Loma Prieta (the site of the 1989 Loma Prieta Earthquake) and Black Mountain (a focus of deformation during the 1906 San Francisco Earthquake). The Santa Cruz Mountains in this area are likely produced by uplift due to slip along thrust faults east of the San Andreas Fault (Burgmann et al, 1994).

Figure 2 shows a perspective view looking down strike of the San Andreas Fault from Mt. Loma Prieta. Clearly visible in this image is the uplifted area east of the San Andreas Fault (right side of fault in figure) that is being uplifted along the Monte Vista, Berrocal, Shannon, and Sargent thrust faults. These faults are collectively referred to as the Southern Santa Clara Valley Thrust Zone (SSCVTZ). Also visible in this image are several topographic welts, including Black Mountain. These welts may represent blocks that are being rotated by movement along the San Andreas Fault and the Southern Santa Clara Valley Thrust Zone as they pass through restraining bends in the Loma Prieta area and the Black Mountain area.

Figure 3 is a perspective view looking down the strike of the San Andreas Fault toward San Francisco. The vantage point is approximately centered at Black Mountain. In this figure, we see a reduction in relief as we move farther away from the restraining bend in the San Andreas Fault (near Mt. Loma Prieta). The segment of the fault we are looking at contains Crystal Springs Resevoir. There is no vertical exageration in any of these figures.

Morphometry of the Loma Prieta Area and Cupertino Area

We tested our morphometric techniques on the Loma Prieta area and the Cupertino area. The 7.5 minute DEMs used in the Loma Prieta area are the Los Gatos Quadrangle, the Loma Prieta Quadrangle, the Laurel Quadrangle, and the Santa Teresa Hills Quadrangle. The 7.5 minute DEM used in the Cupertino area is the Cupertino Quadrangle. In addition, Digital Orthophoto Quadragles are available for the Cupertino area and were used there to aid in our geomorphic interpretations.

The relative magnitudes of the residual surface is shown in Figure 5. High values of the residual are found

northeast of the San Andreas Fault in this area. Fission track data show that the block northeast of the San Andreas fault may be undergoing rock uplift rates as high as 1 mm/yr. The high uplift rates inferred from fission track data roughly corespond to areas with high residual magnitude. The area in Figure 5 encompasses four 7.5 minute quadrangles.

Dip slip motion along the San Andreas Fault is insufficent to account for the observed uplift in the Loma Prieta area. Instead, dip slip motion along thrust faults striking northwestward may accomodate much of the uplift (Burgmann et al., 1994). The 1989 Loma Prieta earthquake occurred along a northwest striking, southwest dipping structure that may be a source of uplift in the area.

This thrust belt extends northwest into the Santa Clara Valley, east of the Santa Cruz Mountains. While no historic seismicity has been recorded on the structures to the northwest, we observe high topographic residual values which indicate that these structures may be responsible for the uplift of the northern Santa Cruz Mountains. We conducted a detailed morphometry of the Cupertino Quadrangle to the northwest of Loma Prieta, which is located in the heart of Silicon Valley's high-tech industry. The Cupertino Quadrangle contains three sets of faults- the SAF, and two of the faults of the Santa Clara Valley Thrust Zone (the Monte Vista and Berrocal Thrusts). We used morphometry to analyze the inferred spatial distribution of rock uplift as indicated by the residual calculation. Our residual calculations in the Cupertino Quadrangle are based on the following values for the residual algorithm presented previously: channelization threshold was set to 63000 m^2, and the ARC/INFO function BASIN (GRID function) was used to delineate the drainage basin boundaries. The results of the analysis are presented Figure 6. The residual roughly outlines some sections of the Monte Vista and Berrocal Faults in this area; however, the diffuse distribution of the residual magnitudes between centers of local high residual complicate interpretation. In order to generalize the residual surface to show areas of concentrated residual magnitudes, we performed a nearest neighbor analysis in which the value of the residual at any point is equal to the average of the magnitudes of areas lying within 250 meters of the point under consideration. This calculation may show general trends in the residual magnitudes. The results of this analysis for the Cupertino Quadrangle are labeled the Generalized Residual and are shown in Figure 7.

Morphometric Analysis of the Southern San Francisco Bay Area, California

We calculated the topographic residual for the entire Southern San Francisco Bay Area in order to identify areas that may be undergoing active uplift due to faulting. We aquired the DEMs for the area1 and calculated the envelope, subenvelope, and residual surfaces based on these data. The value used for critical channelization flow accumulation was 63000 m^2 and the value used for the critical basin flow accumulation value was 54000 m^2. These values identified most of the details of the drainage basins and ridges, providing an accurate representation of the landforms in the study area. The generalized topographic residual for the Southern Bay Area was computed using a 15 km search radius, and the large-scale topographic residual was computed

using a 1.5 km search radius. The vaules of the search radius were chosen to highlight morphometric trends over intermediate- and small- scales.

Figure 8 shows the generalized topographic residual surface for the area investigated. The red lines in the image are mapped faults in the area. The generalized residual surface serves to highlight some general areas of high residual in the area investigated. From this generalized residual surface, we identified three areas with high values of the topographic residual. These areas are located near Mt. Loma Prieta, Black Mountain, and San Mateo. In general, high values of the generalized topographic residual apparently outline the location of active faults, with high residual values observed in the uplifted portion of the area and a reduction in residual values across the fault trace on the downthrown side of the fault. The details of the topographic residual in these areas is not as clear as the general trend. The details of the topographic residual are a function of 1) complex fault geometries, both in map view and at depth, 2) variations in slip distributions along these faults during recent times, resulting in a complicated uplift distribution in areas surrounding these faults, 3) disequilibrium in geomorphic processes (ungraded river channels, partial relaxation of surrounding hillslopes to graded channels, importance of landsliding), 4) accuracy of 7.5 minute DEMs, 5) noise due to gridding algorithms of surfaces, 6) differential resistance to erosion of different rock types juxtaposed by slip along faults, and 7) mechanical weakening of rocks by increased fracture density along fault zones.

The residual surface was calculated for three areas that displayed high residual values on the Generalized Residual Map of the Southern Bay Area (Figure 8). The first of these areas is the Sierra Azul block, located at the beginning of the restraining bend in the San Andreas Fault near Loma Prieta. The residual surface for this area is shown Figure 10. Fission track data suggest that the area has undergone rapid exhumation (on the order of 0.8 mm/yr) over the last 4.6 million years (Burgmann et. al, 1994). Uplifted marine terraces near Santa Cruz and correlation of geologic units contrain the surface uplift in the area suggesting 2-3 km of unroofing. Fission track data provide a means of calibrating the residual magnitudes to uplift rates.

In the Sierra Azul block, uplift is likely accomodated along the Sargent, Shannon, and Berrocal thrust faults (part of the SSCVTZ). While the fission track data provide a means of imaging long-term uplift in this area, a calibrated morphometric analysis may yield details of the uplift distribution in this area. This distribution could be used to infer at-depth fault geometries and slip rates.

Another area of high residual was the Black Mountain area (Figure 11). In this area, the Monte Vista and Berrocal Fault are the primary thrust faults in the area. Black Mountain was an area that underwent large deformation during the 1906 San Francisco earthquake. Note in this residual map the low values of the topographic residual in the Steven's Creek embayment of the Santa Cruz mountains. Offset terraces have been well documented in this area, demonstrating recent and continual uplift of this area.

The last area we investigated was the Half Moon Bay/San Mateo area of the Bay Area. This area shows high residual values. Figure 12 is a map of the 1.5 km generalized residual of this area. The inferred uplift in this

area may be a result of complex faulting in this area and/or lithologic influences on the residual values. This area is near Montara Mountain which contains a granite more resistant to weathering than the surrounding material.

3.4 Summary and Conclusions

This analysis utilized readily available digital topographic data (Figure 13) and applied standard GIS tools to the analysis of the San Francisco Peninsula topography. The analysis shows that morphometric investigations may identify zones of high rock uplift. By testing it in the Southern Santa Cruz Mountains where independent analyses conclude similarly, we were then able to apply it to the rest of the region and identify Black Mountain and portions of the Half Moon Bay/San Mateo area.

A summary of all of the topographic investigations for the study area is shown very clearly in the plates at the end of this document. Those nine plates start with the basic topography, and then successively illustrate the basic morphometric parameters of drainages, slope, curvature, and aspect. The other plates illustrate additional more "derivative" morphometries: local relief calculated over the neares 150 and 300 m, the residual (the difference between sirfaces defining ridgelines and drainages), and the minimum exhumation (difference between the envelope and the topography.

The plates illustrate the richness of the topographic datasets and its study. However, it is clear that a number of factors influence the interpretation of these data: 1) complex fault geometries, both in map view and at depth, 2) variations in slip distributions along these faults during recent times, resulting in a complicated uplift distribution in areas surrounding these faults, 3) disequilibrium in geomorphic processes (ungraded river channels, partial relaxation of surrounding hillslopes to graded channels, importance of landsliding), 4) accuracy of 7.5 minute DEMs, 5) noise due to gridding algorithms of surfaces, 6) differential resistance to erosion of different rock types juxtaposed by slip along faults, and 7) mechanical weakening of rocks by increased fracture density along fault zones. We summarize our initial theoretical investigation of a number of these factors in the second section of this report.

4 References

Arrowsmith, J R., *Coupled tectonic deformation and geomorphic degradation along the San Andreas Fault system*, Ph.D. dissertation, Stanford University, 356 pp., 1995.

Bullard, T. F., and Lettis, W. R., Quaternary fold deformation associated with blind thrust faulting, Los Angeles basin, California, *Journal of Geophysical Research*, v. 98, p. 1303-1317, 1993.

Bürgmann, R., Arrowsmith, J R., Dumitru, T., McLaughlin, R., Rise and fall of the southern Santa Cruz Mountains, from fission tracks, geomorphology, and geodesy, *Journal of Geophysical Research*, v. 99, p.

20181–20202, 1994.

Bürgmann, R., Segall, P., Lisowski, M., and Svarc, J.L., Postseismic Strain Following the 1989 Loma Prieta Earthquake From GPS and Leveling Measurements, *Journal of Geophysical Research*, v. 102, p.4933-4955, 1997.

Penck, W., *Morphological analysis of landforms*, 429 pp., MacMillan, New York, 1953.

Stearns, R. G., Warping on the Western Highland Rim Peneplain in Tennessee by groundwater sapping, *Geological Society of America*, v. 78, p. 1111–1124, 1967.

Wentworth, C. M., Fumal, T. E., Brocher, T. M., Brabb, E. E., The areal distribution of geologic materials and their seismic velocities, San Francisco Bay area, California, *Eos, Transactions, American Geophysical Union* v. 78, p. 436. 1997.

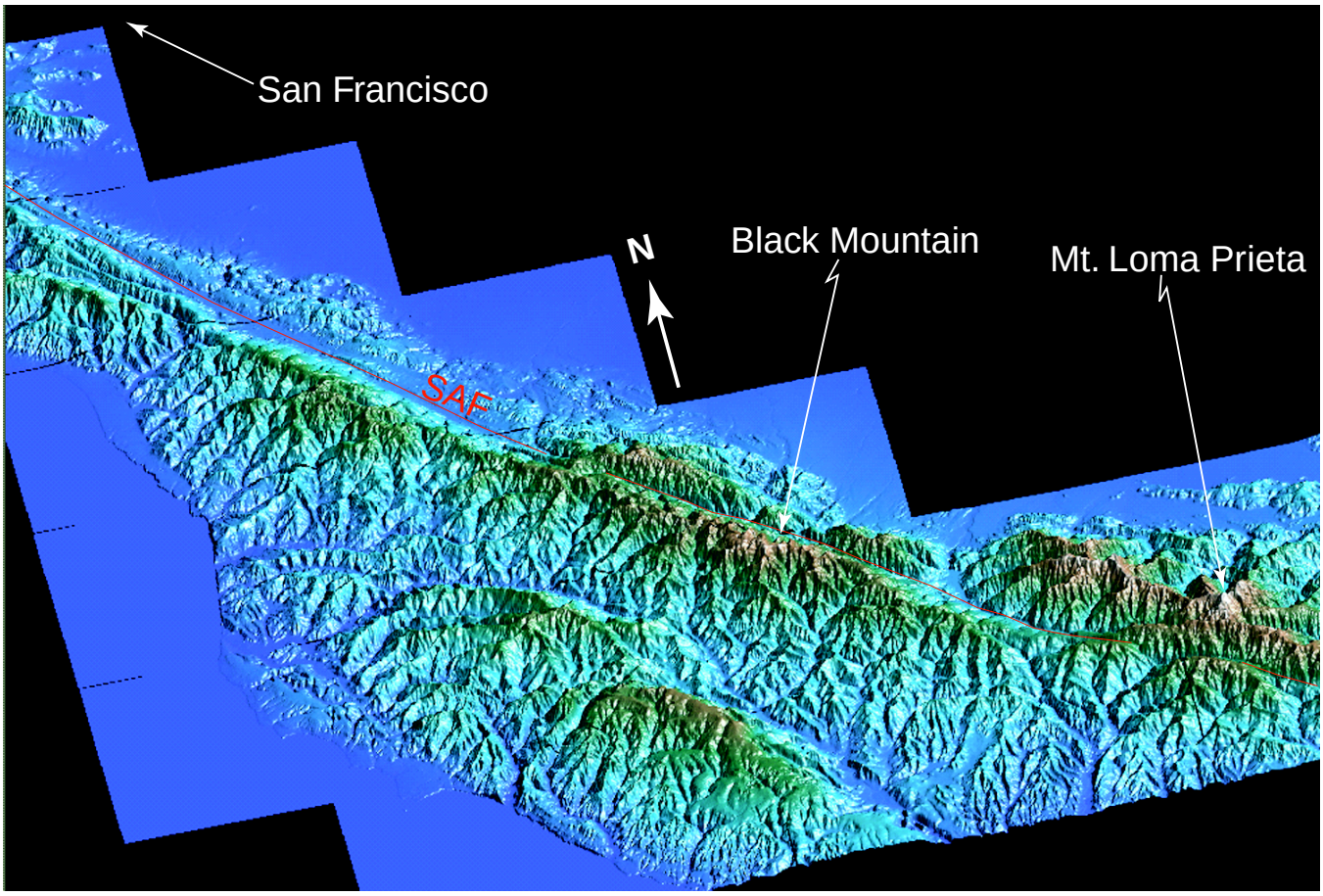

Figure 1: Three dimensional perspective view of the Southern San Francisco Bay Area. Noted on the image are Black Mountain (large deformation accomodated in this block during the 1906 San Francisco Earthquake), Mt. Loma Prieta (area of the 1989 Loma Prieta Earthquake), and the San Andreas Fault (labeled "SAF" in figure). No vertical exaggeration in this image.

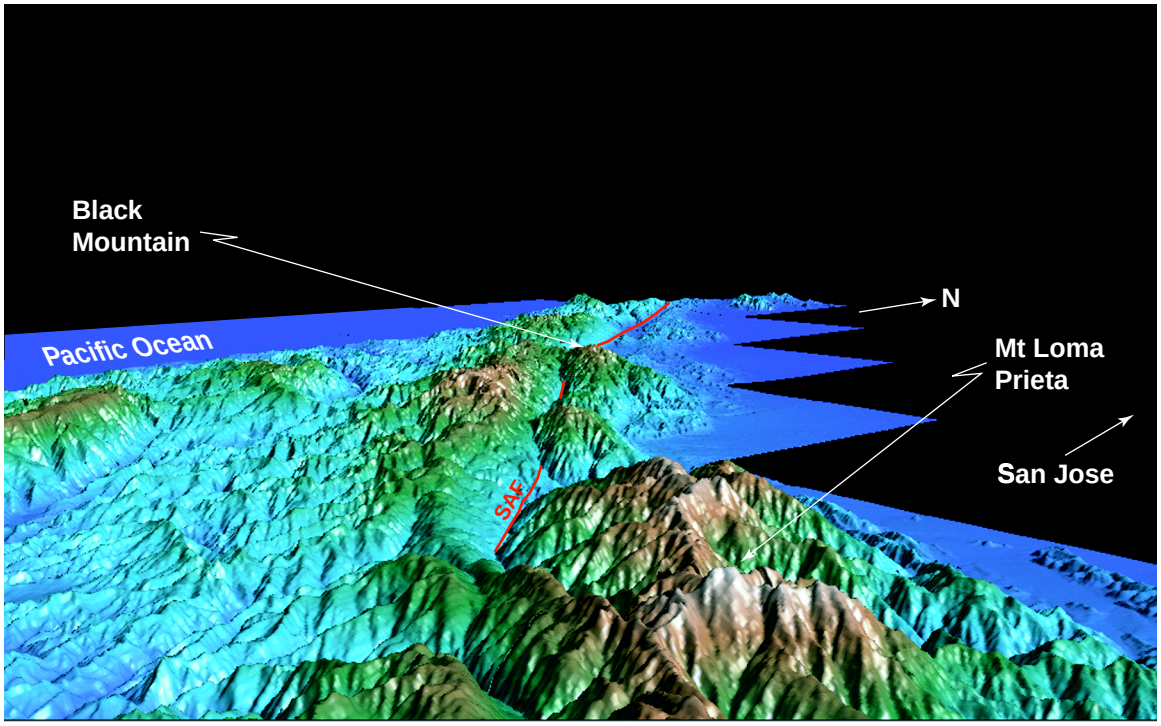

Figure 2: Prespective view of the San Andreas Fault looking toward San Francisco slightly southeast of Mt. Loma Prieta. Note the Black Mountain block and the uplifted area surrounding the San Andreas Fault.

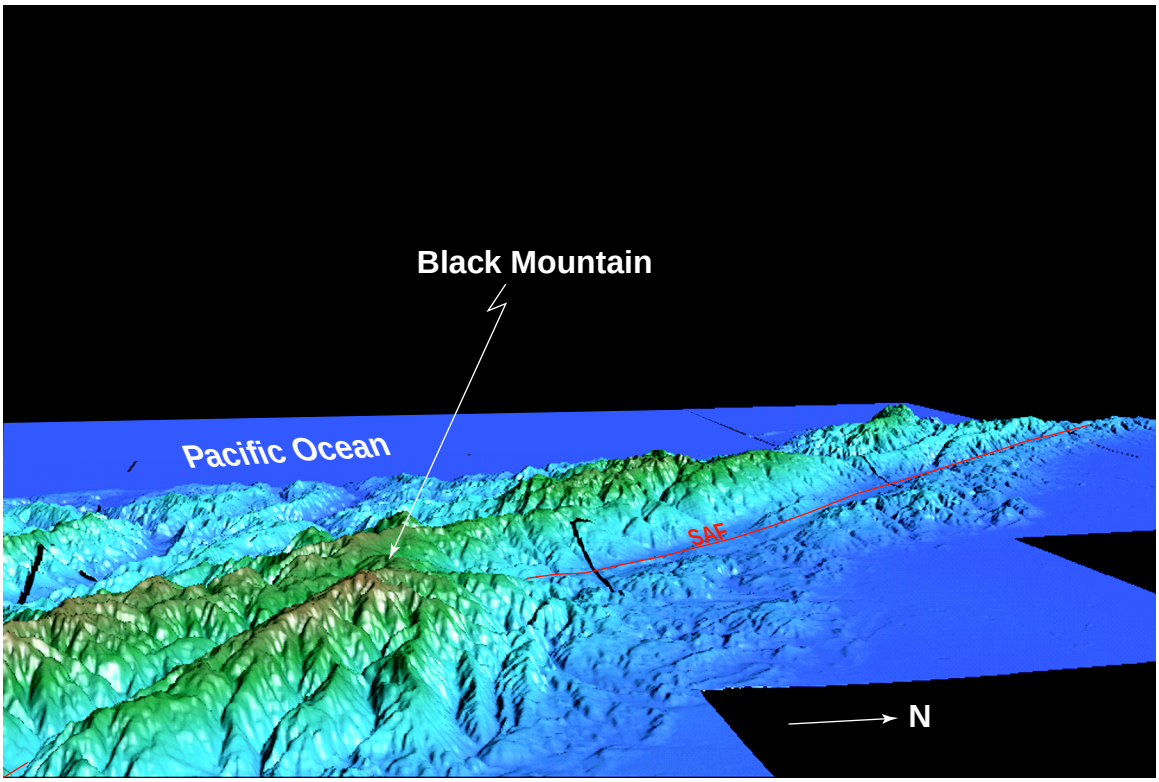

Figure 3: Perspective view of the San Andreas Fault looking west-northwest from Black Mountain. Notice the decreasing relief in this area farther away from the restraining bend near Black Mountain.

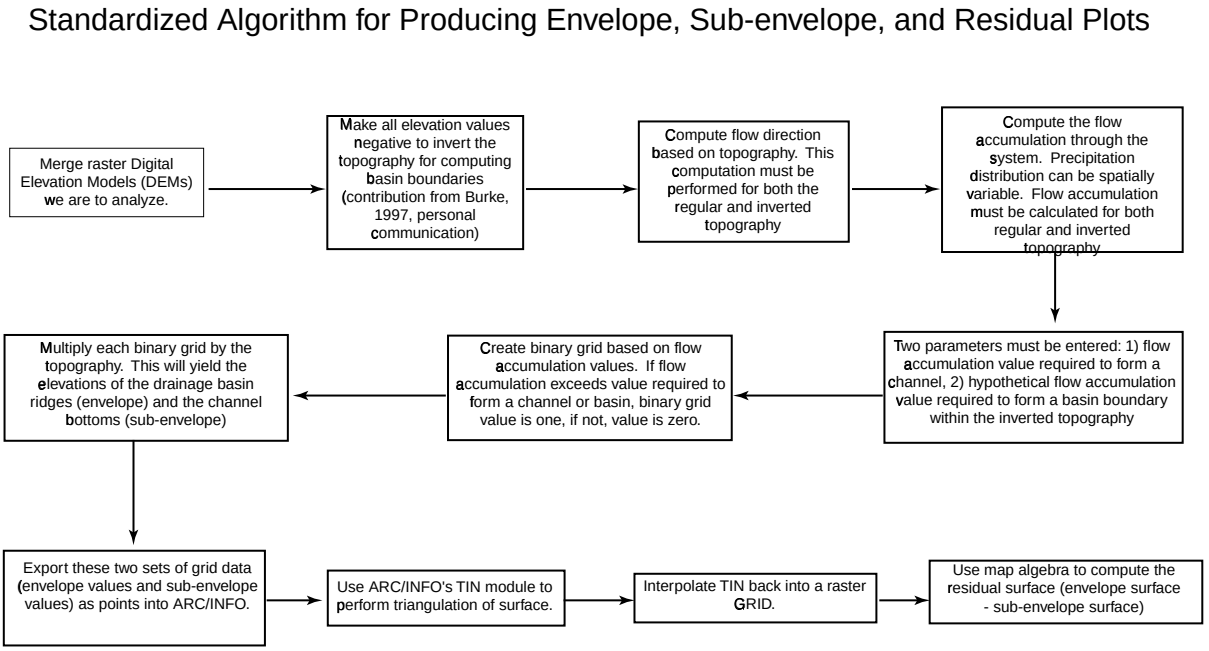

Figure 4: Schematic flowchart of our algorithm for producing envelope, subenvelope, and residual plots from Digital Elevation Models. Our algorithm has been successfully implemented in ARC/INFO.

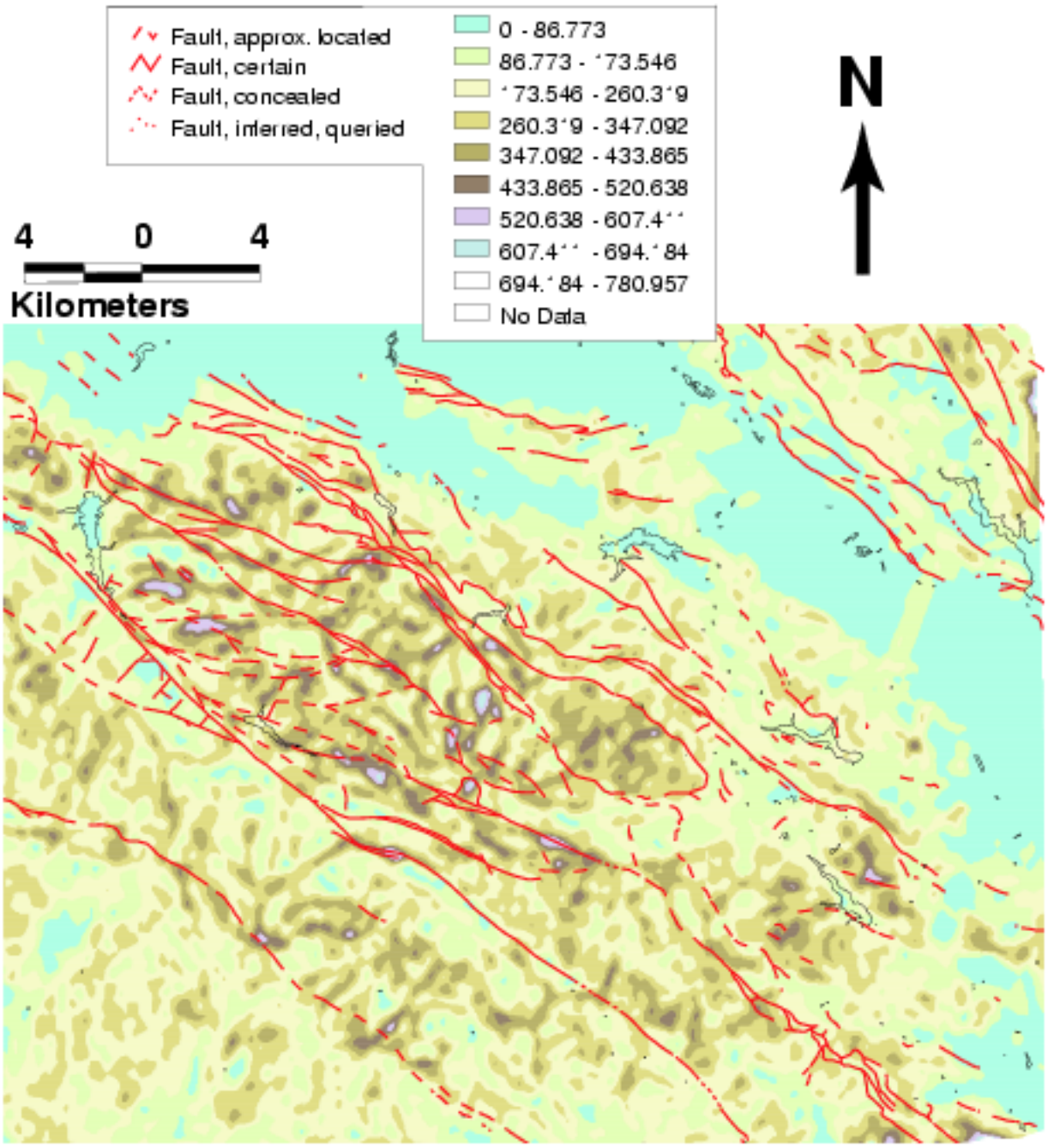

Figure 5: Values of the topographic residual in the area of Mt. Loma Prieta. High values are red, low values are blue. Notice high values of the residual east of the San Andreas Fault, near Mt. Loma Prieta. Fission track data shows a long-term rock uplift rate of approximately 1 mm/yr in this area (Bürgmann, et al., 1994). The spatial distribution of uplift and the topographic residual correlate well in this area.

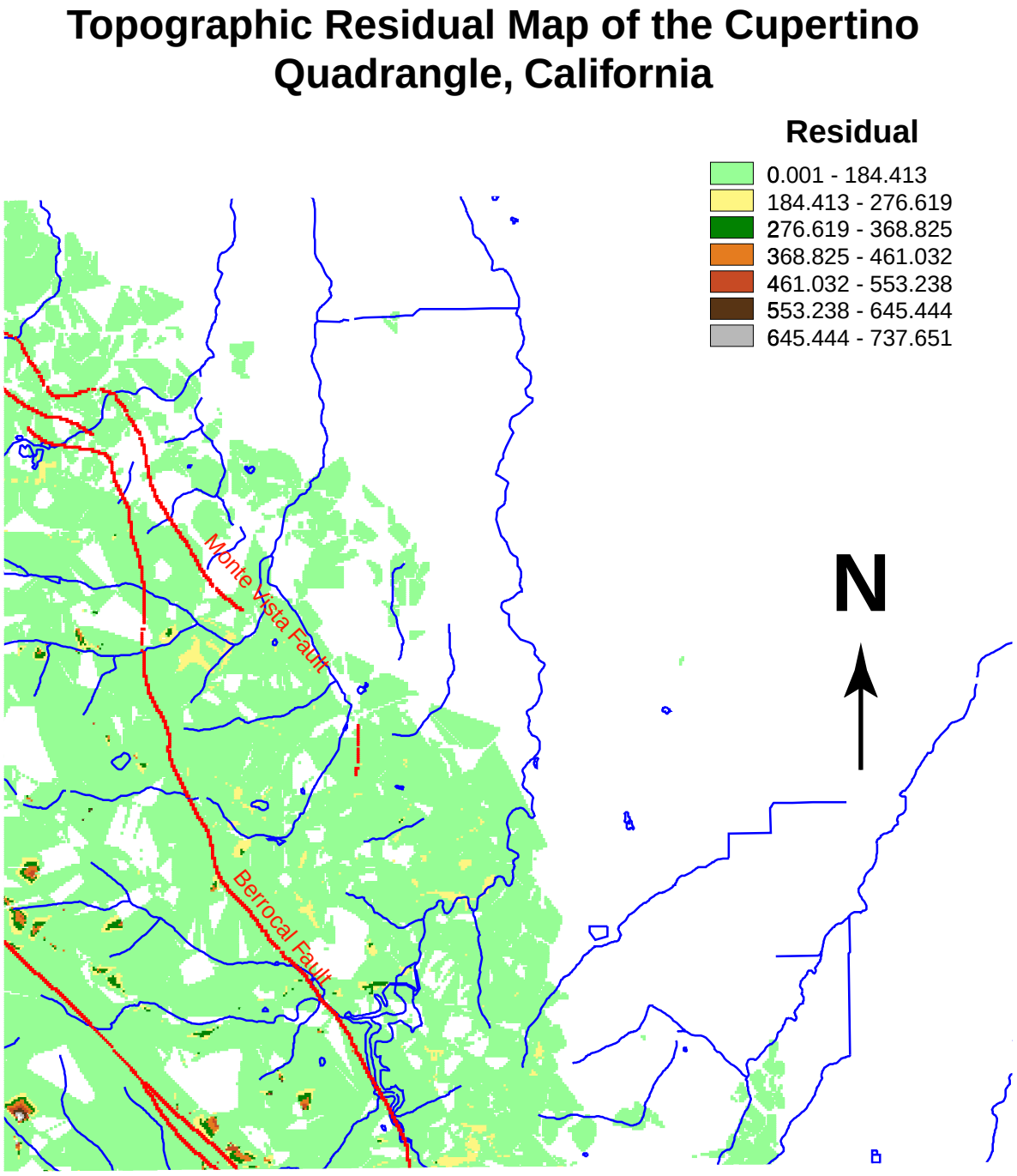

Figure 6: The topographic residual surface of the Cupertino 7.5 minute USGS quadrangle. The calculations were performed using the algorithm described in the text with channelization occuring at flow accumulations exceeding 63000 m^2. Notice the high residuals near the San Andreas Fault and near the Berrocal Fault.

Generalized Residual Map of the Cupertino Quadrangle, California

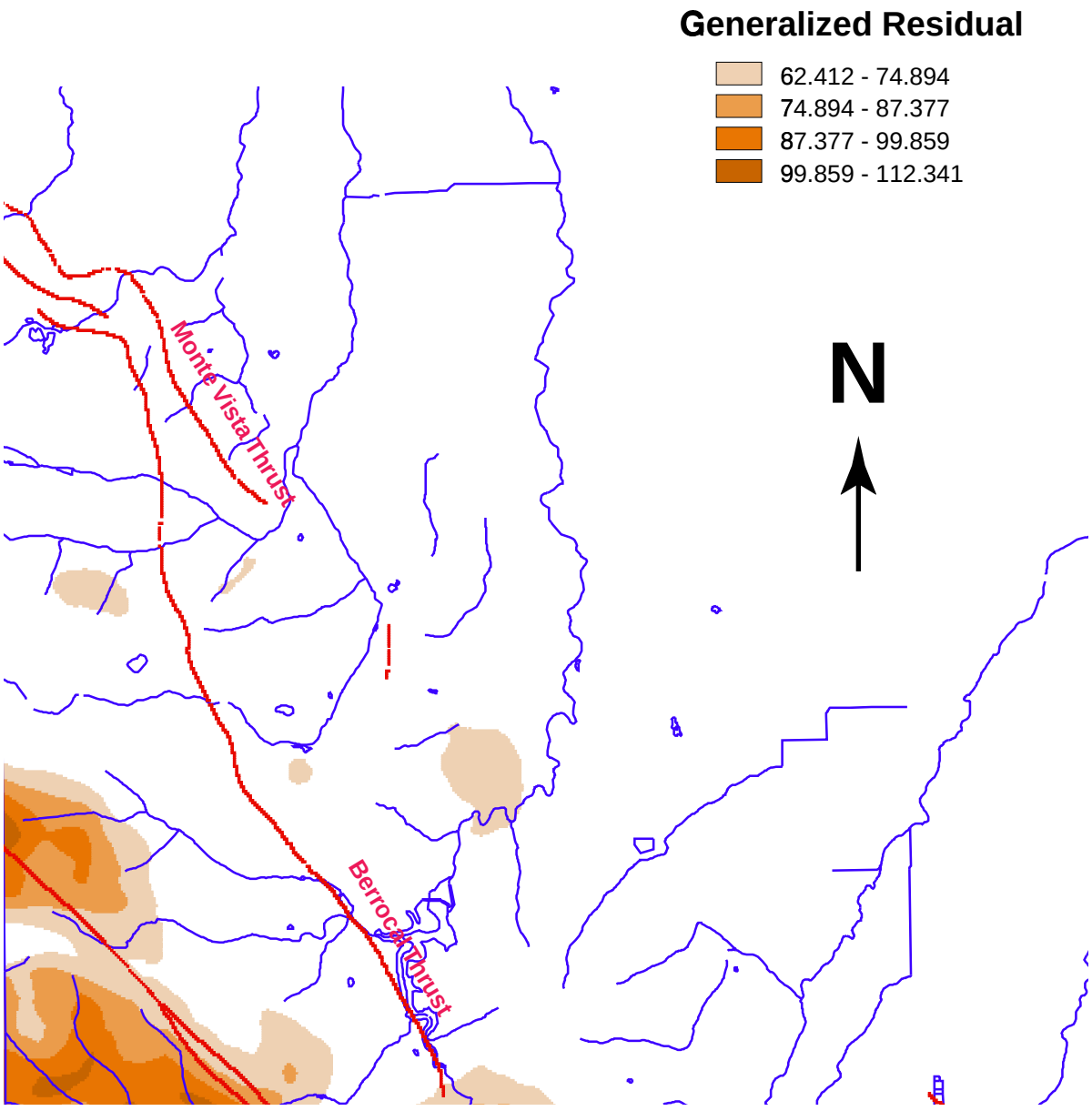

Figure 7: The "Generalized Residual" for the Cupertino 7.5 minute USGS quadrangle. This plot is derived from the residual surface plotted in Figure 6. In an attempt to highlight trends in the residual, we performed a nearest neighbor analysis in which the value of the generalized residual at any point is equal to the average of the residual values of the surrounding 250 meters.

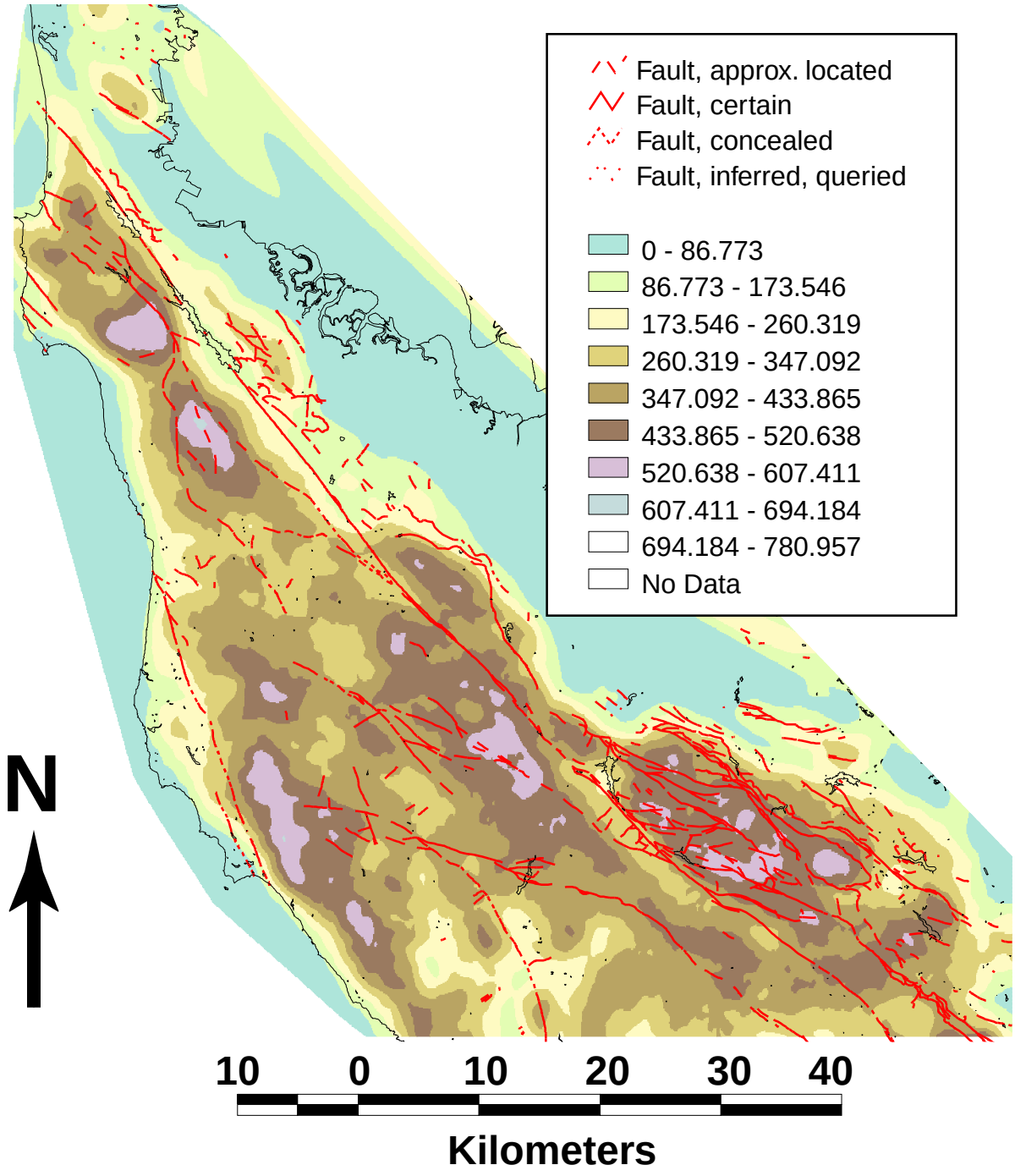

Figure 8: Generalized Residual Map of the Southern San Francisco Bay Area, California. Channels are defined by flow accumulations exceeding 63000 m^2 on the positive topographic surface. Basin boundaries are defined by flow accumulations exceeding 54000 m^2 on the negative topographic surface. The topographic residual was generalized with a nearest neighbor radial search with a search radius of 15 km.

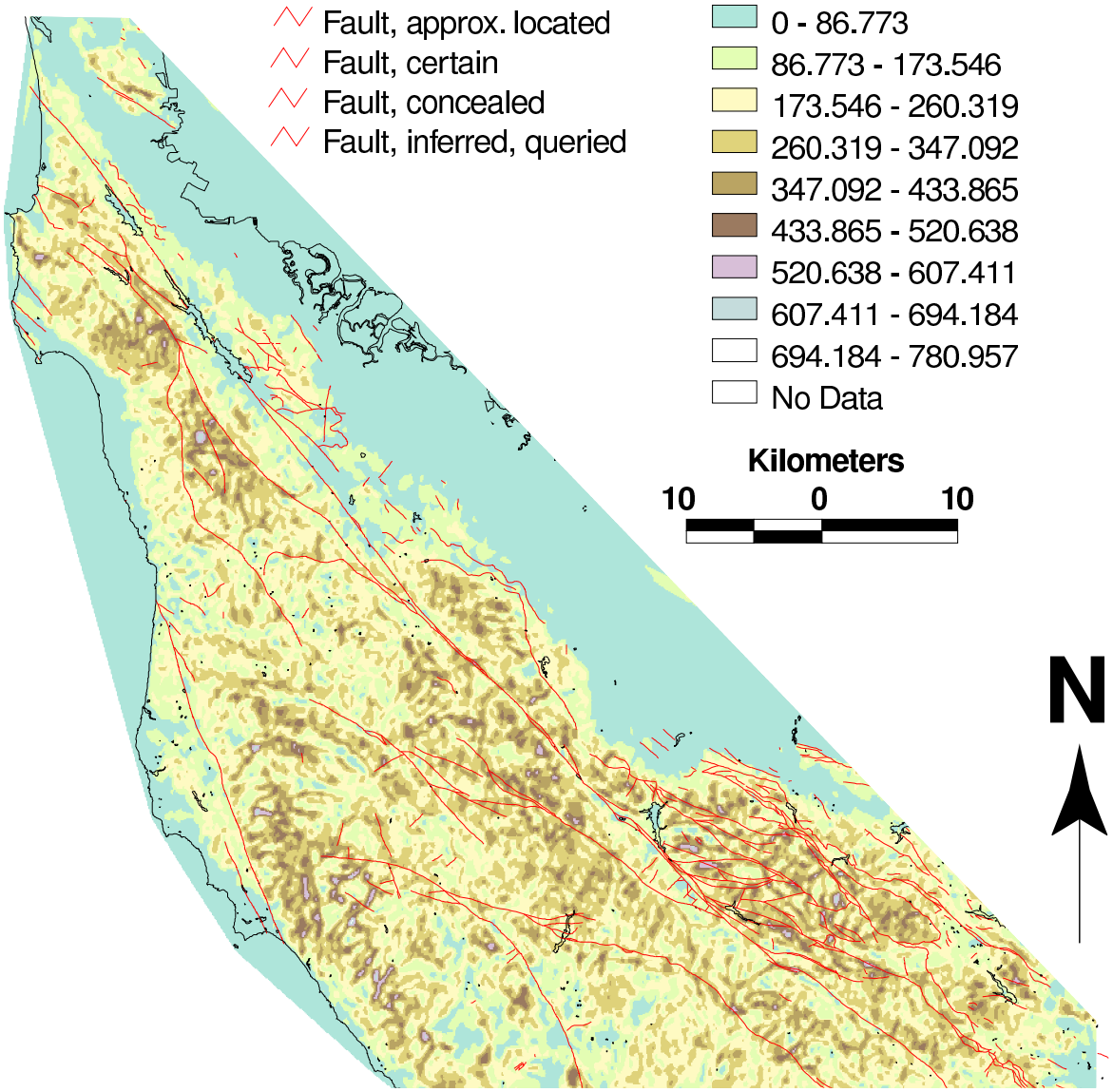

Figure 9: Residual Map of the Southern San Francisco Bay Area, California showing the setting of the detailed maps presented in Figure 10, Figure 11, and Figure 12 (southeast portion of the map). Channels are defined by flow accumulations exceeding 63000 m^2 on the positive topographic surface. Basin boundaries are defined by flow accumulations exceeding 54000 m^2 on the negative topographic surface. The topographic residual was generalized with a nearest neighbor radial search with a search radius of 1.5 km. Thus, this image highlights more detailed deviations in the topographic residual than Figure 8.

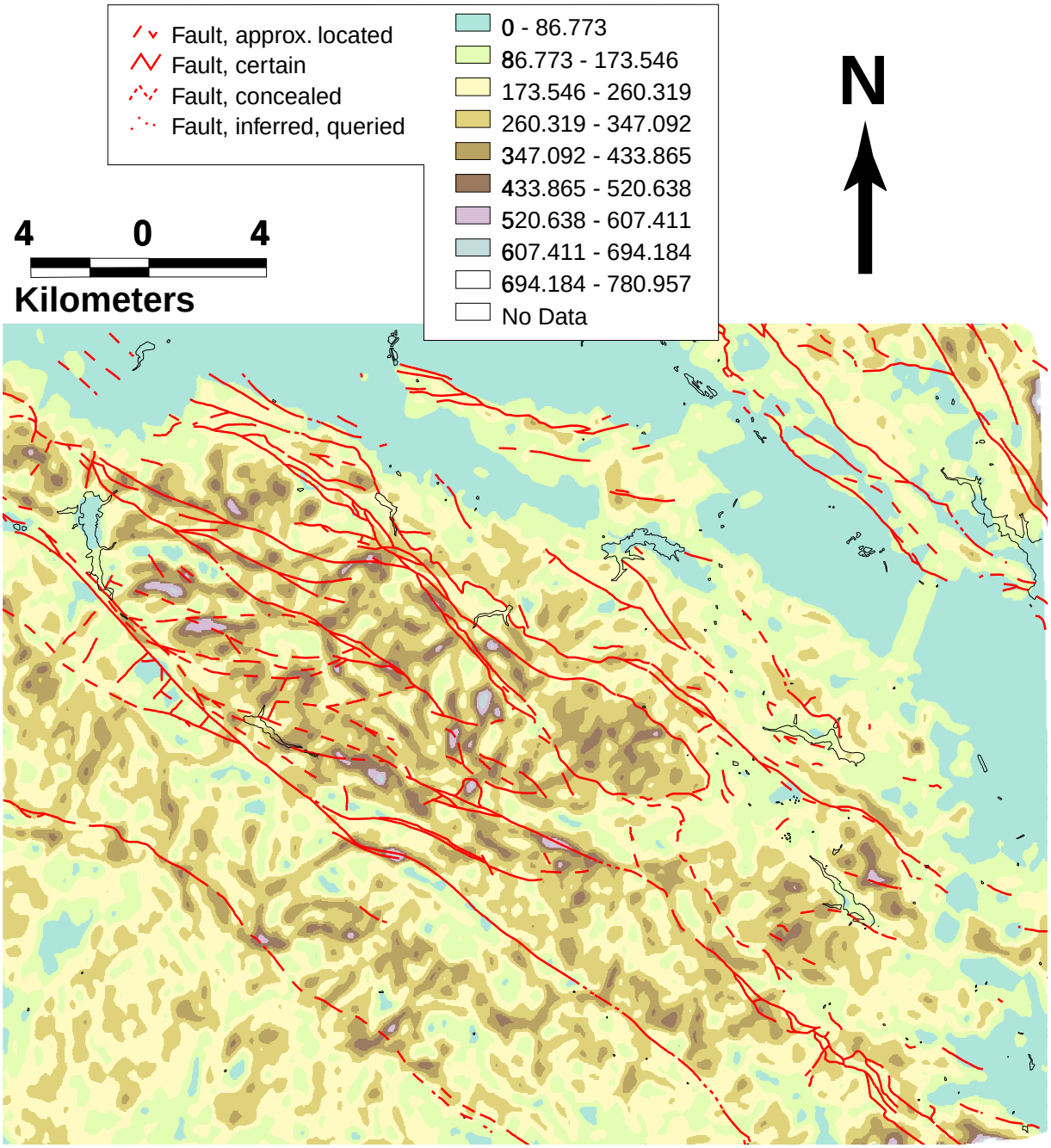

Figure 10: Residual Map of the Sierra Azul block, Southern San Francisco Bay Area, California. Channels are defined by flow accumulations exceeding 63000 m^2 on the positive topographic surface. Basin boundaries are defined by flow accumulations exceeding 54000 m^2 on the negative topographic surface. The topographic residual was generalized with a nearest neighbor radial search with a search radius of 1.5 km. Mt. Loma Prieta is situated near the epicenter of the 1989 Loma Prieta earthquake which resulted in extensive damage in the Bay Area.

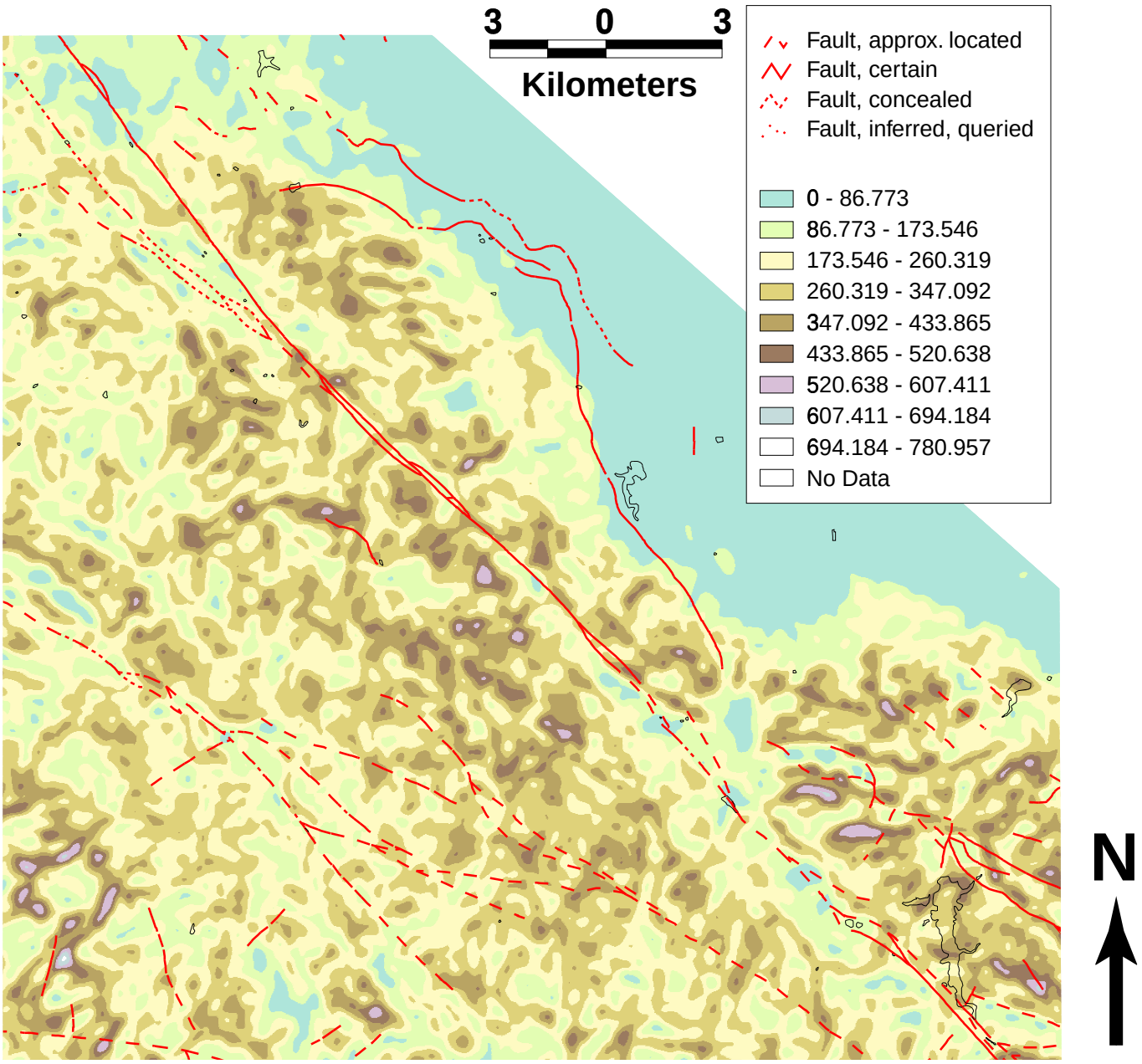

Figure 11: Residual Map of the Black Mountain area, Southern San Francisco Bay Area, California. Residual values are generally low in the area of the Cupertino embayment. The lack of correlation between field evidence in this area (recently offset alluvial terraces) and the magnitude of the topographic residual may result from gridding algorithms of the envelope and subenvelope surface. Channels are defined by flow accumulations exceeding 63000 m^2 on the positive topographic surface. Basin boundaries are defined by flow accumulations exceeding 54000 m^2 on the negative topographic surface. The topographic residual was generalized with a nearest neighbor radial search with a search radius of 1.5 km.

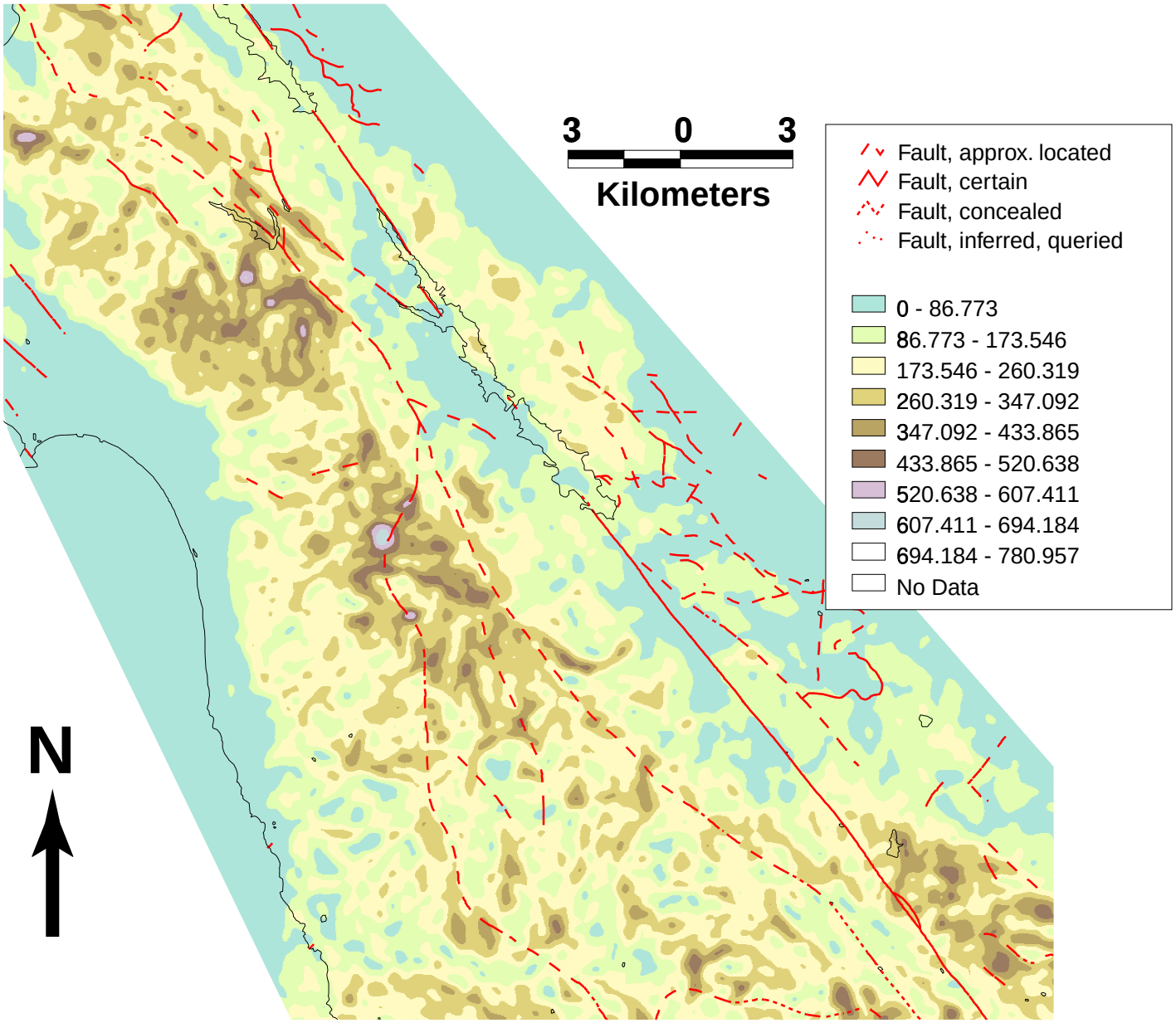

Figure 12: Residual Map of the San Mateo area, Southern San Francisco Bay Area, California. Channels are defined by flow accumulations exceeding 63000 m^2 on the positive topographic surface. Basin boundaries are defined by flow accumulations exceeding 54000 m^2 on the negative topographic surface. The topographic residual was generalized with a nearest neighbor radial search with a search radius of 1.5 km.

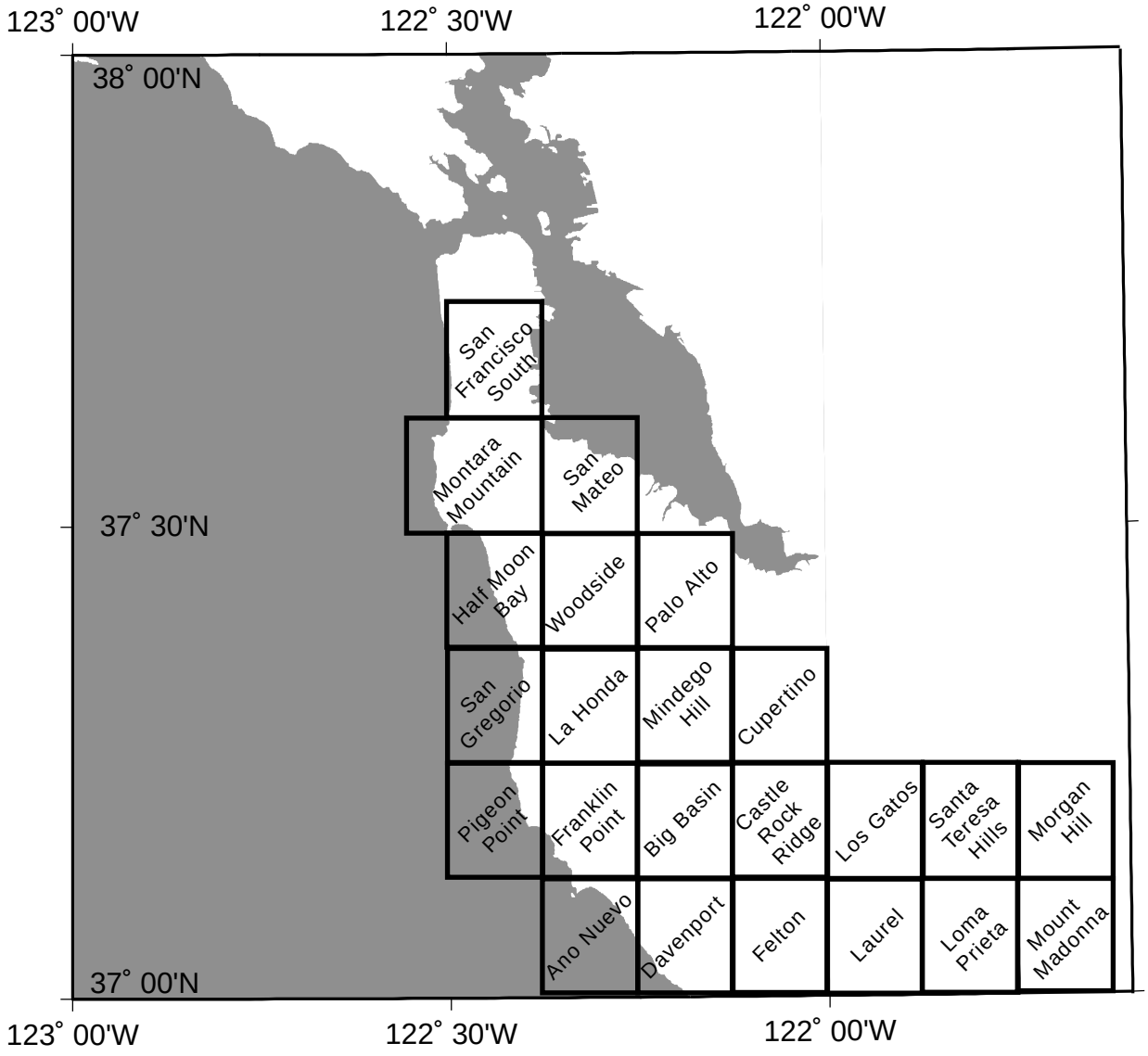

Figure 13: Index map of the Quadrangles used in calculating the morphometric indices discussed. All data were downloaded from the Bay Area Regional Database (BARD). The data used were 7.5 minute Digital Elevation models with a horizontal spatial resolution of 30 meters and a vertical accuracy of 3 meters.

5 Diffusive degradation of transport- and production-limited fault scarps, with implications for morphologic dating and landscape development in tectonically active regions

Abstract

Active faults displace rock that is subsequently modified by surface transport processes. The morphology of a fault scarp depends on the tectonic and geomorphic processes acting along and around the fault. To understand landform and landscape development around active scarps, we consider a landscape dominated by tectonic displacements produced by movement along a fault, diffusive geomorphic transport of regolith, and the steady production of regolith from bedrock. The degradation of fault scarps may be dominated by either transport-limited, in which case excess transportable material exists relative to the transport capacity of the geomorphic system, or production- limited conditions, in which the transport capacity exceeds the amount of material available for transport and bedrock is exposed. For transport-limited scarps, scarp morphology is dependent on the tectonic displacement rates and the hillslope diffusivity. In contrast, production-limited scarp morphology primarily depends on the tectonic displacements and rates of conversion of bedrock to regolith. We find that for typical regolith production rates, a steady-state condition where the surface topography of the scarp and the location of soil–bedrock interface do not vary with time, is never achieved. We propose the following possibilities for short and long term scarp development: 1) Scarp development will remain transport-limited for the duration of the faulting if the tectonic rates are slow, the tectonic displacements are short lived, or the thickness of transportable material is large. 2) The scarp will change from transport- to production-limited if moderate (> 1 mm/yr) tectonic uplift rates are sustained for an amount of time sufficient to expose bedrock. The time at which the scarp becomes production-limited will depend on the initial thickness of transportable material and the diffusive transport rate. 3) Under the special circumstance of high bedrock production rates and low rock uplift rates (< 1 mm/yr), transport-limited conditions may be persist.

Faults slipping at rates for which the rock uplift rate exceeds 1 mm/yr will usually be driven into production-limited conditions. Because steady-state topography is never achieved along production-limited diffusive scarps, the exposure of bedrock in a diffusive system prohibits the development of steady-state topography. While topographic steady-state may be reached in active mountain belts, this condition requires the action of different geomorphic transport and production processes than those we investigate. Therefore, landscapes in which the hillslope transport is dominated by diffusive transport processes are transient features and rarely evolve towards a pure steady-state condition.

5.1 Introduction

The transport of material along unchannelized hillslopes, and hence changes in the hillslope morphology accelarates with increasing relief. This relief is produced by either drainage incision or differential tectonic uplift. Drainage incision may result from climatic fluctuations, geomorphic capture, crossing of geomorphic process thresholds, and exposure of different lithologies, while tectonic displacements may result from plate boundary forces, isostatic adjustment of the crust, thermal buoyancy of the upper mantle and corresponding flexure of the crust, fault slip, or displacements associated with flexure due to sediment loading. Drainage incision and tectonic displacements effect the development of unchannelized hillslopes in different ways. Incision acts to remove material from the base of a hillslope, which accelarates transport at progressively higher points on the hillslope over time. In contrast, tectonic displacements may steepen slopes anywhere along the hillslope, causing material to be redistributed from areas of uplift to those of subsidence (Figure 14). In addition to incision and tectonic displacements, the exposure of bedrock may also effect a diffusive hillslope's morphology. When only unconsolidated rocks exist for transport, the transport capacity is less than the material available for transport. We refer to these slopes as transport-limited. However, when bedrock is exposed, the available transport capacity may exceed the amount of material available for transport, and so the slope is production-limited. In this case, transport takes place only when transportable material is produced from the bedrock.

We strive to understand the geomorphic response of the diffisive hillslopes to deformation by using field observations of the deformation and landforms around active faults to construct a numerical model that captures the interaction of the surface deformation due to faulting and the geomorphic redistribution of material. We use this simple model to explore the topographic response of the earth's surface to faulting for a wide range of geomorphic and tectonic rates and geometries that includes most environments in which diffusive transport apparently acts. Finally, we examine the transition of scarps from transport- to production- limited conditions in actively uplifting regions. This transition exerts a fundamental control on the landscape, so its characterization is necessary to understand the morphological development of fault scarps and hillslopes in tectonically active areas.

5.2 Geologic and Geomorphic Observations of Alluvial and Bedrock Scarps

A fault scarp is a tectonic landform where the fault plane, or a zone of interconnected fault segments intersects the land surface [Stewart and Hancock, 1990]. Fault scarps may be formed by offsetting material available for geomorphic transport, or bedrock that is not easily transported by geomorphic processes prior to mechanical and chemical disaggregation. The former case describes transport-limited scarps, whereas the

later are considered production-limited. The morphology of transport-limited scarps is controlled primarily by the rate at which material can be transported, whereas production limited scarp morphology is controlled by the production rate of transportable material from bedrock.

The morphology of transport- and production-limited scarps can be markedly different (Figure 15). Fresh transport-limited scarps show a steep face that is dominated by gullying and mass failure. Usually mass failure reduces these slopes to the internal angle of friction of the material soon after rupture (Figure 15a). This transport results in the deposition of material at the base of the scarp. Following degradation of the scarp by mass failure, material in channels and gullies is transported by fluvial processes, whereas local hillslope processes transport material across the scarp in the interfluves. Where gullying and channelization are not important, the scarp typically shows a smooth profile, with a convex-up form on the upper part of the scarp and a concave-up form on the lower slopes of the scarp (Figure 15b). These types of forms typically arise when local hillslope processes such as bioturbation, soil creep, and rain splash are the dominant transport mechanism of material. The transport of material downslope results in removal of material from the top of the scarp and deposition of material at the base of the scarp. This transport takes place as the scarp is steepened by further rupture along the fault, which starts the process anew.

Transport-limited scarps within the Basin and Range tectonic province of the United States have been used as a model for the morphologic development of these types of scarps. This tectonic environment is primarily an extensional environment with normal dip-slip motion creating most of the differential uplift along the scarps. The 1954 $M_s = 6.8$ Dixie Valley, Nevada and the 1983 $M_s = 7.3$ Borah Peak earthquake in Idaho are two well studied ruptures. The ground rupture pattern in the Borah Peak earthquake included over a dozen faults and up to 10 tension cracks in up to an 85 m wide complex horst-and-graben zone [McCalpin, 1996]. Where the differential uplift pattern may vary significantly between events, scarp morphology may be complex. However, some locations along the fault may have relatively constant uplift distributions from event to event. In these locations, fault scarp morphology can be understood in terms of repeating uplift patterns resulting from rupture. Schwartz and Hanks [1987] used the morphology of the upper edge of the Borah Peak rupture to estimate the timing of the penultimate event along the fault. This age corresponded remarkably well with the trench-determined numerical ages, using reasonable sets of geomorphic rates.

Offset landforms along strike-slip faults may be used to determine rates of motion along the fault in places where the initial landform geometries can be inferred. Arrowsmith *et al.* [1998] used a series of gullies in the Carrizo Plain to calibrate the transport constant for the area and then applied this transport rate to landforms farther south in the Carrizo Plain. The calibration study showed that slope steepening at the fault as shutter ridges are translated away from their parent interfluves may be used to understand rates of motion along strike slip faults.

Production limited scarps do not display the smooth morphology typical of transport-limited scarps (Figure 15). In this case, rupture or continuous movement along the fault may expose bedrock. This material cannot be transported by geomorphic processes until it is converted to transportable material by chemical dissolution and mechanical abrasion. Therefore, the fault scarp often is expressed as a bedrock cliff that may have structural kinematic indicators of motion along the fault. With time, the bedrock face of the scarp is converted to transportable material and transported downslope into the colluvial pile at the base of the scarp. Material may also be transported to the base of the scarp by gravity failure along preexisting mechanical weaknesses such as fractures. In this process, rock topple and mass failure may act to degrade the scarp. Where these processes are not significant, the scarp can retain its geometry for long periods of time in places where the production rate of transportable sediment from bedrock is low. Further movement along the fault acts to increase the height of the bedrock scarp face. However, the isolation of transportable material at the top of the scarp from the bottom may prevent slope steepening at the scarp face from accelerating the amount of sediment moving to the base of the scarp.

Production-limited scarps may yield information about low tectonic rates and the timing of movement along old faults. Bedrock fault scarps are less susceptible to erosion than those formed in unconsolidated materials. Therefore, they preserve evidence of tectonic activity for longer time periods [Mayer, 1986]. Machette [1986] observed that one-meter high scarps of about 100 ka age are rarely seen in the Basin and Range province in western North America. In Sonora, Mexico, the Pitaycachi fault scarp developed in basalt appeared to have been almost completely obliterated in as much as 200 ka since the penultimate event [Bull and Pearthree, 1988]. Therefore, bedrock fault scarps may be the only evidence to evaluate faults with low slip rate and long recurrence intervals where there were no offset unconsolidated sediments or where such offset sediments were not preserved.

5.3 Conceptual and Numerical Model of Scarp Degradation

Based on our observations of fault scarps, we can build a conceptual model of how the topography and stratigraphy around faults develop (Figure 16). For transport-limited scarps, rupture events produce differential uplift in the vicinity of the fault. Directly following rupture, mass movement of sediment down slope reduces the scarp slope angle to the internal angle of friction of the material. Following mass movement, transport processes such as fluvial transport, debris flows, shallow landsliding, soil creep, bioturbation, and rain splash act to transport sediment towards the base of the scarp. Where shallow landsliding is an unimportant transport process along the interfluves of the scarp, transport will result from local hillslope processes such as rain splash, soil creep, and bioturbation. These processes transport sediment down the fault scarp

to form a colluvial pile at the base of the scarp (Figure 16a, top panel). With several rupture events, wedges representing the downslope transport of material following the rupture may form at the base of the scarp. As the number of rupture events and the total amount of time during which the fault moves increases, the individual events appear continuous and may be expressed as a continuous slip rate. After cessesion of faulting, the topographic form of the scarp degrades as the slopes are reduced by geomorphic transport, but not steepened by tectonic uplift (Figure 16a, bottom panel). With enough time, all topographic evidence of faulting will be erased.

Production-limited fault scarps expose bedrock, leading to different scarp development than transport-limited fault scarps. When bedrock is exposed, the amount of material available for transport is insufficient relative to the transport capacity of the system. Therefore, transport can only take place as bedrock is converted to transportable regolith (Figure 16b). Transport processes in these environments include those acting over transport-limited scarps. In addition, transport of material by bedrock landsliding may also be important in these environments. Production of transportable material from bedrock may take place by mechanical failure and subsequent transport of material by rock topple, steady chemical disaggregation of bedrock, and mechanical abrasion of bedrock. In many areas, rock topple and bedrock landsliding may not be important. In these areas, steady production of transportable material from bedrock results from chemical disaggregation and mechanical abrasion. As regolith is produced from bedrock, it is transported towards the base of the scarp (Figure 16b, top panel). In interfluves where landsliding and topple do not transport material, creep, bioturbation and rain splash move material across the scarp.

We propose the following conceptual model for production-limited scarp development in areas where topple and bedrock landsliding are not active in the interfluves. First, movement along the fault may expose bedrock (Figure 16b, top panel). The exposure of bedrock at the top of and along the fault scarp isolates the transport of material at the top of the scarp from the colluvial pile formed from events prior to the exposure of bedrock. As bedrock is converted to regolith over time, the transportable material is moved downslope to the colluvial pile. Continued motion along the fault produces more relief; however, the exposure of bedrock isolates the material at the top of the scarp from the bottom, so transport may not accelerate due to slope steepening. With time, the colluvial pile may thin if a small amount of transportable material is produced from the bedrock scarp relative to the rate at which material is transported away from the scarp. Finally, with the cessesion of fault movement, the exposed bedrock is steadily converted to transportable material, and eventually the slopes will be reduced, perhaps returning to transport-limited conditions (Figure 16b, bottom panel).

In the following sections, we build a numerical model based on these ideas of fault scarp development. These models are then used to understand what processes and sets of rates are important controls on the

morphology of fault scarps. We characterize geomorphic and tectonic processes by coupling constitutive equations (transport laws for geomorphic processes and rheological properties for tectonic processes) with the equations of continuity.

5.3.1 Tectonic Processes

Displacement of the earth's surface can be caused by slip along a fault and the resulting deformation around the fault, folding caused by movement along a fault at depth, and distributed folding with no discontinuities in the deformation field. The mode of deformation will depend on the loading magnitudes, rates, the temperature, and the rheology of the upper crust. In our simple model of tectonic deformation, we assume that the cool upper crust can be approximated by a brittle linear-elastic rheology that deforms in response to slip along and opening of discontinuities in the elastic medium

We model the tectonic surface displacements due to movement along a brittle fault by embedding a dislocation in an elastic half-space and letting it slip a prescribed amount. The geometry of the fault can be expressed as two parameters, the fault dip, β, and the down dip length of the fault surface, L. We assume that the fault is infinitely long in the out of plane dimension to eliminate the edge effects of the tips of the fault in two dimensions (Figure 17a). The slip along the fault is described by the Burgess vector, which measures the relative displacement along the fault. A positive Burger's vector on a fault dipping less than 90 degrees indicates thrust motion, while the opposite indicates normal motion on the fault.

Given these three parameters, the surface displacements can be computed by summing the effects of two oppositely oriented, infinitely long dislocations, one of which starts at the upper edge of the fault (μ in Figure 17a), and the other which starts at the lower edge of the fault (λ in Figure 17a).The equations for relating surface displacements to fault geometric parameters are [Du *et al.*, 1994]:

$$U_x = -\frac{1}{\pi}\left\{b_x \tan^{-1}(d) + \frac{b_z - b_x d}{1+d^2}\right\} \tag{1}$$

$$U_z = -\frac{1}{\pi}\left\{b_z \tan^{-1}(d) + \frac{b_x + b_z d}{1+d^2}\right\} \tag{2}$$

where, U_x is the horizontal displacement at the free surface (L),

U_z is the vertical displacement at the free surface (L),

b_x is the horizontal component of the Burger's vector (L),

b_z is the vertical component of the Burger's vector (L),

and d is the geometric parameter.

The geometric parameter locates the tip of the dislocation to the point of interest along the free surface:

$$d = \frac{(x - \xi)}{\zeta} \tag{3}$$

where x is the horizontal coordinate of the surface point of interest (L),

ξ is the x coordinate of the tip of the dislocation (L),

and ζ is the vertical coordinate of the tip of the dislocation (L).

Finally, the dip of the dislocation is defined by the magnitudes of the components of the Burger's vectors. We define ω as the compliment of the dip angle, β. Therefore, the components of the Burger's vector are $b_x = b \sin\omega$ and $b_z = b \cos\omega$.

Surface displacements are determined by summing the displacements U_x and U_z due to the two oppositely oriented dislocations defining the slip patch. By repeating this calculation for many points along the surface, we can approximate the surface displacement field due to slip along the simulated fault. Although these equations relate fault slip to surface displacement, they may also be used to compute surface displacement rates by expressing the slip along the fault as a slip rate.

5.3.2 Geomorphic Processes

The simplest imaginable landscape produced by faulting and the response to deformation is on e in which a single geomorphic process acts to redistribute material through the landscape, and a simple process converts bedrock to transportable regolith. First, mass conservation requires that the change in the mass at a point in a small amount of time is equal to the difference in the mass flux entering and leaving that point:

$$\frac{\partial m}{\partial t} = \nabla Q_m = \nabla Q_v \rho_s(x, y, t) \tag{4}$$

Assuming that the density of sediment does not significantly change during transport, this mass flux can be rewritten as a volume flux:

$$\frac{partialz}{partialt} = \nabla Q_v = \nabla Q \tag{5}$$

This equation is also known as the continuity equation. We use a transport law to describe how the sediment flux (Q) varies in space and time. In order to simulate the transport of material across the fault scarp, we consider transport processes such as bioturbation, rain splash, and sheet wash as the primary means of material transport. Based on the morphology of abandoned Lake Bonneville shorelines and abandoned fluvial surfaces, Gilbert [1880] postulated that the flux of material through a point along an unchannelized hillslope is proportional to the local slope (Figure 17b):

$$Q_s = -\kappa \nabla H \tag{6}$$

where, Q_s is the flux of material moving through a point (L^2/T),

κ is the transport constant (L^2/T),

and H is the topographic elevation (L).

Since that time, numerous studies show that this transport law well-represents these processes on unchannelized slopes devoid of landslides. This type of transport is known as diffusive transport. By combining transport laws such as those quantified by Equation 6 with the continuity equation, we can understand how topography develops with time. Using the simple diffusive transport law and assuming the transport constant does not vary in space, the change in elevation per unit time is written as:

$$\frac{\partial H}{\partial t} = -\kappa \nabla^2 H \tag{7}$$

The rate at which material moves downslope is scaled by the transport rate, or diffusivity, κ (Figure 17b). This transport rate has been determined to be between 0.04 and 0.0004 m^2/yr and may vary with climate, aspect, density of vegetation, and other factors.

It is clear that these processes are not exclusively active along an active fault. However, between gullies where flow is channelized, this "diffusion" of material may be the dominant transport mechanism. On the other

hand, a well established geomorphic system will have a system wide response, with the diffusive response coupled to the fluvial and slope failure response to the uplift. As a first order problem, we do not consider the coupled response of several geomorphic processes to the uplift. While models exist which explicitly treat each of the different geomorphic processes, we feel it is valuable to understand each processes response before understanding the response to uplift of the entire geomorphic system.

Transport of material can only take place when there is sufficient sediment to transport. In the case that $\partial H/\partial t$ exceeds the thickness of transportable material, there is excess transport capacity of the system relative to the available sediment. Therefore, the transport process acts to remove all sediment available for transport, but fails to transport at full capacity. In the case that the transport capacity exceeds available material, the flux of material moving downslope at the point that production-limited conditions exist is computed by moving the material available for transport, H_B (where B is the elevation of the bedrock) out of the area:

$$Q(x,y) = \frac{H(x,y,t) - B(x,y,t)}{\partial t} \partial S \tag{8}$$

where S is the horizontal length parallel to the transport direction.

We then iteratively recompute all the fluxes to calculate the change in elevation across parts of the landscape which may be either transport- or production-limited.

The other geomorphic process that we consider is the transformation of bedrock to transportable material. Carson and Kirkby [19722] postulate that regolith production rates due to mechanical weathering are highest at the surface, and decay exponentially with depth. This idea is supported by measurements of production rates at different depths. The production rate with depth is described by the surface production rate, B_a, and the thickness sensitivity, B_b (Figure 17b, bottom panel):

$$\frac{\partial H_b}{\partial t} = -B_a e^{-B_b(H-H_b)} \tag{9}$$

where, H_b is the elevation at the top of the bedrock (L),

B_a is the production rate of regolith when bedrock is exposed (L/T),

and B_b is the thickness sensitivity of production rates (1/L).

In this formulation, the production rate of transportable material is largest when the bedrock is exposed and declines as the thickness of transportable material increases. Larger surface production rates result in faster conversion of bedrock to regolith along the entire profile, whereas smaller values of the thickness sensitivity allow production rates to remain larger with depth than do large values of B_b. Measurements using cosmogenically produced ^{26}Al and ^{10}Be by Heimsath *et al.,* [1998] infer $B_a = 8 \times 10^{-5}$ m/yr and $B_b = 2$ m^{-1}.

Other formulations relating production rate with depth have been proposed. These production functions typically have maximum production rates below the surface and decreases as both bedrock is exhumed closer to the surface and is buried to a depth greater than the depth where the production rate is at a maximum. This production function may operate where chemical disaggregation may be as important as mechanical abrasion. In this study, we focus on the simple, exponentially declining production function, and discuss the implications of "humped" production curves.

5.3.3 Coupled Tectonic and Geomorphic Model

Our models of tectonic deformation, geomorphic transport, and production of regolith from bedrock can be combined to understand the influence of various processes and rates on the morphologic development of scarps. First, we assume that all transport takes place along a cross-section (*i.e.,* there is no out-of-plane movement of material). This allows us to reduce our geomorphic transport model to a one-dimensional system in which the topographic change over time is proportional to the slope in the profile direction and the transport constant. This situation represents an infinitely long scarp in the out-of-plane direction. Then, we assume an initial topographic surface and regolith/bedrock interface elevation. In our models, the initial topographic surface is assumed to be flat at the start of the model to isolate the effects of tectonic deformation from preexisting topography. Next, boundary conditions are prescribed, which describe how material can be moved in and out of the model space at the boundaries. Calculations of the surface topography over time are made by descritizing the topography into a one-dimensional finite difference grid to compute the solutions in space and time to the partial differential equations presented above. The finite difference grid is constructed by evaluating the elevation at regularly spaced points along the profile and adjusting their elevations by the equations described in the previous two sections.

First, the fault may slip in discrete events or continuously. If the fault slips discretely, displacements resulting from the characteristic fault slip are added to the profile length (x) and elevation (z) values when the model time since the last rupture exceeds the recurrence time of the fault. In the case of a continuously slipping fault, displacements are added during every time step of the model. After displacements have been added to the topographic profile and location, the finite difference grid is interpolated to calculate the new elevation

values at the original finite difference grid locations. Following re-sampling, we compute the local slope along each point in the profile and employ our transport law (Equation 6) to compute the volume flux of sediment between each finite difference cell. We then compute the potential change in elevation by applying the boundary conditions and the continuity equation (Equation 5). Where the potential elevation change exceeds the amount of material available for transport, the downslope flux is recomputed as described in the geomorphic processes section. The adjusted change in elevation is then subtracted from the profile elevation. Finally, the regolith/bedrock interface is lowered by the amount described by our bedrock production law (Equation 9). The time is then incremented by an amount sufficiently small to maintain numerical stability, and the calculation is repeated until the end of the model scarp development.

We can gain insight into the importance of processes and how they relate to one another by expressing the domain space and solution in terms of dimensionless parameters. We normalize aspects of fault scarp development in order to understand how the development of faults of different spatial scales relate to one another. First, we express the total displacement field as a function of the fault slip (or alternately, the fault slip rate), the down dip length of the plane that intersects the surface and extends to the bottom of the fault, and the percentage of this place that doesn't slip (Figure 18a). The surface displacements due to slip along a fault scale linearly with the magnitude of slip along the fault (Equations 1 and 2). Therefore, the magnitudes of the surface displacements can be normalized to the fault slip. Alternately, the surface displacement rate can be normalized to the fault slip rate. Next, we note that the location of a given displacement vector is controlled by the geometric parameter, d. Therefore, the displacement gradient can be normalized to some spatial dimension by normalizing the geometric parameter to this dimension.

First, we consider a straight fault with a dip of ω. This fault starts at the point (ξ, ζ). The location of the upper fault termination and lower fault termination can be written as d_1 and d_2, respectively:

$$d_1 = \frac{x - \xi}{\zeta} \tag{10}$$

$$d_2 = \frac{x - (\xi + L\sin\omega)}{\zeta + L\cos\omega} \tag{11}$$

By multiplying d_1 and d_2 by an arbitrary constant, we must multiply the x-y coordinate space to maintain the equity of Equations 10 and 11. Conversely, normalizing the x-y coordinate system to a constant value will normalize d, and hence, the displacement gradient to this value. We choose to normalize the x-y coordinate system to the fault length by multiplying the geometric parameter by $1/L$:

$$d_1 = \frac{(x/L) - (\xi/L)}{(\zeta/L)} \tag{12}$$

$$d_2 = \frac{(x/L) - ((\xi/L) + (\sin\omega))}{(\zeta/L) + (\cos\omega)} \tag{13}$$

We assume that the fault intersects the surface at $(0,0)$ and L is the down dip length from $(0,0)$ to the bottom of the fault. Faults that do not reach the surface can be represented by a number which is the fraction of the fault length that slips relative to the length of the fault if it were to reach the surface. We define n to be the portion of the plane that extends from the surface to the bottom of the fault along which slip does not take place. By doing this, we can express ξ and ζ as products of nL and the fault dip:

$$\xi = nL\sin\omega$$

$$\zeta = nL\cos\omega$$

This allows us to write d_1 and d_2 as a function of the fault dip, ω, the ratio of the surface location to the fault length, x/L, and the percentage of the fault which is inactive, n:

$$d_1 = \frac{(x/L) - n\sin\omega}{n\cos\omega} \tag{14}$$

$$d_2 = \frac{(x/L) - (n+1)\sin\omega}{(n+1)\cos\omega} \tag{15}$$

This normalization points out that the surface displacement gradient scales with the fault length.

Next, we normalize the transport-limited geomorphic transport model by assuming that the surface of the earth is flat prior to uplift and the total displacement along the fault is small compared to the fault. Considering our diffusive transport law in one dimension:

$$Q = -\kappa\frac{dz}{dx} \tag{16}$$

we see that, all other things equal, an increase in the horizontal dimension with the elevation remaining constant results in a decrease in the slope, and hence the flux of sediment moved along the profile. For an n-fold increase in the horizontal dimension, the flux will scale by $1/n$. Next, mass conservation states that:

$$\frac{\partial z}{\partial t} = \frac{\partial Q}{\partial x} \tag{17}$$

By similar arguments as those above, the change in elevation over time will scale with the inverse square of the horizontal dimension. Therefore, for a normalized uplift distribution, as the gradient in the uplift

distribution is reduced by expansion of the horizontal dimension, the change in the morphology of a one-dimensional diffusive profile will scale with the inverse square of the horizontal dimension ($1/x^2$).

We apply this argument to the displacement distribution resulting from movement along our model fault. It is important to note that changes in the horizontal displacement field over space result in slope changes. Therefore, where the gradient in the horizontal displacement field is large, the morphology may not simply scale with the horizontal length dimension. However, when the total amount of displacement along the fault is small compared to the length of the fault, the horizontal displacement gradient is also small. Under these circumstances, the morphologic development of the normalized scarp should be approximately related to the horizontal length scale. The one exception to this is where the fault daylights. At this point in space, the horizontal displacement gradient may be high, violating our generalized analysis. For this reason, we consider the case of thrust and normal fault of different dips separately in our analysis.

Previously, we showed that the surface displacement gradient scales with the fault length. Therefore, we can use the fault length, L, as our horizontal scaling factor in our normalized tectonic deformation and geomorphic transport model. Previous workers have shown that the morphology of a transport-limited, diffusive slope of fixed horizontal length scale is determined by the morphologic age, which is the product of the transport rate and time. We further modify this morphologic parameter, considering the length-scale dependence of the morphologic development of the scarp:

$$T = \frac{\kappa t}{L^2} \tag{18}$$

We call this parameter the dimensionless morphologic parameter, T. It describes the morphological development of scarps over space and time.

The last normalization we propose involves the normalization of the absolute elevation of the topographic surface to the fault slip rate of a continuously slipping fault. The magnitude of the surface displacement rates scale with the fault slip rate. This slip rate can be expressed as the total fault displacement, D, over a certain amount of time. We can rewrite the dimensionless morphologic parameter (T), solving for time:

$$t = \frac{TL^2}{\kappa} \tag{19}$$

The fault slip rate can be expressed as a function of the total fault displacement (D), the dimensionless morphologic parameter (T), the fault length (L), and the transport rate (κ):

$$\frac{D\kappa}{TL^2} = \text{ slip rate} \tag{20}$$

Because the surface displacements scale with the fault slip, we can rewrite the topographic elevation (H) divided by the fault slip rate:

$$\frac{HTL^2}{D\kappa}$$

These operations allow us to generalize our understanding of fault scarp development to dimensionless time and space. Using these normalizations, we can plot the location along the topographic profile normalized to the fault length (x/L) on the horizontal axis, the elevation scaled to the fault slip rate ($HTL^2/D\kappa$) on the vertical axis, with the development in time represented by the dimensionless morphologic parameter ($\kappa t/L^2$). In the next section, we present the morphologic development of transport-limited scarps for a variety of fault dip angles and senses of motion.

Unfortunately, production-limited scenarios require that transport processes may not be transporting material at full capacity. This complicates the normalization of production-limited scarp development in space and time. In this paper, we do not attempt to normalize the production-limited fault scarp problem, but rather explore their morphologic development for different length-scales and rates.

5.4 Diffusive Hillslope Development in Actively Uplifting Areas

We use our model of morphological scarp development along diffusive slopes to understand the behavior of these landforms, to what tectonic rates they are sensitive, and what geomorphic thresholds may cause abrupt changes in the morphology of the landscape. We first explore the deformation field resulting from tectonic displacements surrounding a fault. Typically, block motion of two fault blocks are used to simulate uplift resulting from movement along the faults. We contrast the deformation field from the block faulting model with our physically-based dislocation model. Then, we explore the morphology of transport-limited scarps for different sets of tectonic and geomorphic rates. Finally, we turn our attention to production-limited scarps to examine how these types of landforms develop and how they respond to different sets of tectonic and geomorphic rates.

5.4.1 Tectonic Uplift

Deformation around a fault may be complicated due to the influence of requirements of stress and strain continuity within the fault blocks, effects from the tips of the fault, how the deformation is thought to behave at the boundary of the area considered, and influences of lithology on the state of stress around the fault. Simple geometric models of deformation resulting from fault movement are often used; however, we opt for a more realistic characterization of the deformation by considering the mechanics of deformation around a

fault. In our model, we neglect the effects of lithology by assuming that the upper crust behaves as a linear elastic solid whose surface cannot sustain shear or normal tractions. We postulate that displacements within the medium die out at an infinite distance from the fault, and that the fault is finite and contained within the elastic medium. Making these assumptions, we can use the ideas developed in the previous section to calculate the stresses, strains, and displacement in the medium surrounding the fault

In order to understand the surface displacements resulting from constant slip along faults we plot the magnitude of the horizontal and vertical displacements for a fault undergoing unit slip. In this figure, the horizontal dimension is normalized to the total fault length, while the displacements are normalized to a unit slip on the fault. Figure 19a shows the case of a fault that reaches the surface ($n = 0$). Figures 19b–e show faults in which there is a variable sized no-slip patch at the surface. The magnitude and direction of the horizontal (top panels) and vertical (bottom panels) scales with the slip vector on the fault plane. Each of these plots was created for a fault dipping to the right at an angle, β, and experience positive slip (in this model construction, positive slip vectors represent reverse motion along the fault). In order to derive the displacement field due to normal motion along the fault, the magnitudes of the horizontal and vertical components of the surface displacements must be multiplied by -1. It is also important to note that because of our model parameterization, the horizontal location of the upper tip of the buried fault is not at $x = 0$. Instead, $(0, 0)$ is the location where the projected fault plane intersects the surface. Therefore, with larger values of n, the location of the upper edge of the fault tip moves to the right in the diagrams.

Several salient observations can be made from Figure 19. First, as the length of the slip patch decreases as it is buried (n becomes large), the magnitude of the surface displacements decrease. We see this by contrasting the magnitudes of the horizontal and vertical displacements shown in Figures 19a and 19e. In addition, our normalization showed that the displacement gradient, and hence the localization of the strain, scales with the fault length. This is consistent with the observation in Figure 19 in which the shorter, buried slip patches localize the deformation into smaller zones than longer slip patches. Another important observation is that motion along the fault produces both absolute changes in the foot wall and hanging wall shape near the fault [Densmore, et al., 1998]. In the case of a thrust fault, the foot wall subsides slightly, while normal fault foot walls may be slightly uplifted from movement along the fault. In addition, depending on the dip of the fault, there may be a reverse in vertical displacement magnitude within the hanging wall of the fault. For instance, the hanging wall of a low angle thrust will subside due to slip along the fault at a distance of approximately one fault length along the surface. Conversely, if the fault is the only plane along which discontinuous slip may occur, uplift must result in the hanging wall of a low angle normal fault in order to preserve the requirements of stress and strain continuity within the crust at all points but the dislocation. In the case that the fault plane does not reach the surface, the surface displacements can be complicated

(Figure 19).

From these diagrams, we see that the surface displacements may not be well approximated by block motion. Only in the case that the fault reaches the surface and the fault length is long relative to our window of observation at the fault scarp does the block faulting model result in good predictions of tectonic deformation. In order to understand where the block faulting model well-approximates the displacement field, we quantify the difference between the rigid block displacements and the physically derived displacements in Figure 20. In this figure, the vertical axis of each figure shows the ratio of the displacements derived from dislocation theory to those derived geometrically minus one. Therefore, a value of zero indicates perfect correspondence of the two approaches, whereas non-zero values show deviations in the two methods. In this figure, we fix the coordinate system of the block fault displacement field such that the error for a fault that reaches the surface will be zero at the fault trace. Clearly, the rigid block displacements poorly approximate the displacement field calculated from dislocation theory in all areas but those where the fault daylights. Displacements more than 30% of the fault length away from the fault accrue significant error with continued displacement. Also, in almost all cases, large errors are incurred as the tip of the fault does not reach the surface (Figure 20d–e). These figures emphasize that displacements calculated from a purely kinematic standpoint are not physically reasonable; therefore, we use the displacements determined from dislocations to approximate the surface displacement distribution in our models.

The threshold between different geomorphic processes may be driven by the rate at which relief is created by the interaction of geomorphic processes and tectonic rates. Therefore, different uplift rates may result in different regimes of geomorphic processes. For example, if production-limited conditions are favored by higher uplift rates, we expect the landforms to be dominated by production limited conditions near the fault (where uplift rates are highest) whereas transport-limited conditions will dominate far into the hanging wall(where uplift rates decrease).

5.4.2 Morphologic Development of Transport-Limited Scarps

We previously normalized the equations representing the transport-limited coupled tectonic and geomorphic transport processes. In this section, we present the results of our analysis for these types of scarps. In all of these models, we simulate a fault that dips to the right at a dip angle, β. For simplicity, we only consider faults that reach the surface ($n = 0$), although similar calculations can be performed for blind faults. On the horizontal axis of the plots, we show the position along the profile normalized to the fault length. The vertical axis is the topographic elevation adjusted for the slip rate ($HTL^2/D\kappa$), which we derived in the previous section. Finally, each panel shows a different stage in development as defined by the dimensionless morphologic parameter, T. Assuming that the total fault slip is low compared to the fault length, these

diagrams approximate the development of all transport limited scarps that form along an initially flat surface. Because the horizontal gradients are high at the fault tip, we consider thrust and normal faults separately in our calculations.

Figure 21 shows the development of thrust faults over space and time. We calculate the elevation at each point along the scarp from -150% to +150% of the fault length. For a mean transport rate (κ) of $4 \times 10^{-3} m^2/yr$ and a fault length of 1 km, the model simulation time is 400 kyr, each frame representing 50 kyr of model time. Conversely, the model simulation time is 10 Myr for a mean transport rate of $4 \times 10^{-3} m^2/yr$ and a 5 km long fault. In these models, the model space is extended to each side such that the displacements at the boundary due to slip along the fault are effectively zero. Finally, we fix the elevation at the zero displacement boundaries.

Several interesting observations can be made from this figure. First, tectonic subsidence in the foot wall at the fault may be created and preserved when fault dips are high. As the fault dip is reduced, it becomes less likely to preserve the basin ahead of the scarp, as deposition in front of the scarp overwhelms tectonic subsidence. Also, thrust faults with low dips may have negative topography in the hanging wall of the fault. Depending on the fault length, this effect may be subtle, as the subsidence may be gradual and distributed over many kilometers. Also, this figure points out that faster fault slip rates, roughly corresponding to larger values of the D/T term along the vertical axis, lead to larger values of elevation ($H = D\kappa/TL^2$) than do slower slip rates.

Based on these models, we see that the fastest change in the topographic surface occurs until about $T = 12 \times 10^{-4}$. For a 1 kilometer long fault where material is transported at a rate of $0.004\ m^2/yr$, it takes 300 kyr for this diffusive landscape to reach steady-state. After that time, the geomorphic transport of material away from the scarp balances the amount of material uplifted by tectonic processes, resulting in a "steady-state" condition in which the topography remains invariant with time. The absolute magnitude of the topography at this steady state depends on the fault slip rate, the transport rate, and the length of the fault. For a fixed fault length and transport constant, larger values of T represent larger amounts of time. As topography approaches steady state, little relief is created by faulting (see Figure 21, last two panels). Since the total displacement along the fault (D on the vertical axis of the diagrams) offsets the increase in T, the topography does not increase. It is also important to note that at steady state, the absolute magnitude of the topography increases with the fault length, all else being equal. As the dimensionless morphologic parameter becomes greater than about $T = 12 \times 10^{-4}$, the magnitude of the normalized elevation, $HTL^2/D\kappa$ does not change significantly. Because increases in T are balanced by increases in the total fault displacement, the $T/D\kappa$ portion of the normalized elevation remains constant. Therefore, the absolute elevation at steady state scales with the square of the fault length. Simply, longer faults build larger scarps.

In addition to the fault slip rate and length, the transport constant also plays a role in the absolute elevation of the steady state scarp. For a fixed fault length, as the scarp morphology approaches steady state, the TL^2/D term on the vertical axis remains constant. Comparing identical scenarios for two different transport constants, we see that as the transport constant decreases, the steady state scarp elevation increases to allow the material introduced tectonically to be redistributed off of the scarp. Therefore, the absolute scarp elevation at steady state is inversely proportional to the transport constant. In other words, geomorphic systems which have more transport capacity available are more efficient at transporting material that is introduced by tectonic deformation and need not build steep slopes to remove this material.

It is also worth mentioning that the absolute time to steady state is strongly dependent on the fault length and is independent on the fault slip rate in diffusive landscapes. This is because longer faults produce lower displacement gradients, which result in lower hillslope gradients and slower transport. As the fault length increases, the time it takes for the landscape to reach steady state increases as the square of the fault length. For short faults (e.g., 100 meters), steady state may be reached as soon as 400 years, if the transport rates are high ($\kappa = 0.04 m^2/yr$). However, long faults and low transport rates (e.g., $L = 10$ km, $\kappa = 0.0004 m^2/yr$) can take hundreds of millions of years to reach steady state. Also, the time it takes to reach steady state is dependent on the fault dip. Lower fault dips result in lower magnitudes of uplift. These faults will develop steady state topography sooner than their steeper counterparts. While faster slip rates may build higher steady state topography, the time it takes for the landscape to attain equilibrium for similar fault lengths and transport rates is the same, regardless of fault slip rate.

We resolve the detail of the scarp's morphologic development where the fault reaches the surface in Figure 22. The scarp face is the most prominent expression of the tectonic activity, as this is the area of the highest offsets and offset gradients around the fault. Some workers have used the morphology of the fault scarp in order to date fault slip events and determine fault slip rates. These types of studies typically examine the surface only within 15%–0.5% of the fault length; therefore, the scale of paleoseismic morphologic observations corresponds more to Figure 22 than to Figure 21. We refer to the profile length range of -15% to +15% of the fault length as the near field morphologic development of the scarp.

We see in Figure 22 that the scarp height over time is a function of fault slip rate, the transport constant, and the fault dip. Shallowly dipping faults have more subtle geomorphic expressions than do steeply dipping reverse faults. Also, it is important to note that the heterogeneous deformation field created by slip along the fault causes the surface profile not to pivot around the slope center point as they do in simple, uniform offset models. In fact, high angle reverse faults can create sufficient relief to accelerate erosion in the hanging wall such that erosion actually bevels the top edge of the block significantly (see Figure 22, last panel).

Where the fault dip and length and the geomorphic transport rate can be estimated, profiles such as those

in Figure 22 may be used to infer the fault's slip rate and estimate the timing of initiation of movement along the fault. However, from the above observations, it is clear that as steady state is approached, the topography becomes less sensitive to the time since the beginning of movement along the fault. In the next section, we evaluate how our inferences about the tectonic activity on the fault may become more poorly resolved with increasing total slip along the fault.

We repeat the modeling of transported limited scarps for faults experiencing normal motion. The far field geomorphic development of these scarps is shown in Figure 23 and the near field geomorphic development is shown in Figure 24. The far field morphologic development of normal faults looks much like the case of thrust faults, with the exception that the uplift distribution has been reversed. However, several important differences exist between the near field development of thrust faults and normal faults. First, the diverging horizontal displacements along the fault plane act to smear the topography out over wider zones than thrust faults, which shorten the topography. The topography of low angle normal faults is minimal in these situations, as sufficient transport capacity is available to transport most of the tectonically deformed sediment across the fault. Even steep normal faults have subtler expressions than do their thrust counterparts. This effect arises because thrust faults localize the deformation of the topography at the location that the fault daylights, whereas the normal counterpart not only displaces the topography vertically, but extends it as well, resulting in lower slopes than thrust faults.

As with thrust faults, normal faults reach the same steady state topography condition as time increases. They are likely to reach this condition at about the same point in time; however, the lower slopes created by extension adjacent to the fault plane cause the normal faults to reach steady state slightly sooner than thrust faults.

5.4.3 Morphologic Development of Production-Limited Scarps

Production-limited scarps require that we allow the geomorphic transport process to operate at less than full capacity. This restriction prevents us from generalizing our understanding of the morphological development of these types of scarps by normalizing the scarp features to the controlling rates, as we did with transport-limited scarps. In order to gain intuition as to how production-limited scarp morphology is effected by tectonic and geomorphic rates, we fix all process rates but one to isolate the effect of a single process on the geomorphic development of the scarp.

In each of the models below, we model a 45 degree dipping normal fault that is 10 km long. Except where noted, we assume that a uniform initial regolith thickness of 40 cm is present. We change the fault slip rate, the bedrock surface production rate (B_a), the production thickness sensitivity (B_b), and the geomorphic transport rate (κ) in order to determine each's effect on the morphology of the scarp. The values of the fixed

parameters are estimated mean values, except where noted. The extreme values of the variable parameter are used to capture the range of behavior induced by each factor. In each of the diagrams in Figures 25–28, the upper solid line is the surface topography, the dashed lower line is the location of the regolith/bedrock interface, and the gray shaded areas are bedrock. Also, there is significant vertical exaggeration in the diagrams. We examine only the near field (-20 m– +20 m) morphologic development of the scarp, because this is the place where the vertical displacement gradient is greatest and hence, the location where bedrock will likely be exposed first.

We first examine the effect of fault slip rate on the morphologic development of production-limited scarps. In this set of models, we use an estimated mean values for $B_a = 80$ m/Myr, $B_b = 0.02$ cm^{-1}, and $\kappa = 4 \times 10^{-3}$ m^2/yr. The upper three panels of Figure 25 show the development over time of a fault that creates 0.1 mm/yr of uplift at the fault scarp, while the lower panels show the development of a fault that creates 1 mm/yr of uplift. Each column represents an equal amount of throw along the fault; therefore, the time increment between each panel in the top and bottom models is not the same. In the case of low slip rates, production rates are able to keep up with the creation of relief at most points in the landscape. The one exception to this is the point at which the scarp daylights, where a small patch of production limited material is exposed. The topographic expression of a slowly slipping fault where the bedrock is converted to regolith at moderate rates is much like that of a transport-limited scarp, and may require excavation along the profile to reveal the regolith/bedrock interface. In contrast, a fault that produces uplift much faster than the bedrock surface production rate quickly becomes production-limited. A bedrock cliff forms at the fault scarp, isolating the material on the top of the scarp from the colluvial pile on the bottom. This isolation allows the slopes to steepen at the scarp face without acceleration of the sediment flux at the top of the scarp. The colluvial pile is effectively independent of transport at the top end of the scarp and grows only as material is produced from the scarp face and travels downslope. In the case of transport-limited scarps, the steepening of slopes accelerates the sediment flux where the slopes steepen, creating a negative feedback for the development of relief. However, the introduction of production-limited conditions removes this feedback, as the creation of relief separates the transport-limited portions of the hill slopes at the top and bottom of the scarp.

In the second set of models, we explored the effect of the surface bedrock production rate on the morphologic development of the scarp (Figure 26). In these models, the fault slip rate was fixed to produce 1 mm/yr of uplift at the scarp and the production thickness sensitivity and transport rate were set to estimated mean values ($B_b = 0.02$ cm^{-1} and $\kappa = 4 \times 10^{-3}$ m^2/yr, respectively). The top three panels in Figure 26 show the effect of a low production rate, while the lower panels show the effect of a high production rate. In the case of low production rates, the scarp quickly becomes production-limited, while high production rates prolong transport-limited conditions. In addition, high surface production rates produce thicker regolith at the top

and bottom of the scarp and allow more convex morphologies to persist. Early in the development of scarps with production rates comparable to uplift rates, the convexity of the hillslope in the transport-limited scarp is reflected at the regolith/bedrock interface. Continued movement along the fault exposes bedrock and creates production-limited conditions; however, the initial convexity of the regolith/bedrock interface that was created when the scarp was transport-limited is preserved. This allows a beveled edge to develop above the scarp face.

Also, it is important to note the importance of the timing of the onset of production-limited conditions on the size and shape of the colluvial pile at the base of the scarp. Either initially thick sequences of transportable material or high surface production rates allow transport-limited conditions to persist for significant amounts of time. The longer transport-limited conditions can be maintained, the more material can be transported from the top of the scarp to the bottom, for as the scarp becomes production-limited, the top of the scarp is isolated from the colluvial pile. Because even the largest bedrock production rates produce only moderate amounts of transportable material over time, large colluvial piles at the base of the scarp can only result from scarps that have been active for exceedingly long amounts of time or are relics of former transport-limited conditions.

Next, we investigate the effect of the production thickness sensitivity on the morphology of the scarp in Figure 27. The top set of panels shows the case of a production rate that decays gradually with depth, whereas the bottom panels show the case of a production rate that decays rapidly with depth. In these models, the fault slips such that 0.1 mm/yr of uplift is created by movement along the fault, the surface production rates are moderate, and the transport rates are approximately the estimated average production rate. We see that under these conditions, the scarp morphology is relatively insensitive to the thickness sensitivity. There is a subtle preservation of regolith along the upper portion of the scarp in which the production thickness sensitivity is low. However, the effect on the observed topography is negligible, and excavation of the foot wall would be required to resolve the difference between the two cases.

The transport rate, κ, controls the morphology of those parts of the scarp that are production-limited. In Figure 28, we contrast the scarp morphology resulting from two different transport rates. The slip rate and bedrock production rate are chosen to quickly expose bedrock along the slope of the scarp. The upper three panels show the case of a low transport rate ($\kappa = 4 \times 10^{-3}$ m^2/yr), while the lower three panels show the case of a high transport rate ($\kappa = 4 \times 10^{-2}$ m^2/yr). There are three important differences between these cases. First, production-limited scarps in which material is being transported quickly expose more of the scarp face than do scarps with low transport rates. The exposure of more of the bedrock cliff may accelerate bedrock production in cases where the bedrock production rate is sensitive to small changes in the thickness of the overlying regolith cover. Secondly, the low transport rate scarps have a smoothly varying concave

up morphology along the tailus pile, whereas high transport rate scarps have a nearly linear morphology along the tailus pile. Finally, the regolith mantle in the foot wall of the fault and adjacent to the scarp is mostly preserved with low transport rates. In contrast, high transport rates allow the stripping of the regolith cover well into the foot wall of the fault, resulting in a thin mantle or production-limited conditions on the up-thrown block of the fault.

In contrast to transport-limited scarps, there is a profound distinction between normal and reverse motion when considering production-limited scarps. In the case of transport-limited scarps, the horizontal component of displacement acts to incrementally reduce slopes away from the scarp, whereas shortening acts to steepen slopes adjacent to the scarp. These differences create visible differences in the morphologic development of these types of scarps; however, their gross morphologies are similar. In the case of production-limited scarps, these differences are accentuated by the displacement of bedrock at depth. Normal motion along faults acts to move adjacent points in the bedrock away from one another in the horizontal direction as the fault is crossed. However, reverse faulting acts to decrease, and even overlap this distance in the horizontal direction. In all of the above examples, the bedrock is passively exhumed by the geomorphic relaxation of the scarp slope. In contrast, reverse faults are actively exhumed as they intersect the surface and juxtapose bedrock directly with transportable material.

As an example of this behavior, we consider the case of a normal fault with high transport and production rates and a thrust fault undergoing similar geomorphic conditions. If the fault slip rate and surface production rates are similar and the transport rates are moderate, the normal fault scarp may never reach a production-limited condition because the slope of the scarp is buried at the rate that tectonic displacements accrue as motion along the fault is roughly parallel to the mid-slope and transport direction of material downslope. However, a reverse fault slipping under these conditions will likely expose bedrock because motion along the fault acts to increase slopes and accelerate geomorphic transport, and motion along the reverse fault pushes the bedrock in a direction perpendicular to the mid-slope of the scarp and the direction of downslope material transport. In cases where a normal fault is slipping quickly compared to the surface production rate, the scarp face is exhumed by geomorphic transport. Under these circumstances, the hanging wall of the thrust fault will be exhumed by geomorphic processes as it penetrates the mid-slope as the slip along the fault outruns the conversion of bedrock material in the hanging wall into transportable material.

We demonstrate this difference in Figure 29. The top set of panels show a 45 degree dipping thrust fault slipping such that 1 mm/yr of uplift is created at the scarp, and the lower set shows the same fault creating 0.1 mm/yr of uplift at the scarp. In the case of the slowly slipping fault, bedrock quickly reaches the topographic surface and starts to be converted to transportable material at a rate that keeps up with the slip on the fault. With time, a production-limited band exists in the hanging wall of the fault where the bedrock is juxtaposed

with the regolith mantle. In contrast, a quickly slipping fault displaces the wedge of bedrock toward the surface much faster than production processes can transport the material away from the scarp. Therefore, an overhang forms that isolates the material transport in the hanging wall from that of the foot wall.

These simple model demonstrates an obvious, but profound difference in the way that production-limited normal fault scarps behave as compared to reverse fault scarps. The overhang of material created by faulting must quickly result in the mechanical failure of the bedrock by processes not considered in our simple analysis. These bedrock landslides will tend to relax the slope of the outcropping bedrock perpendicular to the direction of transport. This results in the shedding of a large apron of material in front of the fault scarp. In any case, reverse faults must always create a mechanically unstable overhang as long as slip rates are high compared to surface bedrock production rates. In contrast, if a normal fault dips at an angle less than the stable slope angle of the bedrock, mechanical failure is unlikely. Where normal faults dip steeply enough to warrant mechanical failure of the bedrock, small amounts of tailus material act to buffer the slopes from further failure. Movement along reverse faults causes the hanging wall of the fault to ride over the tailus pile, requiring large amounts of material created by mechanical failure to buffer the slope created by fault motion. Previous models [e.g., Arrowsmith, et al.,, 1996] have not shown this effect because the bedrock profile is interpolated at every time step to a regular gridded interval. This regridding effectively erodes the bedrock, preventing subsurface bedrock slopes from exceeding vertical slopes.

It is worth emphasizing that most production-limited thrust faults are not treated well with the modeled processes. Bedrock overhangs at the front of the scarp require processes such as mechanical failure of bedrock slopes in order to prevent the physically unreasonable case of large bedrock overhangs from occurring.

5.5 Morphologic Dating of Scarps

Many workers have used the morphology of scarps to constrain the timing and rates of movement along a fault. This method is based on the idea the landscape responds to slip along a fault in a consistent, predictable way. By calibrating the transport rate, we can infer tectonic parameters such as the time at which movement along the fault ceased based on the topographic expression of the fault scarp.

The dating of inactive faults and the estimation of rates along active faults using the scarp morphology requires the calibration of the transport constant, κ, the surface bedrock production rate, B_a, and the production thickness sensitivity, B_b. The calibration of the bedrock production parameters (B_a and B_b) need not be conducted along scarps with thick regolith. Studies of transport-limited scarps have successfully inferred rates and timing of movement along a fault where geomorphic rates can be constrained.

Because the landscape is the product of both tectonic displacements and geomorphic transport, the infor-

mation contained within the topography about one of these sets of processes is lost as it is overwhelmed by the other. For example, in areas where geomorphic transport rates are high relative to tectonic displacement rates, the landscape provides little information about the tectonic processes, as the tectonic expression of the fault is subtle. We explore the landscape sensitivity to different fault slip rates and geometries to determine how much information about these parameters is determined in the landscape. We consider the inferences of rates and timing based on the morphology of production-limited scarps.

We quantify our ability to resolve tectonic rates from the topographic resolution of the scarp by comparing the topographic profiles of a fault that slipped in a single event a constant amount of time ago with one that slipped in a single event a slightly different amount of time in the past (Figure 30). In the case depicted in Figure 30a–c, a 45 degree dipping normal fault is instantaneously offset 20 meters. Following offset, the fault degrades. Initially, the steep slopes result in rapid transport of material downslope. As time passes, the rate at which material moves downslope decreases, slowing the morphologic development of the scarp. Therefore, as the scarp becomes older and the transport of material downslope slows, it becomes more and more difficult for us to determine the age of the scarp. In Figure 30a–c, the solid line denotes the theoretical topographic profile at the time defined by $\kappa t/L^2$ and the dashed lines represent the topographic profile if the scarp were 100 $\kappa t/L^2$ younger or older than the true age of the scarp. As the scarp becomes "older", the ± 100 $\kappa t/L^2$ profiles become indistinguishable from the actual topographic profile. Therefore, as the scarp becomes older, we loose our ability to resolve these differences in the scarp age based on only morphology.

We plot the root mean square error (RMS error) between the profile at times $\kappa t/L^2$ (called the control profile) and a profile whose age is denoted on the horizontal axis of Figure 30d (called the perturbation profile). As the perturbation profile approaches the control profile, the RMS error decreases, and is zero when the perturbation profile is equal to the control profile. Where the RMS error increases rapidly around the age of the control profile, small differences in age result in large differences in scarp morphology. Therefore, these situations yield ages that are well defined by topography. Conversely, where the RMS error increases slowly as the age of the perturbation profile deviates from the control profile, the age of the scarp is ill-defined by the topography. We can quantify this difference by prescribing a maximum tolerance in the RMS error to see what the difference in the calculated ages will be. In Figure 30d, the dashed horizontal line shows this RMS tolerance. The abscissa at which this tolerance intersects the RMS curve for each measurement defines the age error for the RMS tolerance. We see that as the scarp gets older, a fixed RMS tolerance produces scarps whose age error increases with time. The choice of the RMS tolerance is arbitrary; therefore, this analysis allows us to estimate the resolution loss relative to scarps of different ages.

Similar analyses can be applied to a continuously slipping fault. In this case, the resolution of the fault slip rate and timing of initiation of movement along the fault are evaluated instead of just the age of the fault. Below,

we perform this analysis on transport- and production-limited fault scarps to understand the loss of resolution of fault slip rates and timing of movement along faults with time. While these calculations are designed for determining the information loss over time for the purpose of understanding morphologic scarp dating, the loss of information over time reflects the influence of one set of processes (either tectonic or geomorphic) processes dominating the system over time. Therefore, the results of these sensitivity analyses can also be used to understand under what conditions diffusive landscapes are dominated by tectonic processes, geomorphic processes, or some combination of both.

5.5.1 Previous Work on Morphologic Scarp Dating

The determination of recent faulting activity typically requires studies in which young strata, datable by methods such as ^{14}C age dating, can be identified and causatively linked with activity along a particular fault. These types of studies provide a record of the timing of individual events and the offset magnitude in areas where the slip vector and piercing points of known age exist. However, depositional hiatuses and distributed deformation may skew the results of these studies such that apparently low slip rates and "slip gaps" in time may solely be the product of the sampling bias caused by depositional and structural complexities. In order to understand the longer temporal and broader spatial scale behavior of an active fault, the morphology of a fault scarp may be used to infer tectonic rates where geomorphic rates can be calibrated. Morphology studies sacrifice the resolution of individual events; however, they provide us with a means of glimpsing at the behavior of the fault over time scales ranging from 10s to 100s of thousands of years.

5.5.2 Resolution of Transport-Limited Scarps

We first consider the case of information loss along a single event scarp. We calculate the error induced in $\kappa t/L^2$ as a function of $\kappa t/L^2$ (Figure 31). The top panel shows the errors for an RMS tolerance of 0.01 m, regardless of the scarp height. Increasing errors correspond to a reduction in our ability to determine the timing of movement along the fault. We see in this figure that for a constant RMS tolerance, the error in $\kappa t/L^2$ increases with increasing $\kappa t/L^2$. Scarps with small amounts of displacement are more poorly resolved than are scarps with large amounts of displacement. This is likely because we fix the RMS tolerance for each of the scarp heights. In the second panel (b), we scale the RMS tolerance to be 10% of the total displacement along the fault. By doing this, we attempt to remove the effects of total displacement on the scarp resolution. We see that by doing this, the loss of resolution over time is similar for each value of the total scarp displacement (Figure 31). However, it is clear that the loss of resolution is not simply related linearly to the total fault displacement. In general, when we normalize the RMS tolerance to the total fault displacement, the faults with larger displacement are more poorly resolved over time.

5.6 The Transition From Transport-Limited to Production-Limited Conditions and Steady-State Landforms in Actively Uplifting Areas

In the transport-limited analysis, we saw that the landscape eventually reaches a state of equilibrium in which geomorphic processes exactly remove all of the tectonically introduced material around the source of deformation. We call this condition the steady-state landscape condition. The time it takes for this condition to be reached is dependent on the fault length and the transport constant. In the case of linear diffusion, steepening of slopes by tectonic deformation leads to higher material transport downslope. The amount of material moved downslope increases until all of the material is removed from areas where relief is being created to areas where little or negative relief exists.

This steady-state condition is only possible when an infinite thickness of transportable regolith exists. In the general case of production-limited scarps, a steady-state exists when not only the topography does not vary with time, but the regolith/bedrock interface remains fixed. As we saw in the previous sections, when the uplift rate resulting from slip along a fault is much higher than the bedrock production rate, bedrock is exposed. Once the production-limited threshold is crossed, the isolation of the diffusive transport system at the bottom of the scarp from the top removes the feedback which causes slope steepening to result in higher downslope material transport. Therefore, the negative feedback existing between geomorphic processes and tectonic deformation is removed. Unless other bedrock production processes, such as bedrock landsliding, are invoked the exposure of bedrock prohibits the existence of a steady-state landscape.

In the next section, we explore the conditions necessary for a steady-state landscape to exist when the presence of bedrock and the production of regolith is considered. In summary, we find that for the geomorphic processes modeled, three domains exist. In the case that bedrock surface production rates are on the order of, or larger than tectonic uplift rates, the location of the surface and bedrock/regolith interface may remain invariant with time. In the case that tectonic uplift rates are much higher than bedrock production rates, bedrock will eventually be exposed, and the landscape cannot attain a steady-state condition. However, the presence of large, preexisting basins of transportable regolith may act to prolong the exposure of bedrock. In this case, a "quasi" steady-state condition exists where the topographic surface may be in steady-state; however, low production rates continually move the bedrock closer to the surface. If the period of tectonic activity is less than the amount of time required to strip the preexisting regolith, the system is effectively in steady-state.

In order to capture the diffusive response of a steady-state landscape, we consider two scenarios. In the first, we assume that the fluvial systems in the hanging wall of a reverse fault, or conversely the foot wall of a normal fault, grade to the level of the deformation over short time-scales relative to the diffusive response.

These hill slopes are effectively controlled by a dropping baselevel that down-cuts at the rate of relative uplift across the fault. In these scenarios, we calculate the requirements for a steady-state diffusive landscape to develop, and the time required to reach this state. In the second scenario, we consider the diffusive response of the landscape at the range front scarp. For this scenario, we calculate the requirements for and time to steady-state using the models developed previously in this paper.

5.6.1 Rates Required for Steady-State Conditions

We start with a landscape in which material is transported downslope by diffusive transport processes towards a channel that down-cuts at the rate of uplift at the fault. In this system, we assume that there is enough stream power in the channel to transport any material delivered to the channel by diffusive processes. At steady-state, each point along this type of hillslope will drop in elevation at the rate that the channel incises [ref]. In order to preserve transport-limited conditions along the slopes, the bedrock surface production rate must be equal to or exceed the rate at which the baselevel drops. Where the surface production rate exactly equals the baselevel incision rate, the surface of the slope will be mantled by an infinitely thin regolith. When the surface production rate exceeds the baselevel incision rate, regolith will mantle the slopes. The thickness of the regolith mantle will be determined by the production rate thickness sensitivity.

We can calculate the conditions under which steady-state can exist and the thickness of the regolith mantle by realizing that the unchanging bedrock/regolith interface relative to the surface topography will occur when the bedrock production rate is equal to the baselevel incision rate, V_z:

$$V_z = B_a e^{-B_b T}$$

This equation can be rearranged to solve for the steady-state regolith thickness, T:

$$B_b T = -\ln \frac{V_z}{B_a} \tag{21}$$

Figure 32 shows the steady-state regolith thickness for different sets of baselevel incision and bedrock surface production rates. The gray area shows the zone in which a steady-state condition is possible. The vertical axis plots the steady-state regolith thickness scaled to the thickness sensitivity. The domain of the graph encompasses the realm of reasonable baselevel incision rates and bedrock surface production rates. It is important to note that the domain in which steady-state diffusive landscapes undergoing steady regolith production exists is extremely limited as compared to the possible range of tectonic and bedrock production rates. For production rates an order of magnitude higher than those measured in Northern California [800 m/Myr; Heimsath et al., 1998], the diffusive landscape cannot remain in steady-state for even low (0.8 mm/yr)

uplift rates. Therefore, in tectonically active areas in which deformation is localized and the regional baselevel in the uplifted block down-cuts at the rate of tectonic uplift, diffusive landforms are likely a transient feature whose eventual destiny is to be obliterated by the exposure of bedrock.

The heterogeneous deformation field around faults results in a heterogeneous uplift distribution in the hanging wall of the block (see Figure 19). When the fluvial system incises at the rate of the uplift in the hanging wall, the uplift rate decreases as one moves away from the location where the fault daylights. These decreasing uplift rates into the hanging wall may preserve transport-limited conditions in parts of the hanging wall, whereas near the fault, the landscape is driven into production-limited conditions. In the case that the fault slip rates are low enough to preserve transport-limited conditions everywhere in the landscape, the steady-state regolith thickness will vary throughout the landscape according to the magnitude of the tectonic uplift rate at that point.

Figure 33 shows the steady-state regolith thickness in the hanging wall of a reverse fault in which the fluvial system incises at the uplift rate within the hanging wall. Each of the panels (a)–(e) shows different fault geometries. Because the uplift rate decreases as one moves away from the hanging wall, the steady-state regolith thickness increases. In the case of a reverse fault dipping less than 45 degrees, subsidence in the hanging wall caused by movement along the fault results in the continual deposition of material into this basin. Within the areas of subsidence, the regolith thickness continually increases as the basin is filled with material being shed from the portion of the hanging wall adjacent to the fault. For fault dips greater than 45 degrees, there is no subsidence in the reverse fault hanging wall, hence, there is a finite steady-state regolith thickness for these cases.

5.6.2 Time to production-limited conditions

In cases where the baselevel incision rate is greater than the bedrock production rate, a true steady-state diffusive landscape cannot exist. However, topographic steady-state may be achieved if there is sufficient preexisting regolith to prevent bedrock from being exposed. In this case, bedrock may be approaching the surface while the topography is in steady-state. The length of time that this topographic steady-state can persist depends on the amount of preexisting regolith, the bedrock surface production rate, the depth sensitivity of the bedrock production rate, and the incision rate of the fluvial system.

In Figure 34, we compute the amount of time it takes to expose bedrock, given that the incision rate is equal to the tectonic uplift rate. In each panel, the vertical axis shows the time required to expose bedrock for an initial regolith thickness shown on the horizontal axis. Different lines in each panel represent different incision rates. Finally, bedrock production parameters are varied between each panel. In each of the panels, the ratio of the bedrock surface production rate to the incision rate scales the initial soil thickness to the

time of bedrock exposure. In general, the bedrock thickness sensitivity is important only in cases where the bedrock production rate is close to the landscape incision rate. Under these conditions, low bedrock thickness sensitivities may prolong the exposure of bedrock slightly. It is interesting to note that if thick sequences of regolith exist prior to motion along a slow moving fault, it can take hundreds of millions of years for the bedrock to be exposed. Therefore, this topographic steady state condition in which the regolith/bedrock interface travels towards the surface may be regarded as being a steady-state landscape, given the typical duration of tectonic events as 10s of millions of years.

5.7 Discussions and Conclusions

Many people have built quantitative models that address the response of the landscape to climatic and tectonic forcing. These models include a plethora of geomorphic transport laws that route sediment through the landscape to produce topography. This paper addresses only one of the simplest geomorphic processes and a basic solution for confined faulting in an elastic medium. While our models to not include the complexity of these other models, we see that an examination of this simple transport law allows us to build much intuition as to how hill slopes may or may not respond to rock uplift. In addition, even in this elementary geomorphic system, a great variety of landscape behavior is produced, many traits of which mimic natural systems. This richness of information for a single geomorphic system highlights the advantage of systematically analyzing landscape response to uplift: while complex models can produce a wide variety of geomorphic behavior for reasonable geomorphic rates, single process, simple models can produce complex behavior as well. Because complexity exists within even the simplest geomorphic systems, a direct comparison of all topographic data with model results may produce a solution which may be fit with a great number of possible models.

We show that the transition from transport- to production- limited landforms produces a profound impact on the morphology of landforms in tectonically uplifting areas. When landforms are diffusive and transport-limted, the landscape may reach a steady-state condition where all of the material uplifted by tectonic processes is removed by geomorphic processes. Conversely, when the landscape becomes production-limited, diffusive processes may never produce a steady-state landscape, and thus the observed morphologies at any time represent a convolution of the fault slip history, the slip rate, the rate at which bedrock is converted to regolith, the geomorphic transport rate, and the topography that was present prior to the initiation of faulting. In this study, we seek a hueristic understanding of these landform morphologies by assuming simple initial conditions and constant geomorphic and tectonic rates over time, to see the effects of changing each is on the landscape over time. Our results show that even simple transport laws and tectonic deformation patterns produce complicated production-limited landscapes that are not directly interpretable in terms of

the tectonic and geomorphic rates that caused the landscape's morphology. If rates are to be interpreted from production-limited fault scarps and landscapes, we must independently reconstruct many of the rates and initial topography.

In this study, we also show that most landscapes undergoing even moderate uplift likely become production-limited with time. Therefore, in tectonically active areas, bedrock exposure is the rule, rather than the exception, to landscape development. The introduction of production-limited conditions introduces the complications cited above; therefore, further study of simple production-limited geomorphic systems is required before the coupled tectonic and geomorphic model may be used to estimate tectonic rates.

5.8 Acknowledgements

Speical thanks to Stephen Holloway for help with the production of certain aspects of this document and to Lee Amoroso for many important discussions about fault scarps. We also wish to acknowledge our esteemed collaborator, Roland Bürgmann for his inspiration in the execution of these analyses.

6 References

Arrowsmith, J R., Pollard, D. D., Rhodes, D. D., Hillslope development in areas of active tectonics, *Journal of Geophysical Research*, v. 101, p. 6255–6275, 1996.

Arrowsmith, J R., Rhodes, D. D., Pollard, D. D., Morphologic dating of scarps formed by repeated slip events along the San Andreas Fault, Carrizo Plain, California, *Journal of Geophysical Research*, v. 103, p. 10141–10160, 1998.

Bull, W. B., Pearthreee, P. A., Frequency and size of Quaternary surface ruptures of the Pitaycachi Fault, northeastern Sonora, Mexico, *Bulletin of the Seismological Society of America*, v. 78, p. 956–978, 1988.

Carson, M. A., and Kirkby, M. J., *Hillslope form and process*, Cambridge University Press: New York, 475 pp., 1972.

Densmore, A. L., Ellis, M. A., Anderson, R. S., Landsliding and the evolution of normal-fault-bounded mountains, *Journal of Geophysical Research*, v. 103, p. 15203–15219, 1998.

Du, Y., Segall, Gao, H., Dislocations in inhomogeneous media via a moduli-perturbation approach: general formulation and two-dimensional solutions, *Journal of Geophysical Research*, v. 99, p. 13767–13779.

Fernandes, N. F., Dietrich, W. W., Hillslope evolution by diffusive processes; the timescale for equilibrium adjustments, *Water Resources Research*, v. 33, p. 1307-1318, 1997.

Gilbert, G., K., *Report on the Geology of the Henry Mountains*, U. S. Geogr. and Geol. Surv. of the Rocky Mt. Reg., Washington D. C., 1880.

Heimsath, A. M., Dieterich, W. E., Nishiizumi, K., Finkel, R. C., The soil production function and landscape equilibrium, *Nature*, v. 388, p. 358-361-1997.

Machette, M., History of Quaternary offset and paleoseismicity along the La Jencia Fault, central Rio Grande Rift, New Mexico, *Bulletin of the Seismological Society of America*, v. 76, p. 259–272, 1986.

Mayer, L., Tectonic geomorphology of escarpments and mountain fronts, in *Active Tectonics*, Wallace, R. E., editor, Natl. Acad. Press. Washington, D.C., United States, p. 125–135, 1986.

McCalpin, J. P., editor, *Paleoseismology*, San Diego, Academic Press, 588 pp., 1996.

Schwartz, D. P., Hanks, T. C., Morphologic dating of the pre-1983 fault scarp on the Lost River Fault at Doublespring Pass Road, Custer County, Idaho, *Bulletin of the Seismological Society of America*, v. 77, p. 837–846, 1987.

Stewart, I. S., Hancock, P. L., Whati s a fault scarp? *Episodes*, v. 13, p. 256–263, 1990.

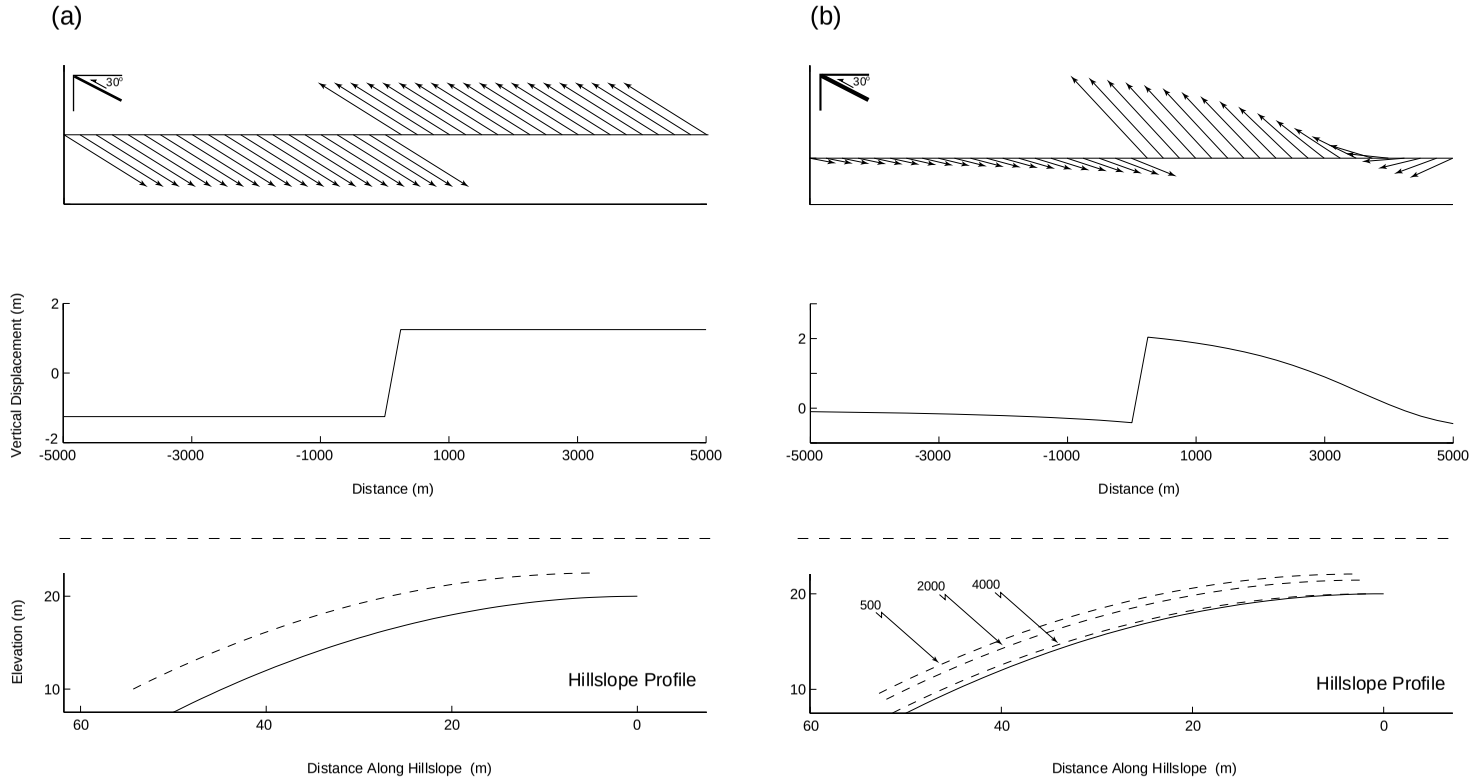

Figure 14: (a) Uplift field due to block faulting. (b) Displacement vectors resulting from slip and deformation on and around a fault. Notice that (a) approximates the uplift field when fault geometries are near vertical, deep and near planar, and the area of interest is adjacent to the fault. The first row of figures shows the displacement vectors in the case of block faulting or deformation due to slip along a dislocation in an elastic medium, whereas the second row shows only the vertical component of displacement in each case. The third row considers a 50 m long hillslope in the hanging wall of the thrust. The solid line is the topography of the hillslope prior to deformation due to faulting, whereas the dashed line in the left panel shows the final geometry of the hillslope after faulting. Because deformation in the block faulting model is homogeneous throughout the hanging wall, the hillslope undergoes a constant translation due to deformation. However, in the case of the fault in an elastic medium, the deformation of the hillslope at different distances from the fault (labeled dashed lines in right panel) show different degrees of deformation due to the inhomogeneous strain field created by movement along the dislocation. The fault in each case slips 5 meters and dips 30^0 to the right in the figure.

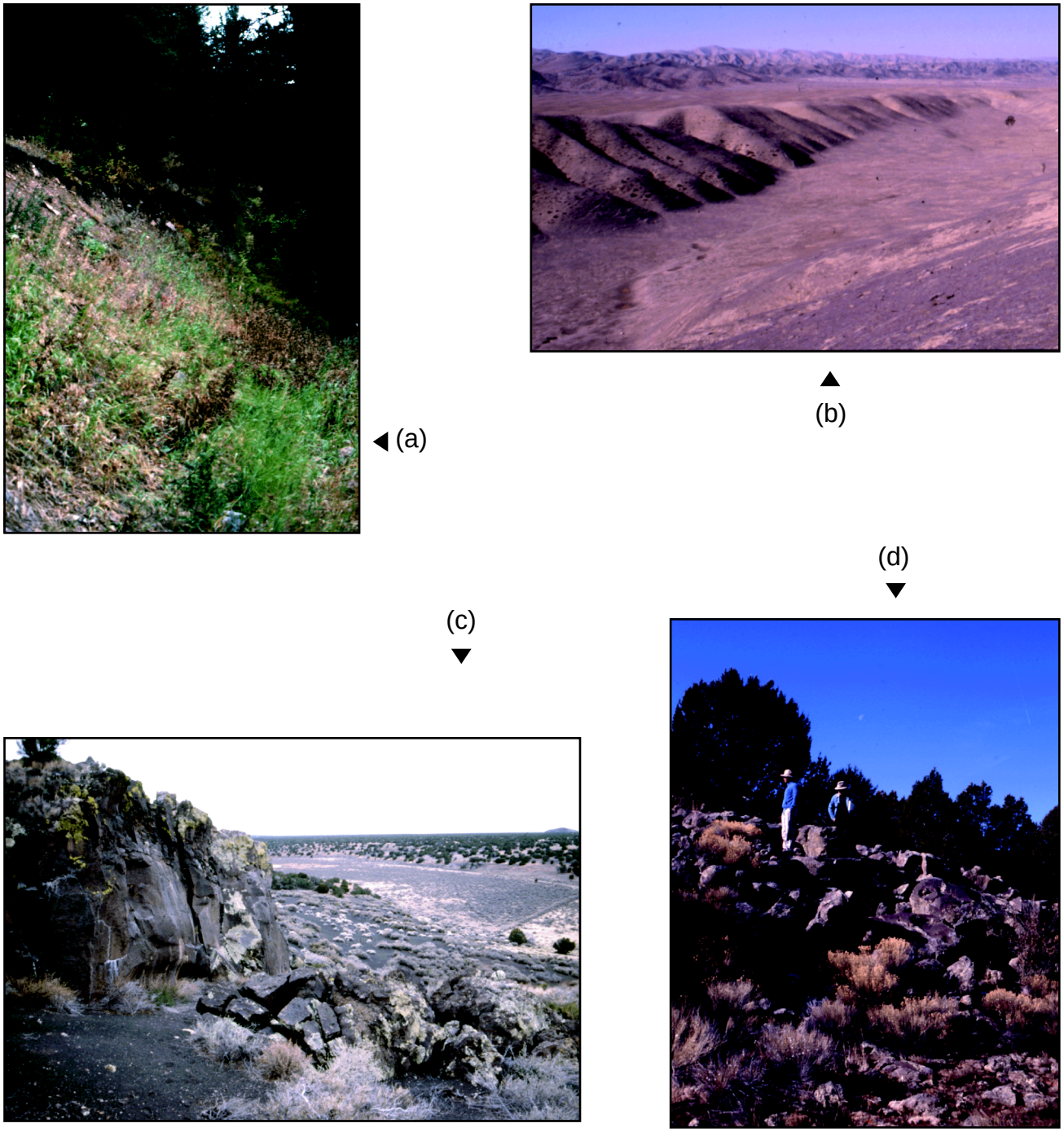

Figure 15: Degradation of transport-limited (a)–(b) and production-limited (c)–(d) scarps. Following rupture, transport-limited scarps form a steep linear profile whose angle is typically close to the angle of repose of the material (a). With time, the scarp degrades into a convex form on the upper slopes with a concave form on the lower slopes (b). In contrast, rupture along production-limited faults expose bedrock, creating a bedrock cliff (c). After movement along the fault ceases, the bedrock scarp degrades, reducing the local slopes. The photos are taken from (a) the Hebgen Lake fault scarp, MT (Cabin Creek locality) (b) a normal fault in the Carrizo Plain, CA, (c) Della tank graben in Northern Arizona, and (d) Babbitt Lake scarp in Northern Arizona.

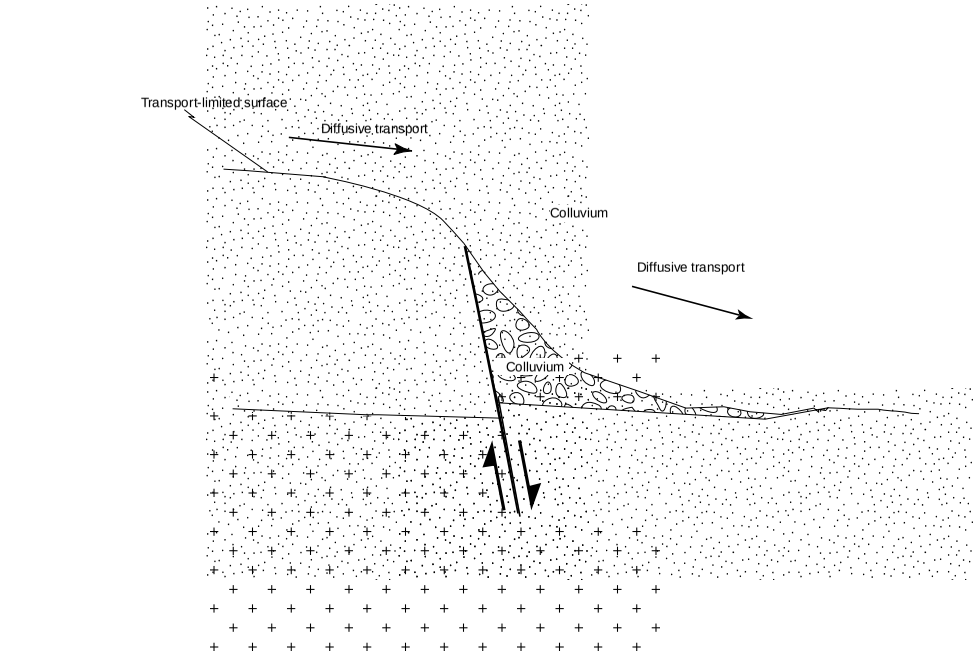

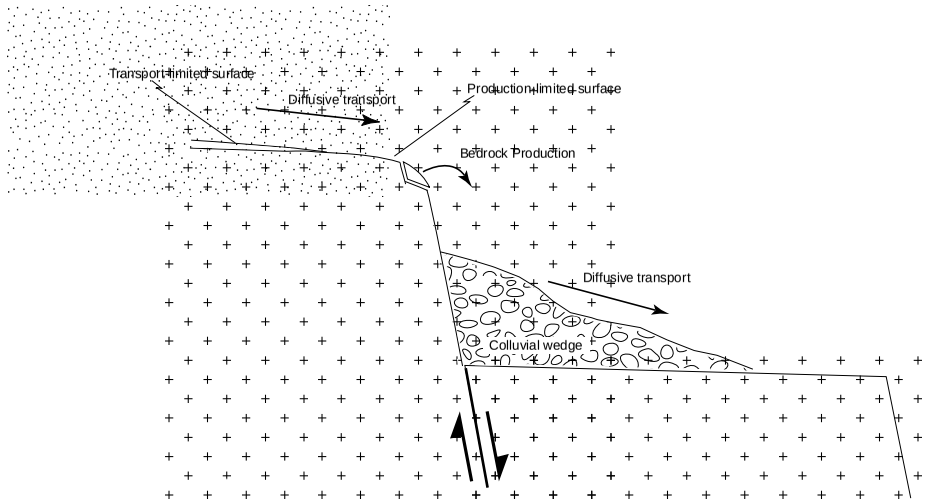

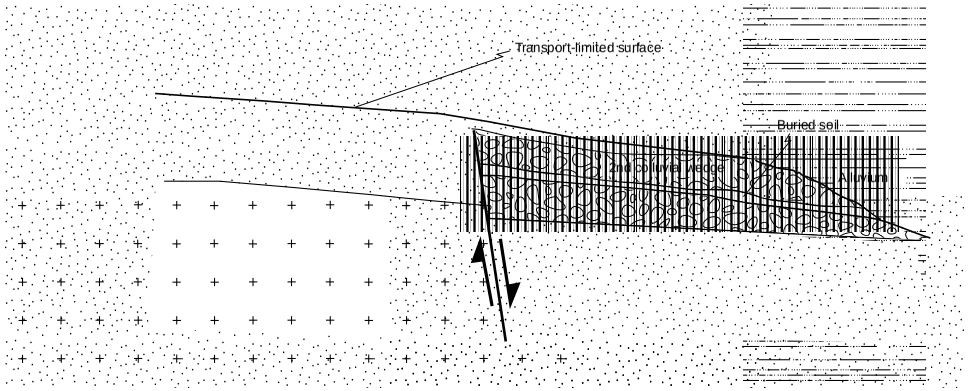

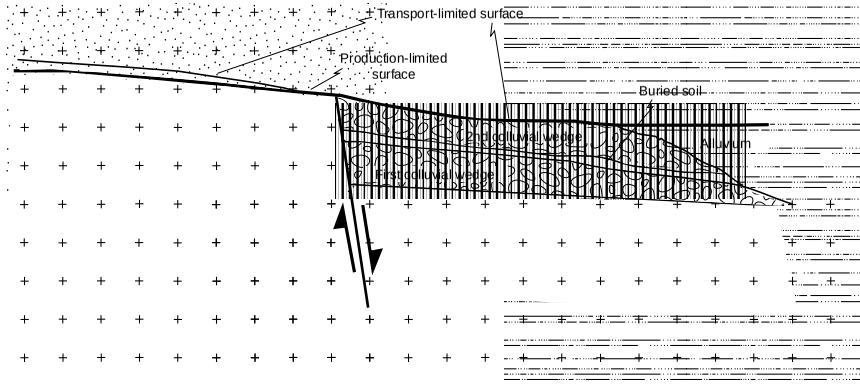

Figure 16: Schematic conceptual figure showing the development of transport- vs. production-limited scarps. (a) shows the development of transport-limited scarps. In this scenario, the bedrock is overlain by a thick section of regolith that is easily transported. As relief is created by faulting events, material is transported downslope across the slope, forming a colluvial deposit at the bottom of the scarp. With either more rupture events or continuous slip along the fault, a smooth profile is formed. After cessesion of fault movement, the fault scarp degrades to a low-relief landform. The case of a production-limited scarp is portrayed in (b). In this case, non-transportable bedrock is exhumed; therefore, transport of material cannot take place until it is produced from the bedrock. It then travels downslope and forms a colluvial apron at the bottom of the scarp. However, there is commonly a bedrock cliff above the colluvial pile. Finally, after cessesion of the movement, the bedrock scarp degrades into a low-relief landform, as bedrock is made available for transport by the conversion of bedrock to transportable regolith.

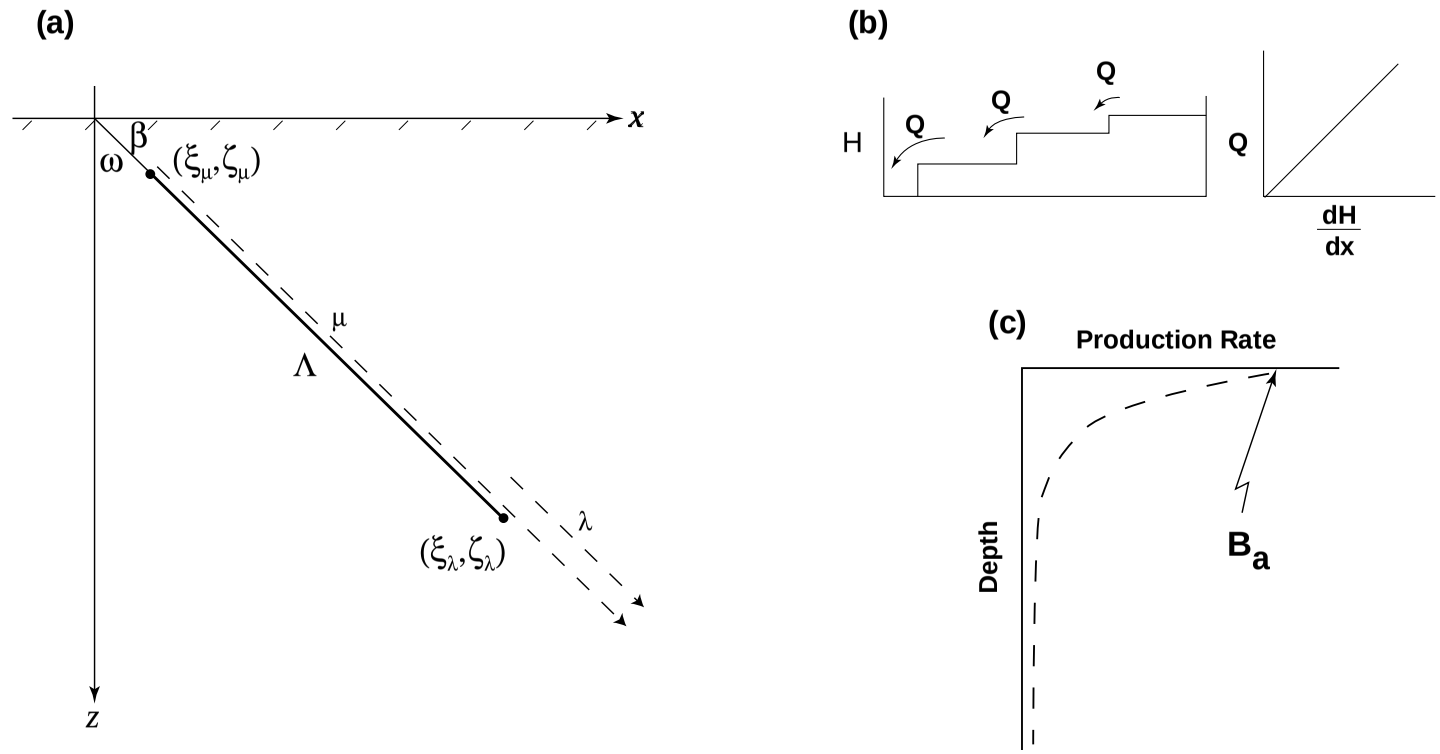

Figure 17: Figure showing fault geometry and how it relates to defined parameters in the equations of Du *et al.*, [1994]. The surface displacements are computed by summing the effect of movement on two infinitely long dislocations, one (μ) starting at (ξ_μ, ζ_μ) and extending to infinity, and the other (Λ) starting at $(\xi_\Lambda, \zeta_\Lambda)$.

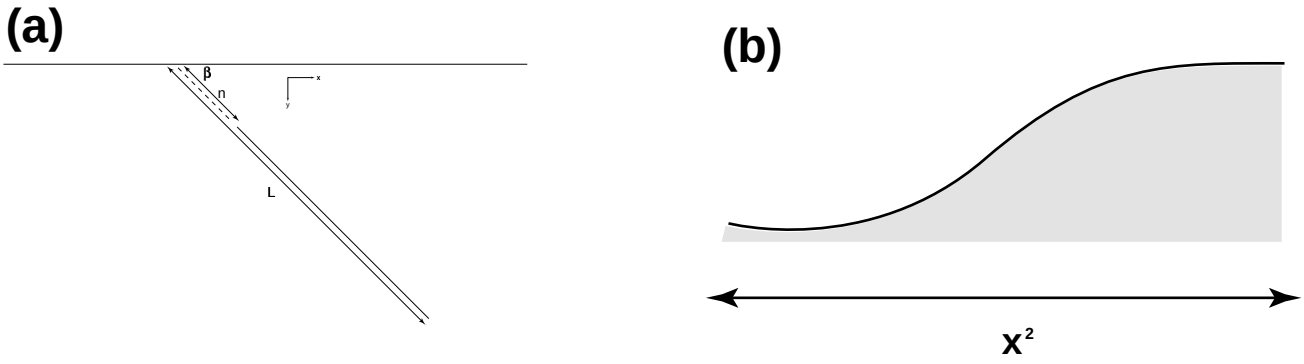

Figure 18: Definition of parameters for tectonic displacements. The displacement gradient scales with the fault length, the magnitude of the displacement scales with fault offset, and blind faults are characterized by the ratio of the no slip patch length to the total fault length (n). The no-slip patch extends from the surface at (0,0) to the top of the fault.

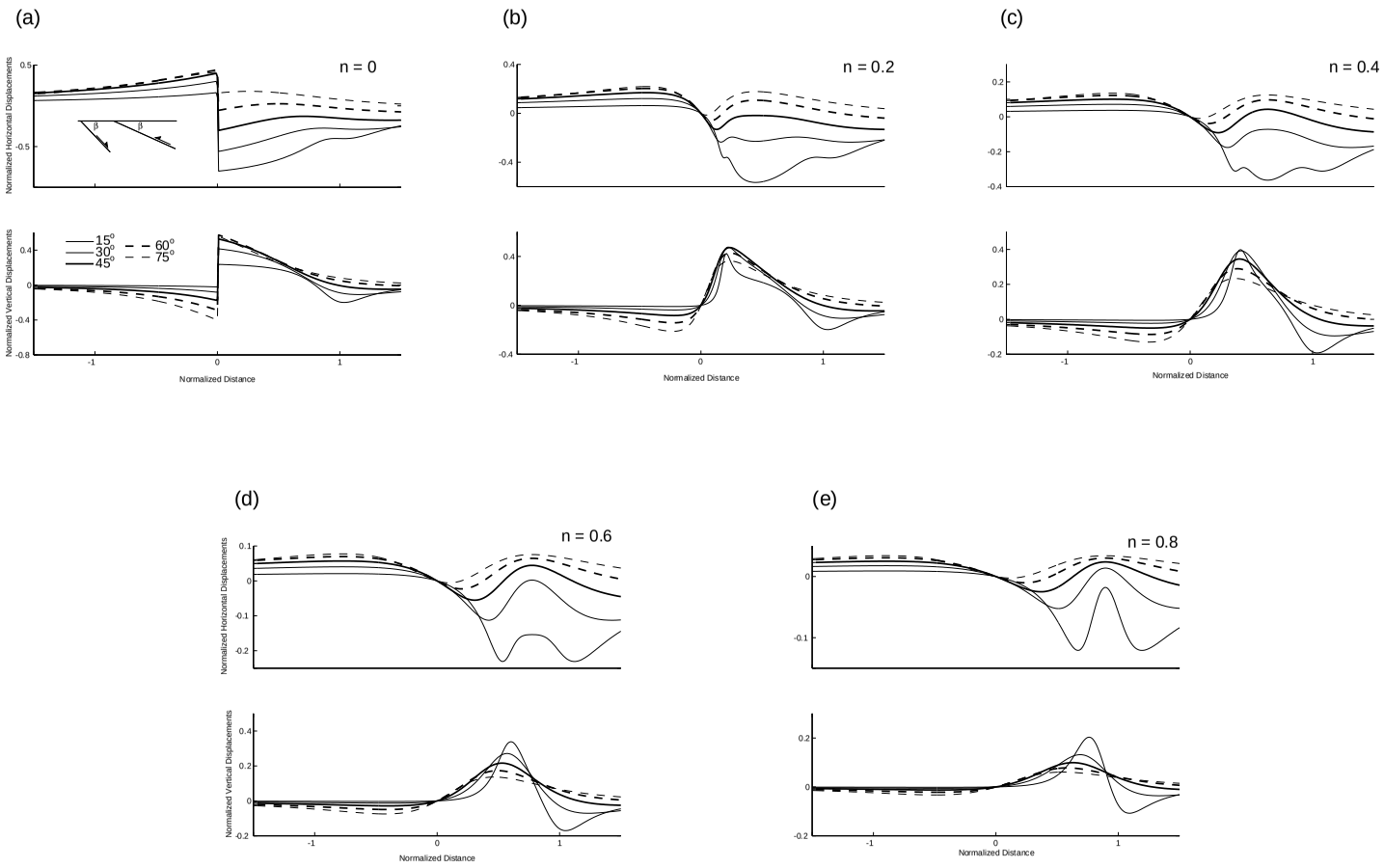

Figure 19: Surface displacements due to a unit movement along the model fault. In each of the diagrams, the upper portion of the panel shows the horizontal surface displacements, while the lower panel shows the vertical surface displacements. In (a), the fault daylights at the surface, while in (b) - (e), there exists a no-slip patch that starts at the surface and extends down to the fraction of the fault defined by n.

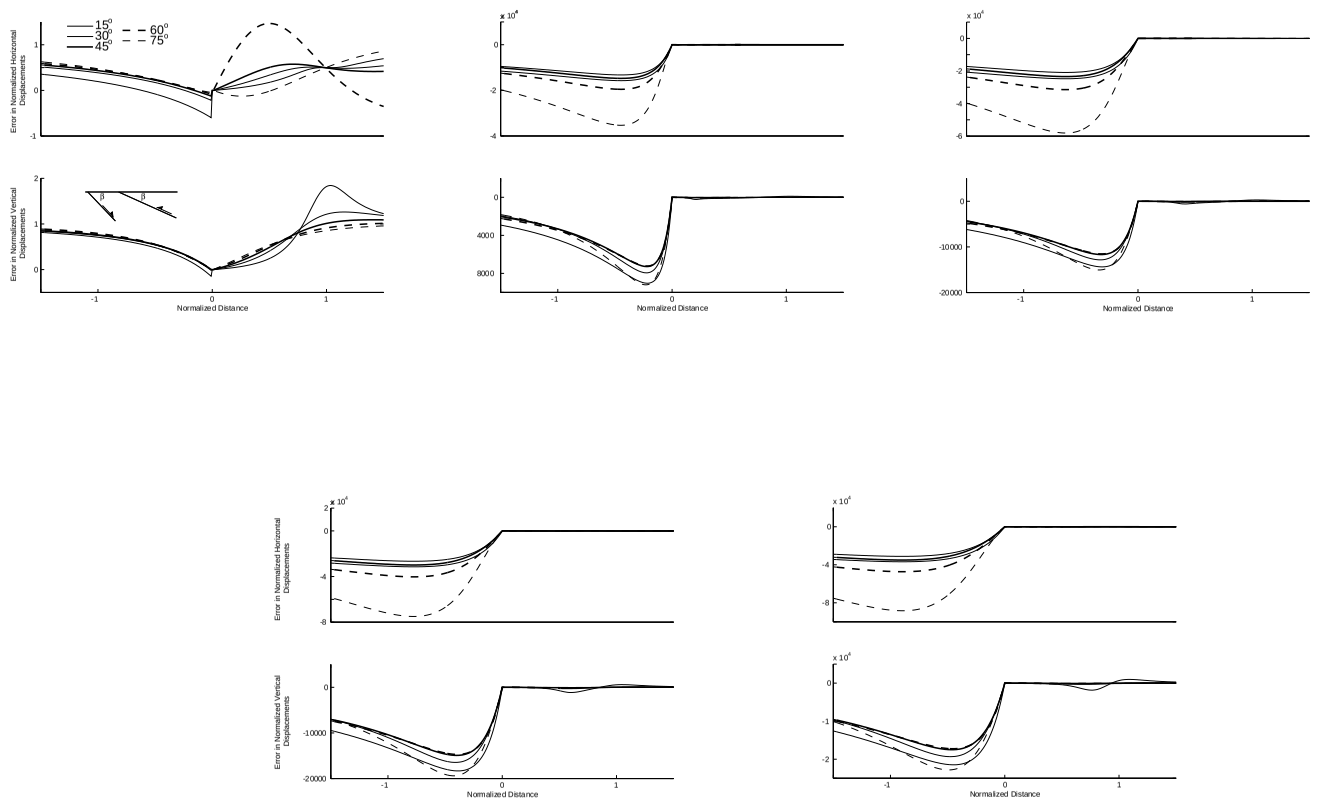

Figure 20: Differences in surface displacements computed using geometric, block faulting calculations, and mechanically-based dislocation calculations. The vertical axis in each panel show the deviation in the displacement, which we calculate as the ratio of the displacement calculated from dislocation theory to that calculated from rigid block faulting minus one. In these diagrams, a value of zero indicates perfect correspondence between the block faulting model and the dislocation model. Notice that the block fault model poorly characterizes the expected displacement distribution when the point is not adjacent to the fault (a–e) and when the fault does not reach the surface (b–e).

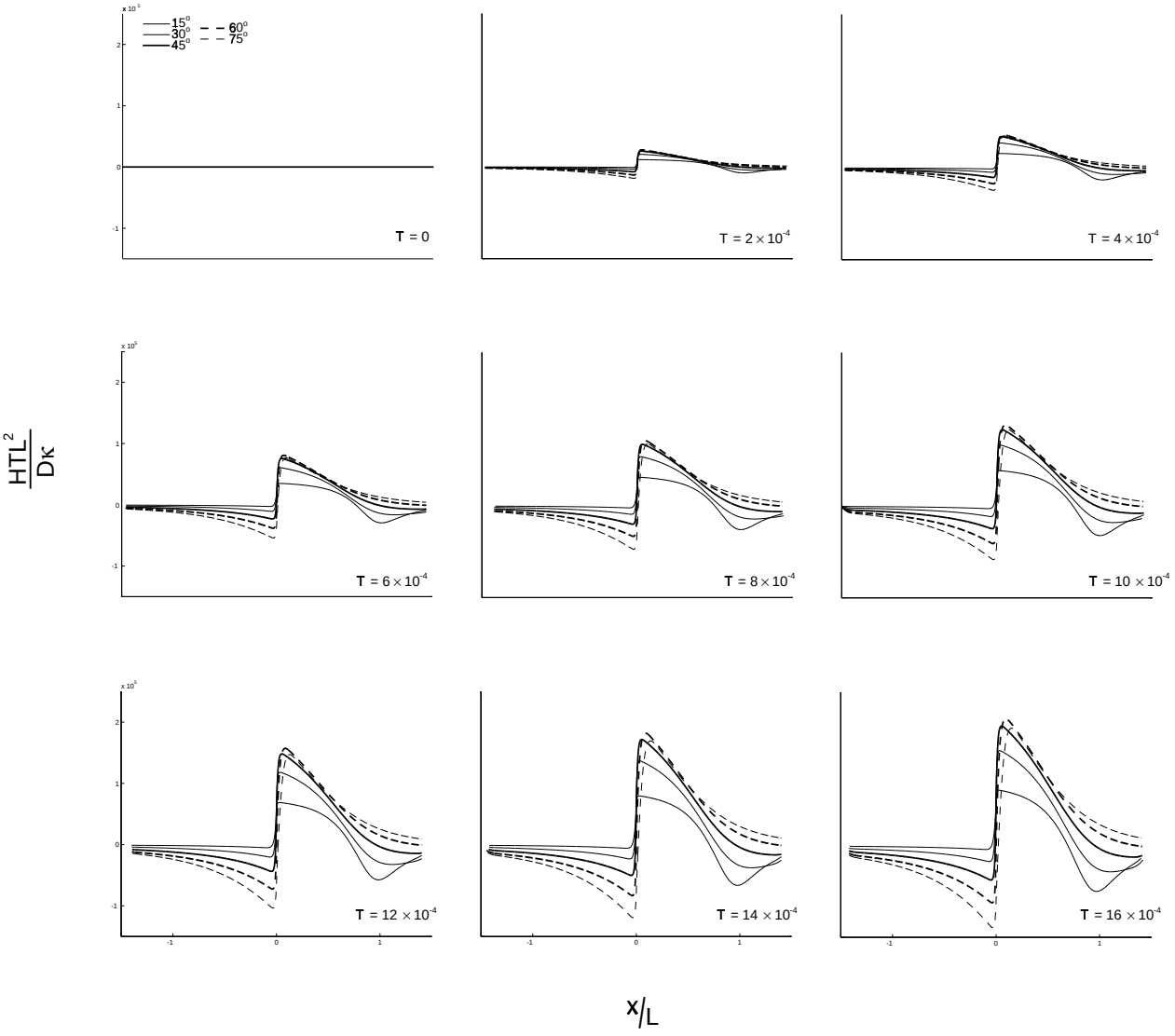

Figure 21: Morphologic development of a thrust fault over time and space. The horizontal axis plots the spatial location along the surface normalized to the fault length (x/L), and extends from -150% of the fault length to 150% of the fault length. The vertical axis plots the topography at the surface, rewritten as a function of the total fault displacement (D, the dimensionless time/space parameter, T, the fault length L, and the transport rate, κ. Each of the panels shows the development of the fault as the dimensionless morphologic parameter, T, increases. This normalization permits us to capture all transport-limited fault scarp morphologies in these diagrams. For further information regarding the normalization and the meaning of the parameters, see the text. In all of these diagrams, the fault daylights at the surface.

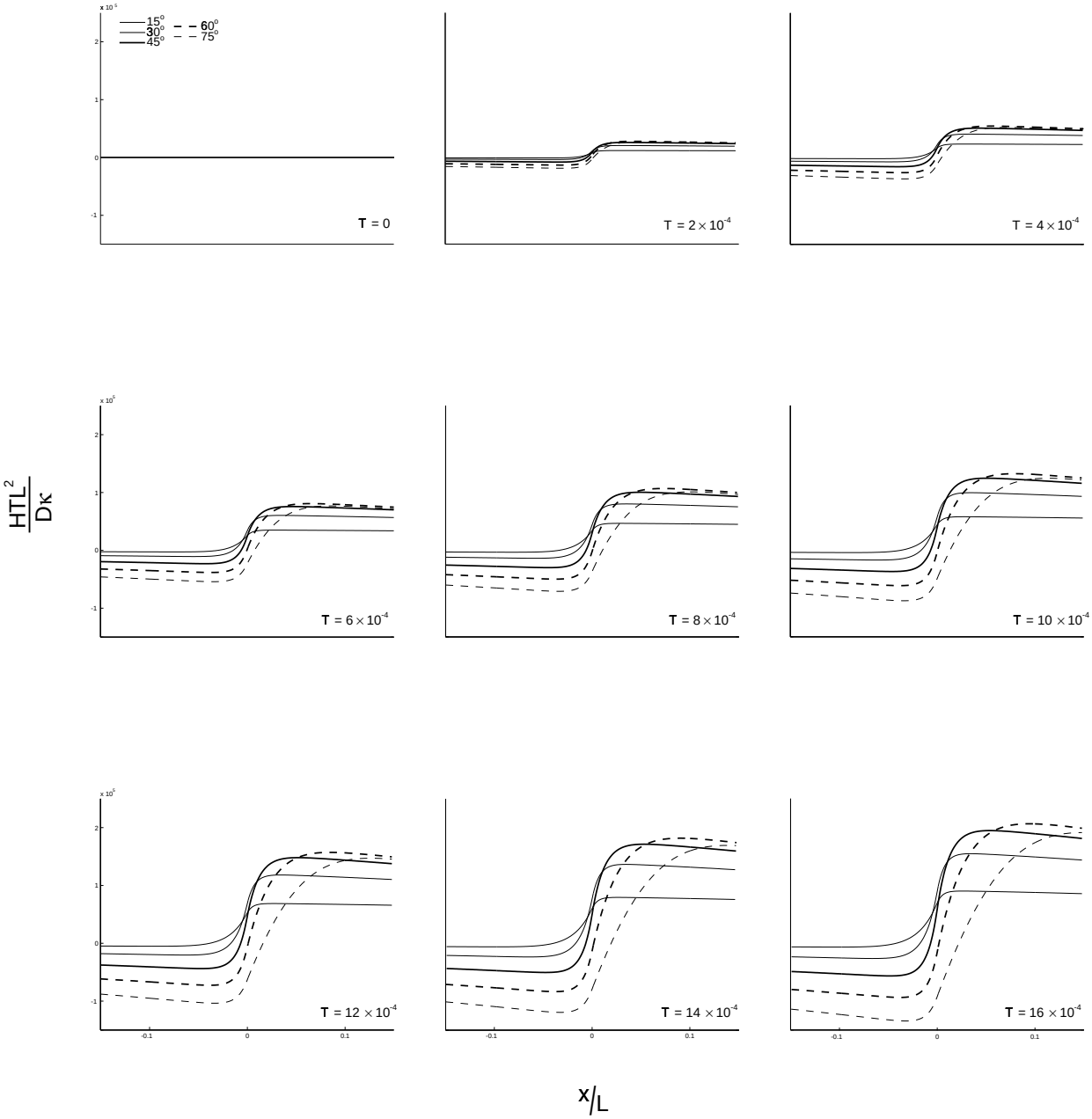

Figure 22: Morphologic development of a thrust fault over time and space. These diagrams are the same as in figure 21; however, the horizontal axis of each diagram (x/L), shows the domain between -15% and 15% of the fault length. These diagrams show the scarp development near where the fault daylights. Typically, paleoseismic studies may sample the surface topography from up to 30% of the fault length to 3% of the fault length. For a description of the variables in the diagram, see Figure 21 and the text.

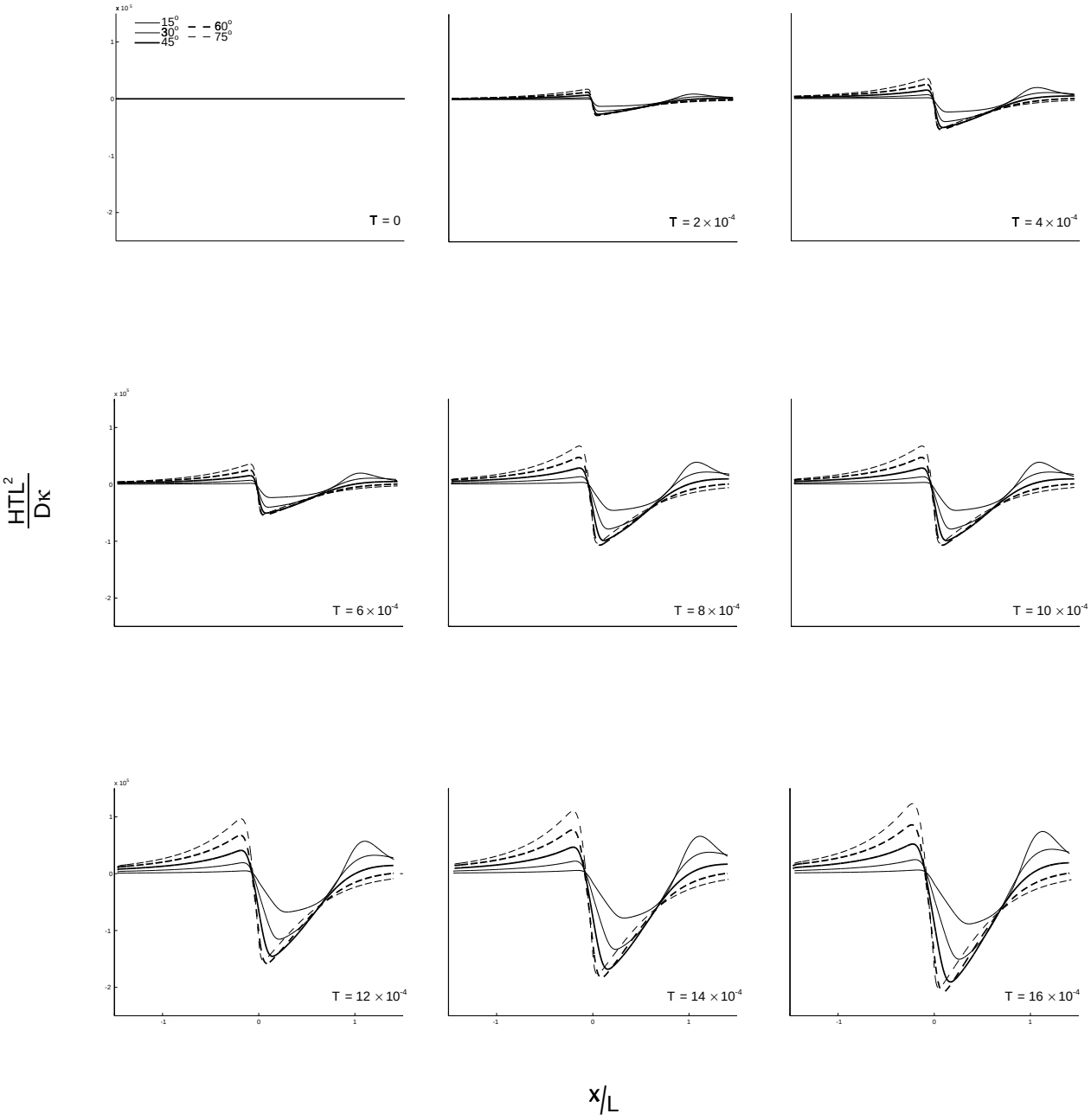

Figure 23: Development of a normal fault over space and time. Parameters are identical as those in Figure 21. The horizontal axis on this figure shows the domain between -150% and 150% of the fault length.

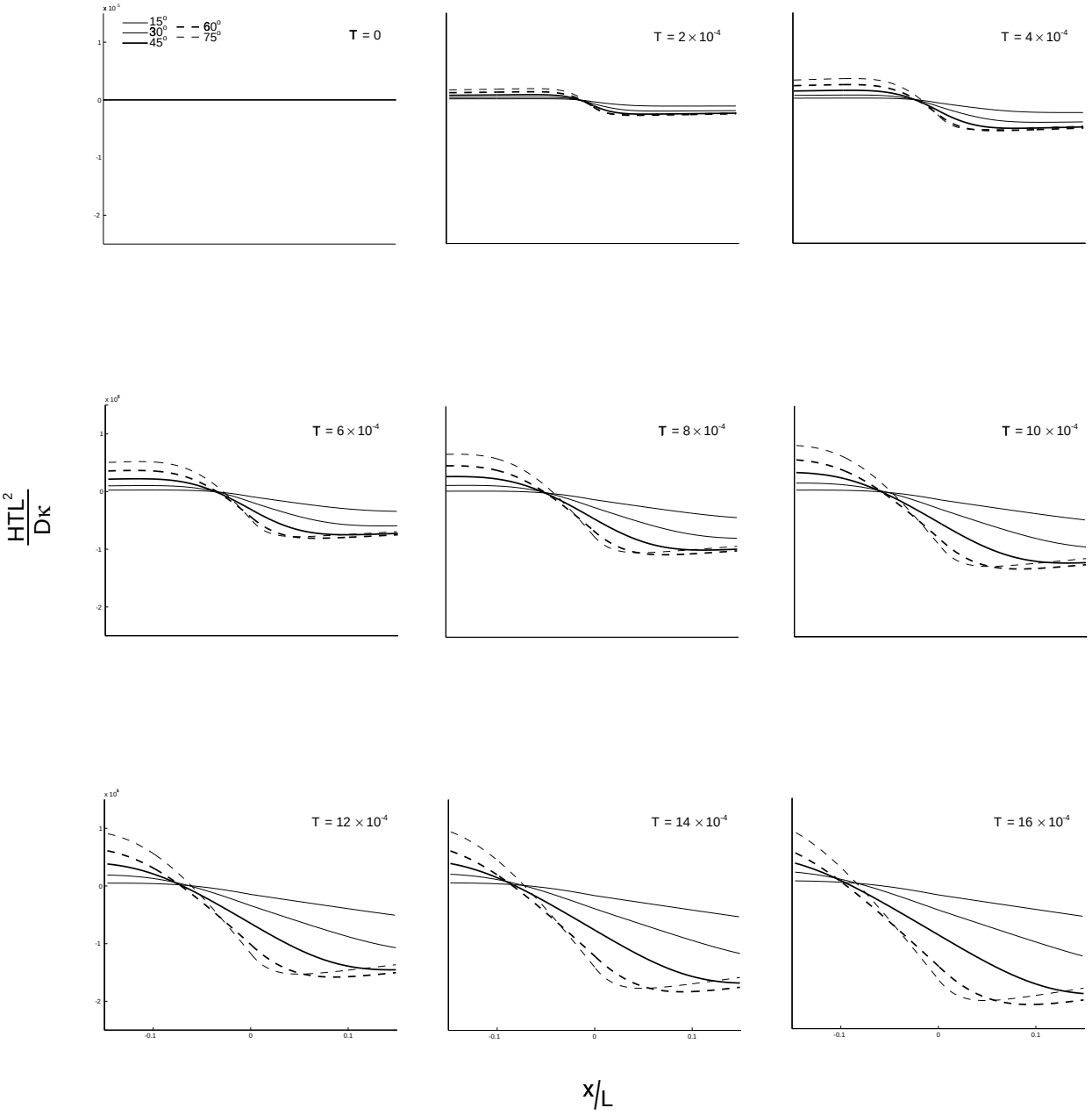

Figure 24: Development of a normal fault over space and time. Parameters are identical as those in Figure 22. The horizontal axis on this figure shows the domain between -15% and 15% of the fault length.

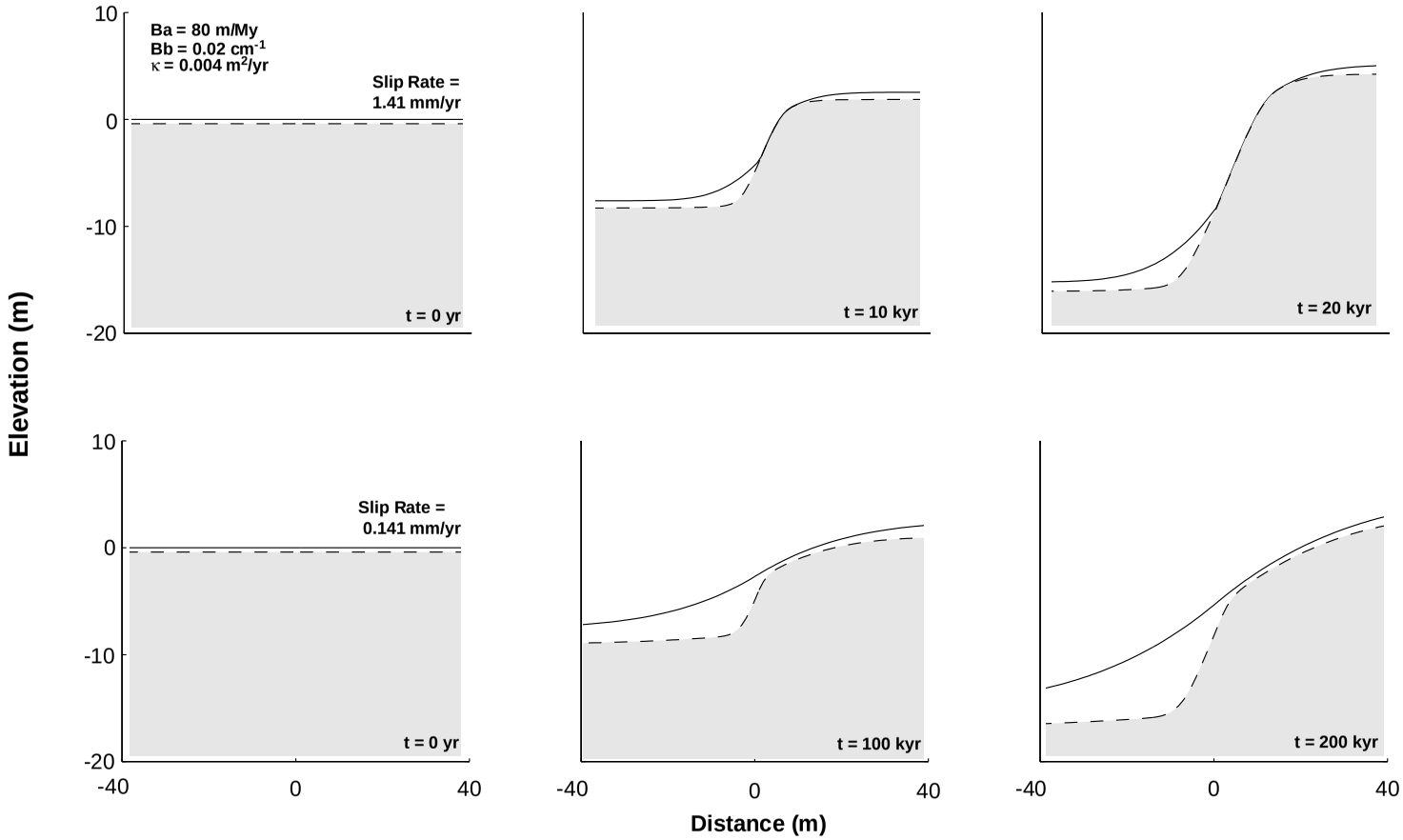

Figure 25: The effect of fault slip rate on the morphologic development of a 45 degree dipping normal fault scarp over time. In this figure, the bedrock production rate, B_a, the thickness sensitivity B_b, and the transport constant, κ are fixed. The fault slip rate in (a) is constructed to produce one millimeter of uplift per year, while the fault slip rate in (b) is constructed to produce one tenth of a millimeter of uplift per year. The gray section of the diagrams is the bedrock, while the solid line denotes the topographic surface. The development of fault scarps with low slip rates is shown in (a), while (b) shows the development of a fault along which the slip rate is high. The total displacement in the panels in (a) and (b) is the same; therefore, time in (b) is an order of magnitude greater in the upper panel than the lower panel. We see that slower slip rates allow more time for the production of regolith from bedrock, preserving transport-limited conditions longer in the vicinity of the scarp. Therefore, when differential uplift rates exceed bedrock production rates, all other things equal, we expect the rapidly slipping fault to be expressed as a bedrock cliff with a small colluvial pile, whereas the slowly slipping fault is expressed as a slowly slipping fault with a large colluvial pile at the base of the scarp.

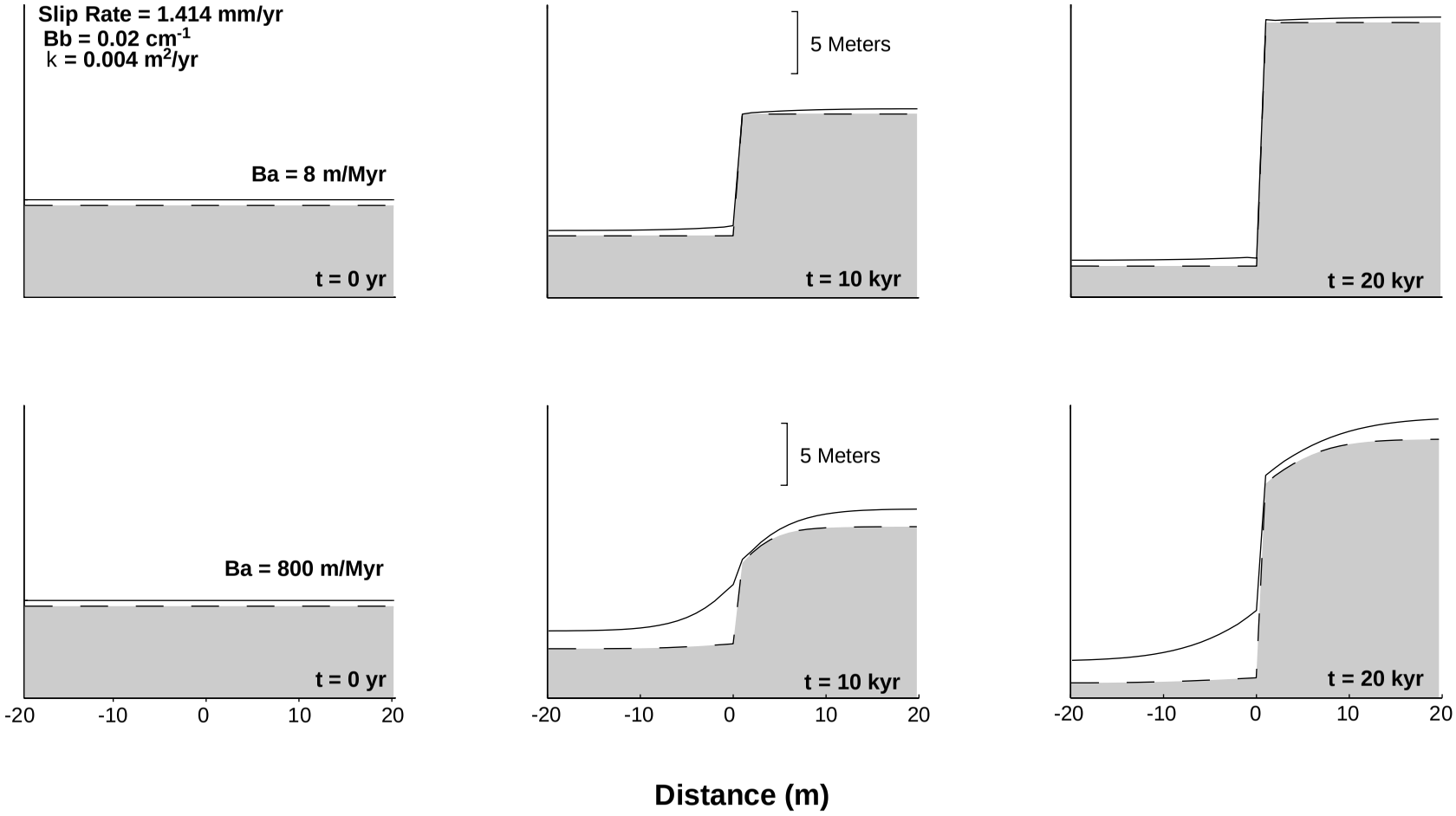

Figure 26: The effect of variations in surface bedrock production rates on fault scarp morphology. As in Figure 25, the fault dips 45 degrees. The fault slip rate is designed to produce one millimeter of uplift per year. In (a), the bedrock production rate is small (8 m/Myr), and in these cases, bedrock cliffs form at the scarp and small colluvial piles are formed at the base of the scarp. As bedrock surface production rates increase relative to the fault slip rate, transport-limited conditions can be maintained for longer periods of time, allowing transport-limited conditions to persist for longer periods of time along the scarp. This results in a more "diffusive" form of the scarp and the higher production rates produce a large colluvial pile at the base of the scarp.

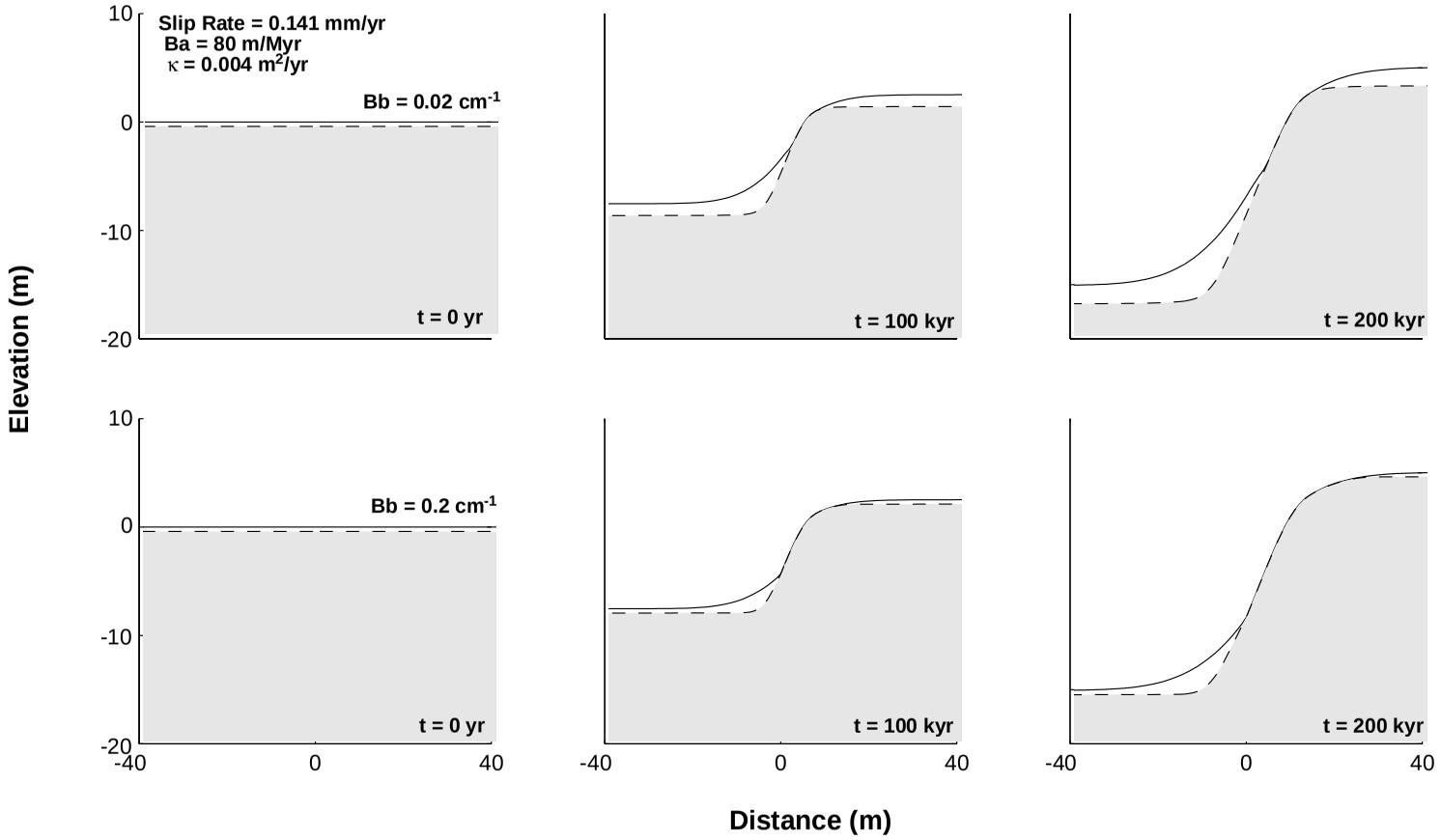

Figure 27: The effect of the thickness sensitivity parameter, B_b on the morphologic development of production-limited scarps. As in Figure 25a, the fault dips at 45 degrees and is designed to produce one tenth of a millimeter of uplift per year. In this case, greater depth sensitivity (lower values of B_b) maintain transport-limited conditions above the scarp(a) , while less depth sensitivity creates a scarp in which the upper section of the scarp is dominated by production-limited conditions (b).

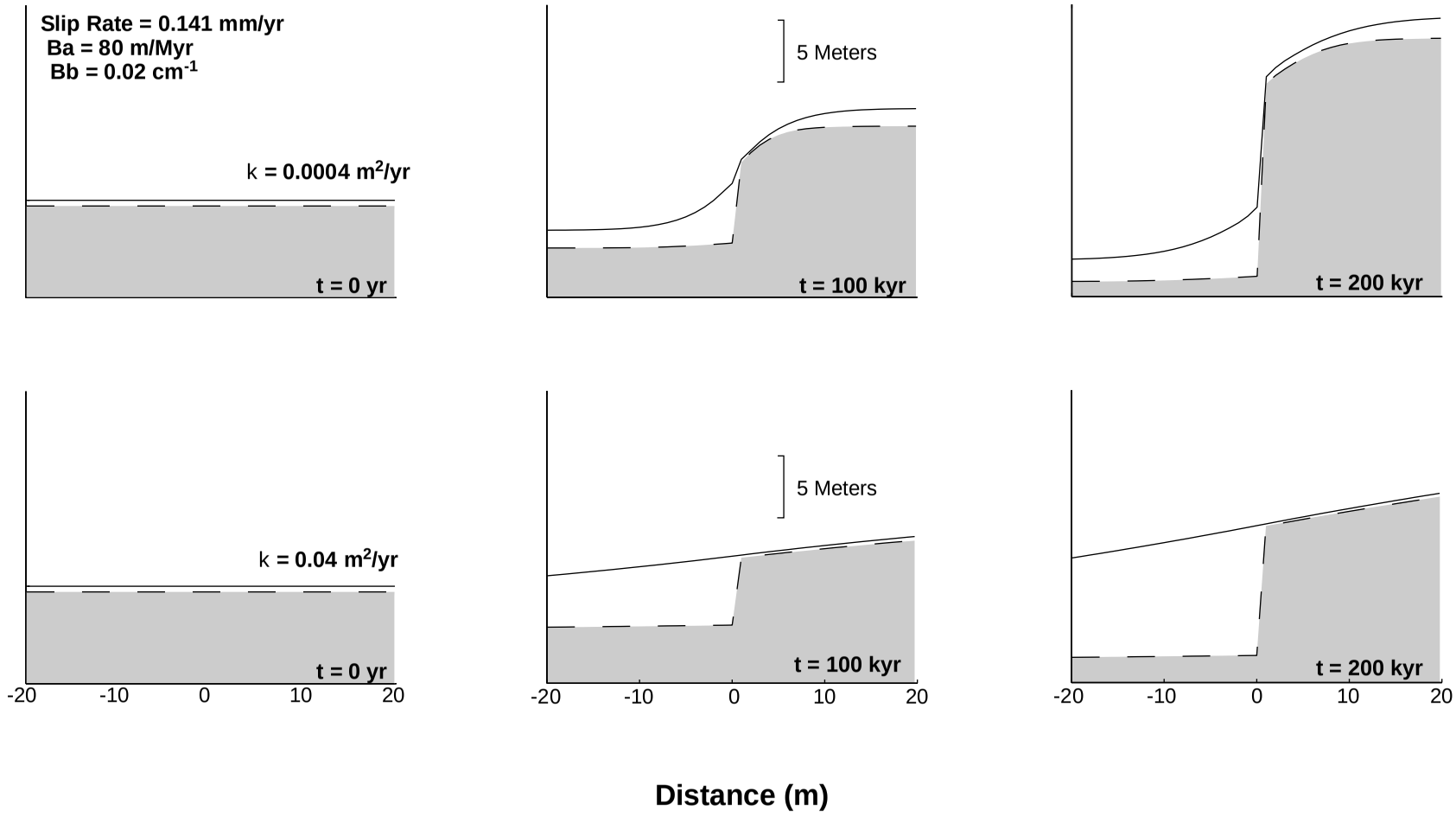

Figure 28: The effect of transport rate on the development of production-limited scarps. Low transport rates, which may represent arid conditions [Fernandes *et. al*, 1996], are depicted in (a), while high transport rates are depicted in (b). In (a), bedrock is exposed early in the history of movement along the scarp, while transport-limited conditions persist with high transport rates (b). When geomorphic rates are low, material only adjacent to the scarp can be transported to reduce the relief in a given amount of time. However, high transport rates allow more material to be transported to reduce the relief in the same amount of time. Therefore, lower transport rates initially favor higher relief localized at the fault trace. Bedrock is thus exposed earlier in the slip history for low transport rates, relative to high transport rates. It is important to note that eventually, bedrock will be exposed in the case of high transport rates, due to the fact that bedrock production rates are less than the rate at which relief is created in the landscape. Once bedrock is exposed, the high transport rate scarp will quickly transition from a transport-limited scarp to a production-limited bedrock cliff, and high transport rates will allow the colluvial pile to be rapidly removed from the bottom of the scarp. After the exposure of bedrock in the high transport rate case, the scarp will proceed to be more "production-limited" than the low transport rate scarp. Therefore, the transport rate not only effects the

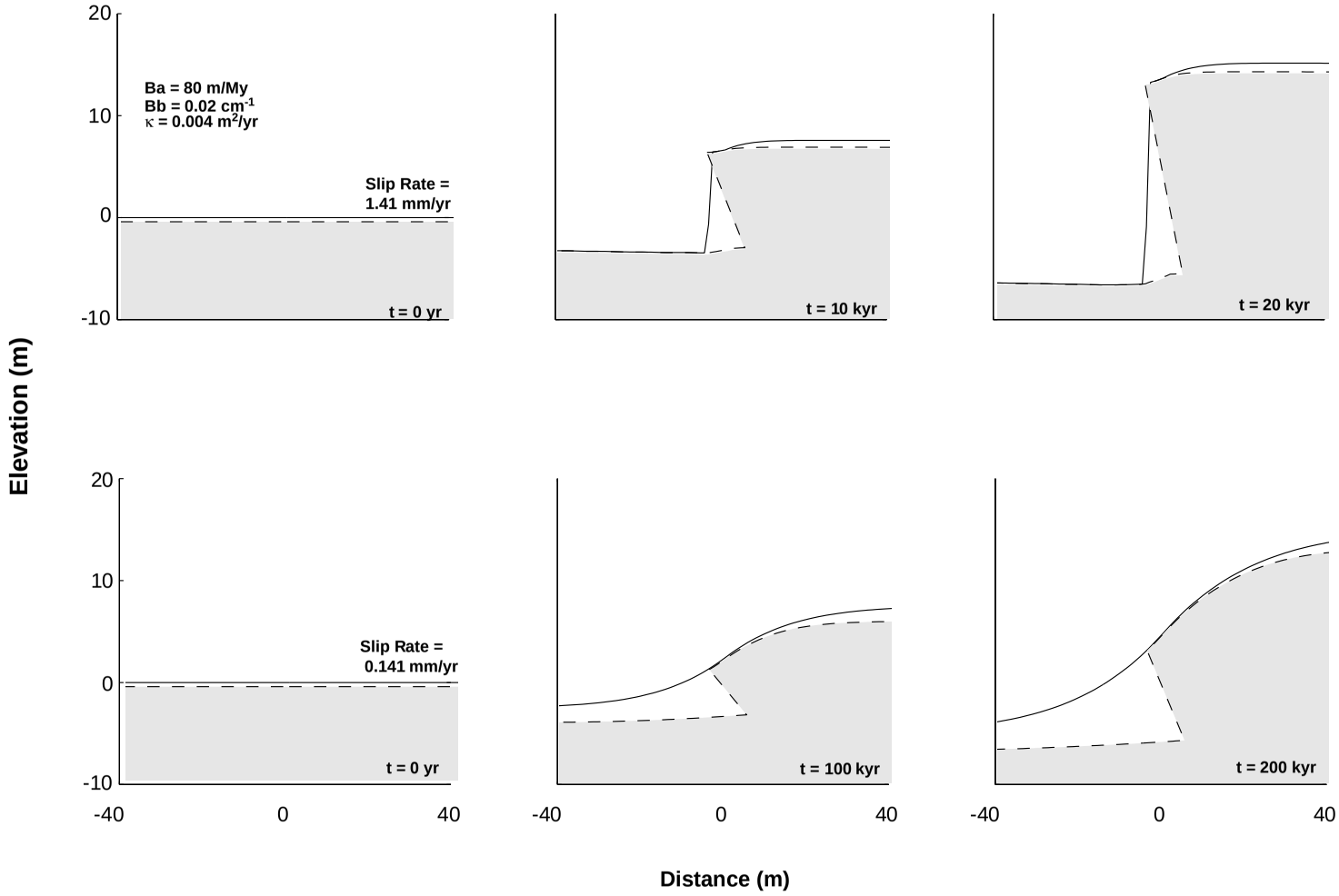

Figure 29: The effect of variable thrust fault slip rate on the surface displacement field and subsequent geomorphic response. Note also the development of the overhang, given the refined interpolation method described in the text.

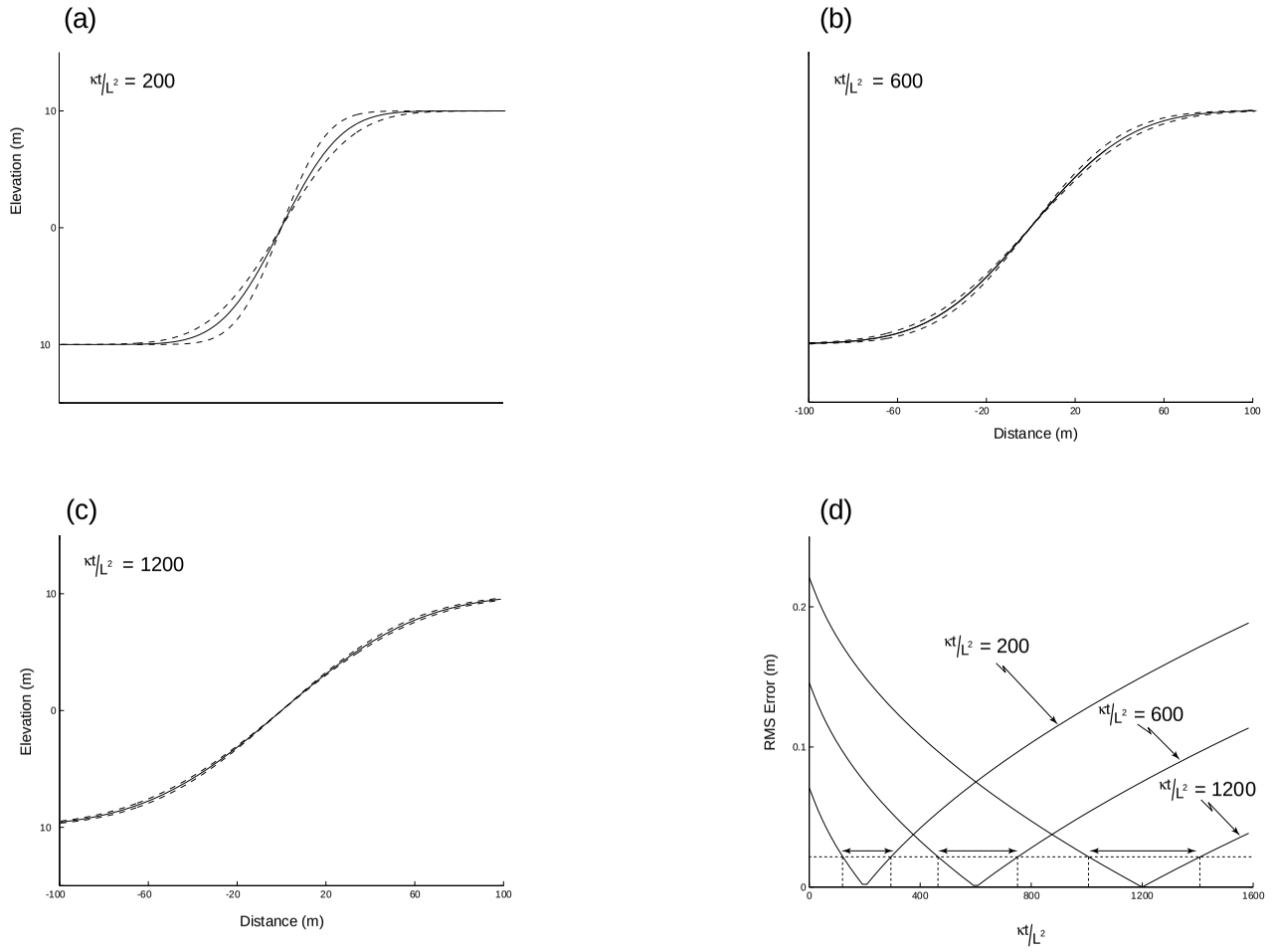

Figure 30: The ability to resolve timing of movement along a single-event scarp declines with time. In (a)–(c), we simulate a vertical, single-event scarp that degrades over time. The length scale, L, is arbitrarily set to one. The solid lines show the theoretical scarp profile at 200, 600, and 1200 in (a), (b), and (c), respectively. The dashed lines show the scarp profile calculated at ± 100 from the value of the dimensionless morphologic parameter of the scarp. As can be seen in (a)–(c), as the scarp becomes older, it becomes more difficult to discern the difference between the scarp at a given stage of development, and that ± 100 away from the scarp. Figure (d) summarizes these results by plotting the RMS error between the target profile and those of different ages vs. the dimensionless morphologic parameter for each of the different diagrams (a)–(c). The older profiles touch the horizontal axis in panel (d) farther to the right than the younger diagrams. For a given RMS error, as the profile gets older, the error in the age calculation becomes greater. Therefore, panel (d) shows the decrease in the "memory" of the scarp as the scarp degrades with time.

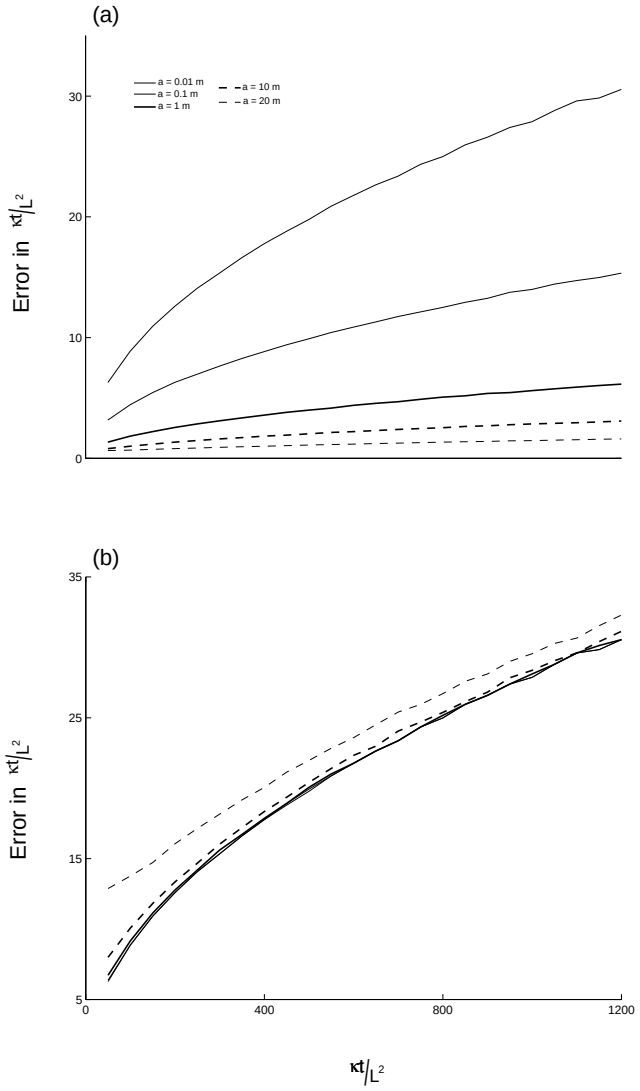

Figure 31: Error in the dimensionless morphologic parameter as a function of the stage of morphologic development defined by the dimensionless morphologic parameter for single event scarps. Increasing errors correspond to a reduction in our ability to accurately determine the timing of movement along the fault. Panel (a) shows the error in $\frac{\kappa t}{L^2}$ for a 0.01 deviation in the RMS error. Panel (b) shows the error in $\frac{\kappa t}{L^2}$ for an RMS error that is 10% of the scarp height. The morphologic development of smaller scarps are more sensitive to a constant RMS value than larger scarps, as shown in panel (a). In (b), we attempt to remove the effect of the scarp height in computing RMS by expressing the threshold RMS as a function of the scarp height. As seen in (b), this method is valid for small scarps; however, as scarp height increases, we see deviations from the normalized RMS.

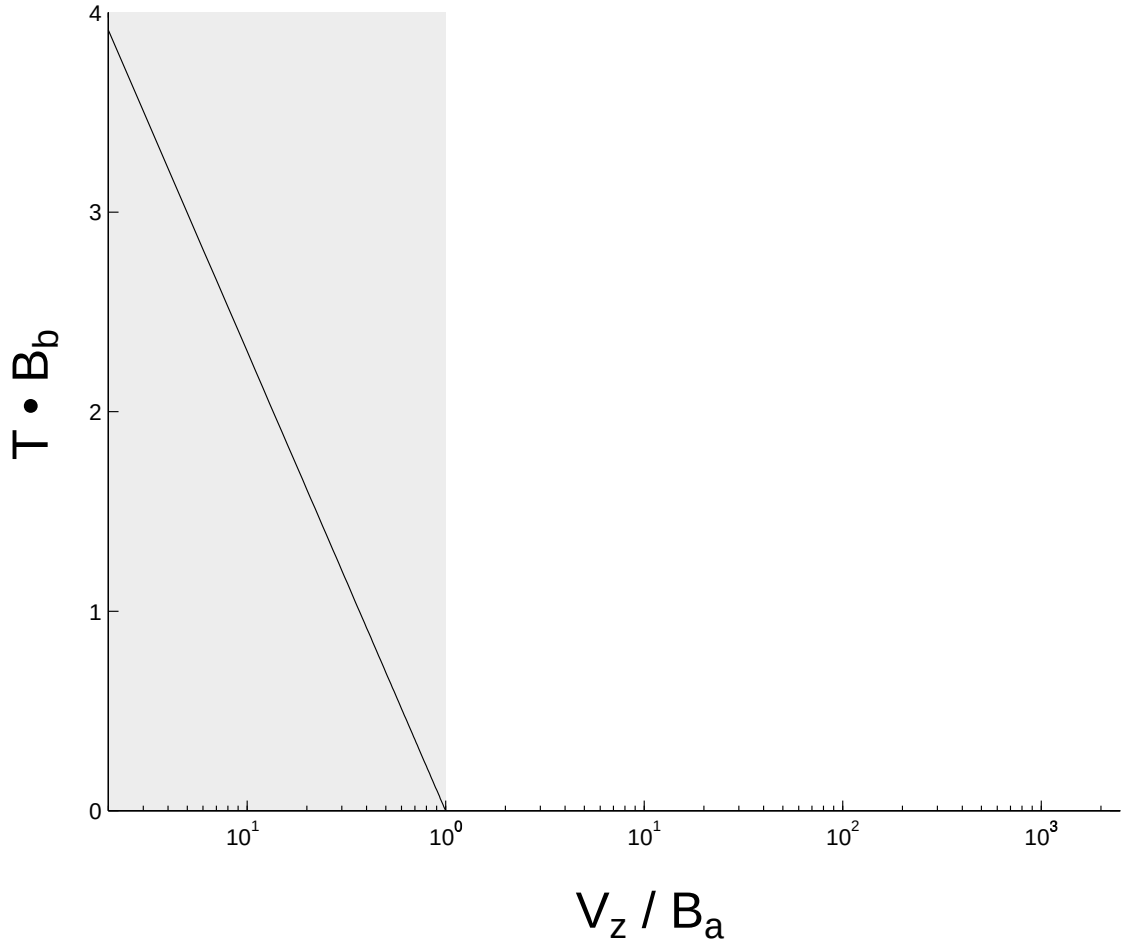

Figure 32: Figure showing the steady-state regolith thickness in a denuding diffusive landscape. The horizontal axis shows the ratio of the uplift rate (S) to the surface bedrock production rate (B_a). The extent of the horizontal axis shows the range of possible values in tectonic environments by computing a high value using an uplift rate of 0.2 m/yr and a bedrock production rate of 8×10^5 m/yr. We hypothesize that regolith can only be produced when the bedrock production rate is equal to the rate at which the diffusive landscape is being lowered. Therefore, only values of $S/B_a \leq 1$ constitute valid steady-state diffusive landscapes. The vertical axis shows the steady-state regolith thickness normalized by the depth scaling factor, B_b.

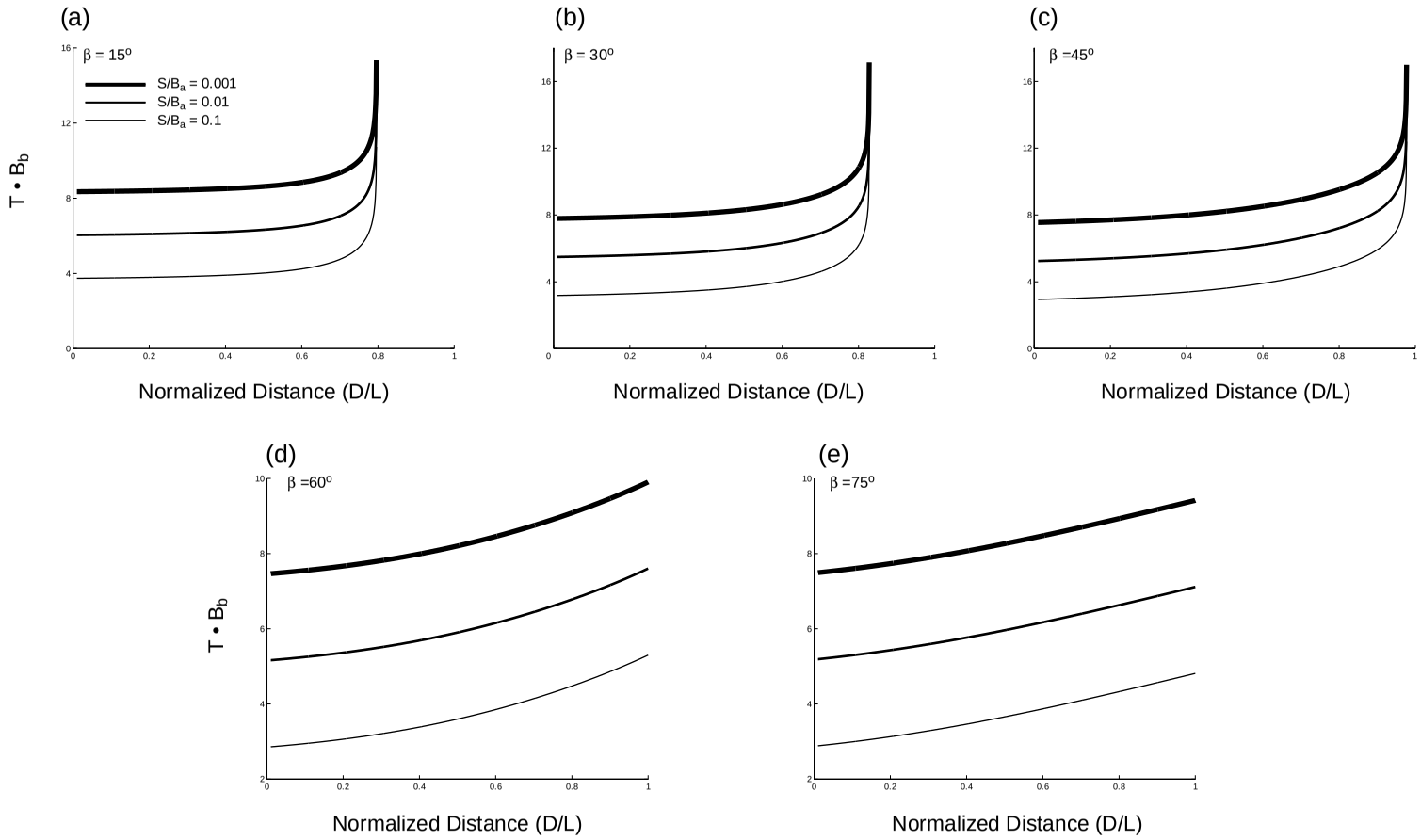

Figure 33: Figure showing the steady-state regolith thickness in the hanging wall of a fault moving at a constant rate. The fault slip rate is defined by the ratio of the fault slip rate (S) to the bedrock production rate (B_a). We consider ratios of S/B_a less than one as those conditions required for a steady-state transport limited scarp. With lower ratios of S/B_a, greater regolith thicknesses are possible.

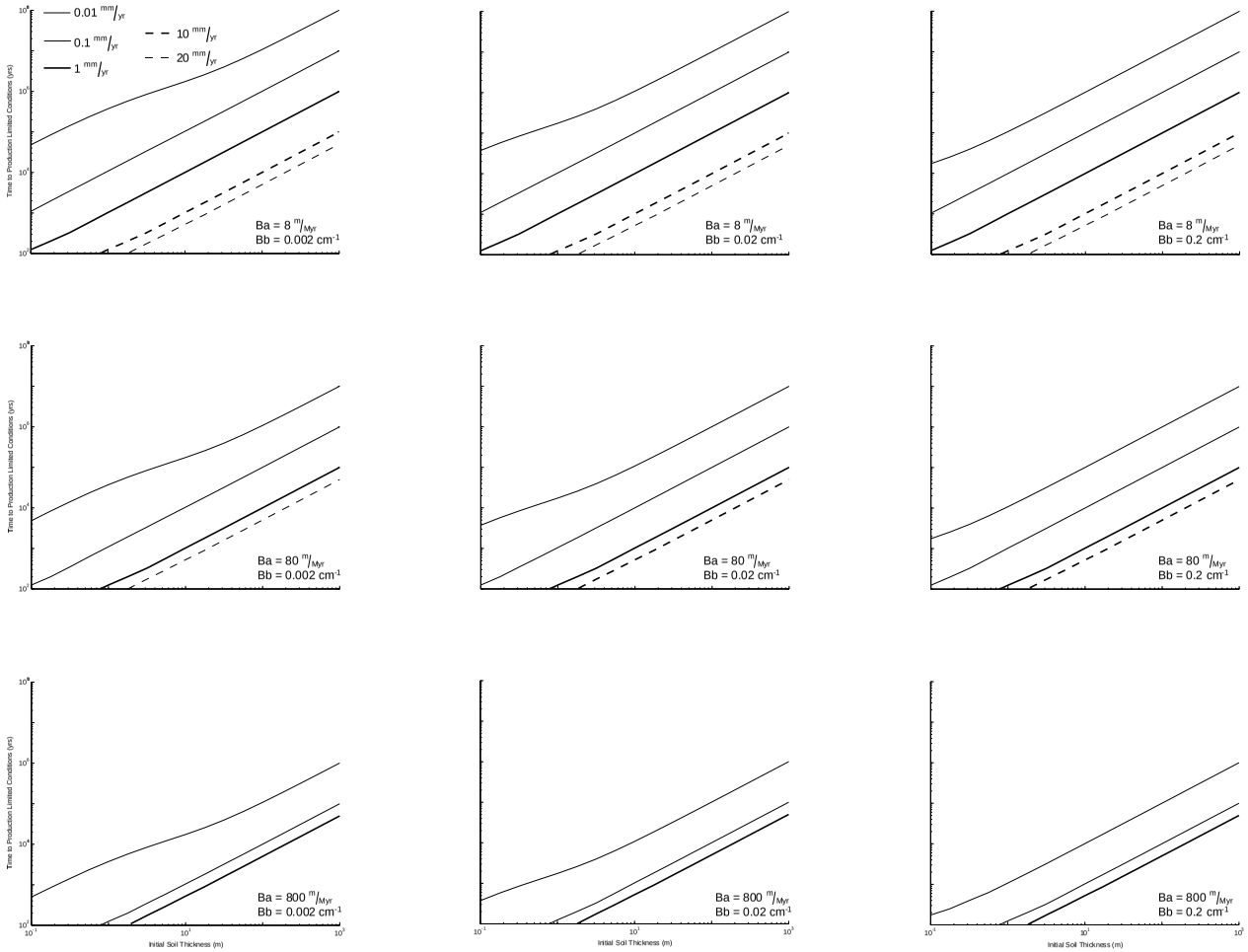

Figure 34: Time at which bedrock is exposed in a landscape being uniformly exhumed at a constant rate. The different panels show different production parameters, B_a and B_b. The horizontal axis is the initial regolith thickness draping the landscape, while the vertical axis shows the time at which the bedrock is exposed for a variety of different exhumation rates. We see in the figures that for high exhumation rates, the B_b parameter is unimportant, while at rates of exhumation comparable to B_a, B_b increases the time required to reach bedrock. This is manifest in the deflection of the low exhumation rates upward in the panels. If the morphology of the landscape is in equilibrium with the uplift rate, then the exhumation rate equals the rock uplift rate. In this case, these diagrams depict the maximum amount of time a landscape can remain in a state of equilibrium where the surface morphology remains relatively constant, but the location of the bedrock/regolith interface is changing.

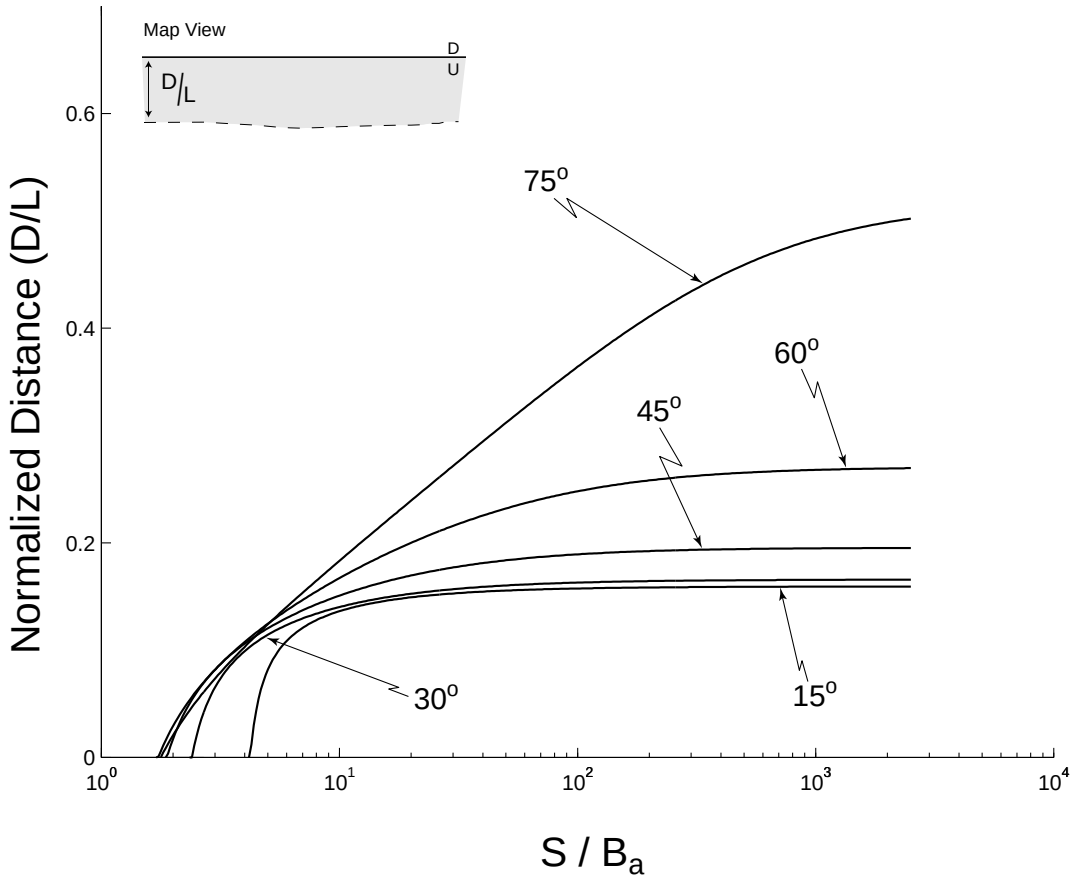

Figure 35: Graph showing the transition between transport-limited and production-limited conditions for a scarp in steady-state equilibrium. Areas above the threshold line for each fault geometry preserve regolith under equilibrium conditions, whereas areas below the threshold line are dominated by production limited conditions. As the ratio of the slip rate to the bedrock production rate (S/B_a) increases, the landforms near the fault become progressively more production-limited. Also, as the fault dip increases, uplift becomes more significant at the fault's intersection with the surface, decreasing the critical value of S/B_a required for production-limited conditions at steady-state.